Artificial photosynthesis and generation of hydrogen by splitting water

A thesis submitted in partial fulfilment for
the degree of
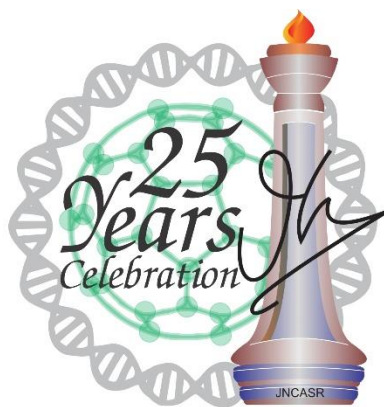
Master of Science

as part of the

Integrated Ph. D. programme
(Materials Science)

by

Uttam Gupta

Chemistry and Physics of Materials Unit
Jawaharlal Nehru Centre for Advanced Scientific Research
(*A Deemed University*)
Bangalore, India.

April 2014

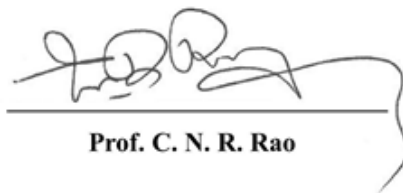*Dedicated to my family, teachers and friends*

II

DECLARATION

*I hereby declare that the matter embodied in this M.S. thesis entitled "**Artificial photosynthesis and generation of hydrogen by splitting water**" is the result of investigations carried out by me under supervision of Prof. C. N. R. Rao, FRS at the Chemistry and Physics of Materials Unit, Jawaharlal Nehru Centre for Advanced Scientific Research, Bangalore, India and that it has not been submitted elsewhere for the award of any degree or diploma.*

In keeping with the general practice in reporting scientific observations, due acknowledgement has been made whenever the work described is based on the findings of other investigators.

_____

Uttam Gupta

CERTIFICATE

*I hereby certify that the matter embodied in this M.S. thesis entitled "**Artificial photosynthesis and generation of hydrogen by splitting water**" has been carried out by Mr. Uttam Gupta at the Chemistry and Physics of Materials Unit, Jawaharlal Nehru Centre for Advanced Scientific Research, Bangalore, India under my supervision and it has not been submitted elsewhere for the award of any degree or diploma.*

Prof. C. N. R. Rao

(Research Supervisor)

Acknowledgements

I am extremely thankful to Prof. C. N. R. Rao, FRS and I take this opportunity to express my immense gratitude to him.

"Guru gobind dou khade,kaake lagoon pay (Guru and God both are here to whom should I first bow)

Balihari guru aapne gobind diyo batay (All glory be unto the guru path to God who did bestow)"

He not only introduced me to the field of Material Science but also has helped me with his invaluable guidance and fascinating constant encouragement. He is a person of immense enthusiasm and wisdom. It is a rich and fulfilling experience to work under his guidance. He has taught me the various facts of science, the way of understanding the problem and how to maintain levelheaded approach when problems do not work.

I would like to express my sincere thanks to Dr. A. Govindaraj who has helped me a great deal in carrying out various experiments. His friendly attitude towards me has made him a very approachable person for any kind of problem.

I thank Prof. Umesh Waghmare and Dr. Ranjan Dutta for their support and suggestions in collaborative work.

I thank Urmimala Maitra, Dr. B.S Naidu, Dr. Mrinmoy De, Mr. Bolla Govinda Rao, Dr. B E Prasad, Mrs. Anjali Singh and Ms. Sharmila Shirodkar for their collaborative work and various discussions.

I would like to thank specially Mr. Nitesh Kumar for suggestions and helping me in various possible ways.

I would like to thank Mr. Ritesh Haldhar and Thripuranthaka M. Nagaleekar for help in gas adsorption measurements and conductivity measurement.

VI

Preface

Energy crisis being a serious problem of the upcoming decade efforts need to be made to develop new model of energy system other than the present fossil fuels. One of the alternatives is to obtain an active fuel like hydrogen, from cleaner and greener source of like water and solar energy.

In this thesis we employ various strategies to split water to obtain both oxygen and hydrogen. Chapter 1 gives a brief overview of the need for Hydrogen as an alternate fuel and various strategies employed in water splitting.

In chapter 2, we show the role of electronic configuration and crystal structure of lanthanides of cobaltates and manganates in photocatalytic water oxidation.

In chapter 3 we have used group 4, 5 transition metal dichalcogenides (TiS_2 and TaS_2) for water splitting. Although they are inactive independently but they act as a cocatalysts. Nanocomposites of CdS with TiS_2 and TaS_2 were used for hydrogen evolution reaction of water. Metallic TaS_2 was found to be a better co-catalyst in water splitting.

There is a brief overview on crystal and electronic structure of transition metal dichalcogenides and how we can modify them to use as desired for photocatalysis.

In chapter 4 we have used Group 6 metal dichalcogenides MoS_2 and $MoSe_2$ for water splitting. We have employed various strategies like shifting of CBM of Mo and the changing of electronic structrure of the MoX_2 (X=S, Se) to achieve greater efficiency. It was found that 1T form of MoX_2 was a better catalyst in HER.

Contents

Chapter 3.

Water splitting based on few-layer TaS$_2$ and TiS$_2$ …..………..…………………..*37*

X

Chapter 1

Brief introduction to

Artificial photosynthesis

Introduction

Energy and environmental issues have become the biggest technological challenges of today. The global energy demands have been stipulated to rise from current level of 12 TW per day to 27 TW by 2050. The current sources of energy, primarily hydrocarbons, coal and petroleum are non-renewable and will not be able to sustain the increasing demands of energy for it is getting consumed and also diminishing. It is expected that due to increasing consumption of the fossil fuels will last for another 30-40 years. Also, burning of hydrocarbons emits CO_2, the major greenhouse gas leading to environmental degradation and global warming. According to International energy agency, the goal of limiting global warming to 2°C is becoming more difficult to maintain with each passing year and if action is not taken within 2020, all allowable CO_2 emissions would be locked. Therefore, alternative energy supplies are urgently needed to limit our dependence on fossil fuels. Out of the major ways like hydroelectrical, wind power and harvesting sun energy, the solar energy is the most abundant and sustainable natural source of energy. The earth receives about 120,000 TW each day, way higher than all our energy needs. The conversion of solar energy to electricity for direct use or storage in batteries can be achieved by photovoltaic cells. Conversion of solar energy to fuels involving storage of solar energy in the form of energy of chemical bonds is another way to harvest energy, also known as artificial photosynthesis. Advantage of using artificial photosynthesis over photovoltaic cells is that former gives the active fuel (like petrol, natural gas and etc.), which can be used for machines (car engines, heavy machinery, etc.)

which need to withdraw lot of power at once over a longer period. Solar fuels can be in the form of H_2, produced from photoassisted water splitting or high-energy carbon compounds (CO, HCOOH, or CH_3OH) that are produced by light-driven reduction of CO_2. Hydrogen has the highest energy density per unit weight compared to contemporary fuels with energy density of 142 MJ/kg compressed at 70 MPa while for methane gas it is 55.2 MJ/kg. Methane being the next to hydrogen in terms of energy efficiency. It is around 2.5 times as good as natural gas. Also, hydrogen is the cleanest source of energy as only by product of combustion of H_2 is water. This is why it has been advocated as the ultimate fuel for future. Figure 1. compare the energy density Hydrogen and the contemporary fuels used today.
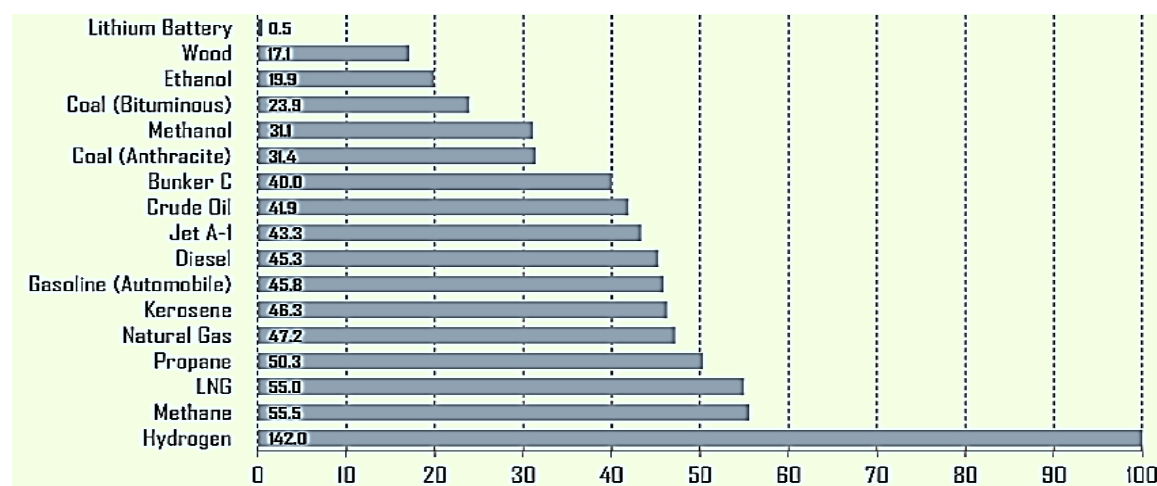
Figure.1 *Energy Efficiency (MJ/kg) of various fuels in comparison with Hydrogen. (adapted from C. Ronneau (2004), Energie, pollution de l'air et developpement durable, Louvain-la-Neuve: Presses Universitaires de Louvain.)*

Electrolysis of water, steam reforming biomass and photocatalytic or photoelectrochemical water splitting are the three approaches to Hydrogen. Photocatalytic water splitting being the simplest in design has been one of the most investigated field of research over the past several years.

In photocatalytic water splitting the energy of photons is converted to the chemical energy of H_2 by breaking the bonds in water. This process is accompanied by large positive Gibbs free energy of 238 kJ.mol^{-1}. This is endothermic reaction, as in natural photosynthesis, this is an uphill reaction and is difficult to perform unlike photocatalytic degradation of organic compounds, which is a downhill reaction. Water splitting involves two redox reactions involving four electrons:

Oxidation: $2H_2O \longrightarrow 4H^+ + O_2 + 4e^-$ (1.23V vs SHE)

Reduction: $4H^+ + 4e^- \longrightarrow 2H_2$ (0V vs SHE)
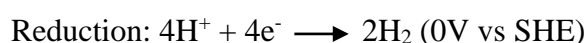
Plants perform this conversion through natural photosynthesis where CO_2 and water get converted to oxygen and carbohydrates. Photosynthesis occurs in two stages. In the first stage, water is oxidized to O_2 generating a proton which gets bound to $NADP^+$ to give the energy carrier, NADPH. In the second stage, NADPH is used to reduce CO_2 to glucose. Glucose is the fuel generated during photosynthesis similarly, we have H_2 as the fuel source generated during the artificial photosynthesis.

Natural Photosynthesis

In Figure 2, we show a schematic representation of natural photosynthesis. Solar energy is absorbed by chlorophyll and other pigments of PSII, which is the center for light-reaction in photosynthesis. P680 (containing chlorophyll a) or PSII absorbs a photon and loses an electron to pheophytin (a modified form of chlorophyll) generating P680$^+$. The redox potential of P680 is highly oxidizing while that of pheophytin is -0.5V so that it is able to reduce H^+ to H_2.[1] In order to reduce the probability of charge recombination the electron is transported from pheophytin, down, along a chain of molecules to photosystem I (PSI). This process of electron transfer down a chain of potential gradients ensures that the charge separation quantum efficiency of nearly 100% since the electron transfer processes happen on a femto-second time scale.
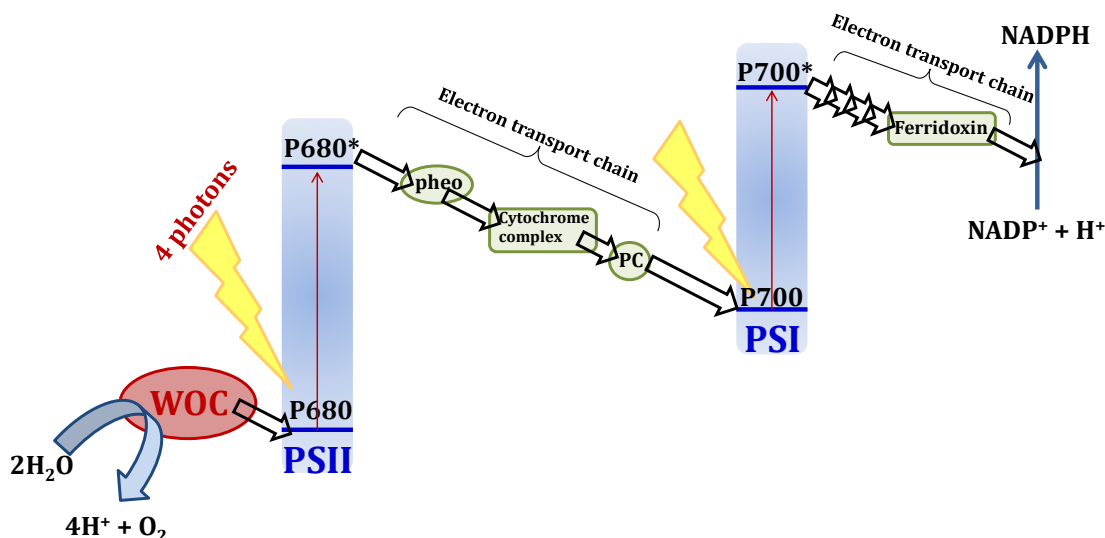
Figure 2. *Z-scheme of photosynthesis. PSI and PSII are photosystems I and II respectively, also known as P680 and P700. (adapted from reference [1])*

The electrons (e^-) and holes (h^+) have life times of μsec before charge recombination. $P680^+$ regains its electron from water thereby oxidizing it to O_2 in a reaction catalyzed by the water oxidizing center (WOC) which is a cubic Mn_4O_5Ca cluster encapsulated in a protein environment. In the meantime, P700 or PSI absorbs light and loses an electron to reduce H^+ and convert $NADP^+$ to NADPH thereby generating $P700^+$. The electron that travels down the cascade of steps to PSI is used up by $P700^+$.[1] This electron transport chain is commonly referred to as the **Z-scheme** of photosynthesis. Generation of O_2 from water is a 4 electron process as shown in reaction 1. PSII has to therefore absorb 4 photons to drive this half-reaction and PSI also has to absorb 4 photons for the subsequent reduction reaction. Absorption of two photons by the natural photosynthetic system generates one electron and one hole making the efficiency of this reaction almost 50%. However, considering that chlorophylls absorb nearly in the entire visible range and utilize only the red photons, the efficiency drops down to 20%. Forest harvest nearly ~5% of the total sunlight falling on the earth and natural photosynthesis in an agricultural crop is only 1% efficient over its entire life-cycle.[2]

Artificial Photosynthesis

Artificial photosynthesis provides is simple, has good efficiency and employs principles derived from natural photosynthesis. Artificial photosynthesis involves a photon absorbing center followed by a catalytic center with an electron and hole transfer pathway joining the two. This two process can either be a single-step or a two-step process which can be employed in artificial photosynthesis (Figure 3). In the single-step process, a photon absorber is directly attached to an electron donor on one side and/or an electron acceptor on the other or it can be the same species (catalyst). The photon absorber can be a semiconductor or a dye which absorbs light generating an electron-hole pair. The wavelength of light absorbed depends on the band gap of the semiconductor or the HOMO-LUMO gap of the dye as shown in Figure 3 (a). The semiconductor or dye is generally used in conjugation with an electron donor or an electron acceptor to enhance charge separation. An electron donor should have an energy level more negative than the excited state reduction potential of the semiconductor or the dye and at the same time more positive than the water oxidation potential. The electron acceptor would have an energy level more negative than the proton reduction potential and more positive than the excited state oxidation potential of the photon absorber. For swift electron transfer, acceptors and donors must be close to the photon absorber. Electron and hole transfer occurs directly from the energy levels of the semiconductor or the dye with only the electron donor or the electron acceptor or neither of them being used in the process of the reaction.
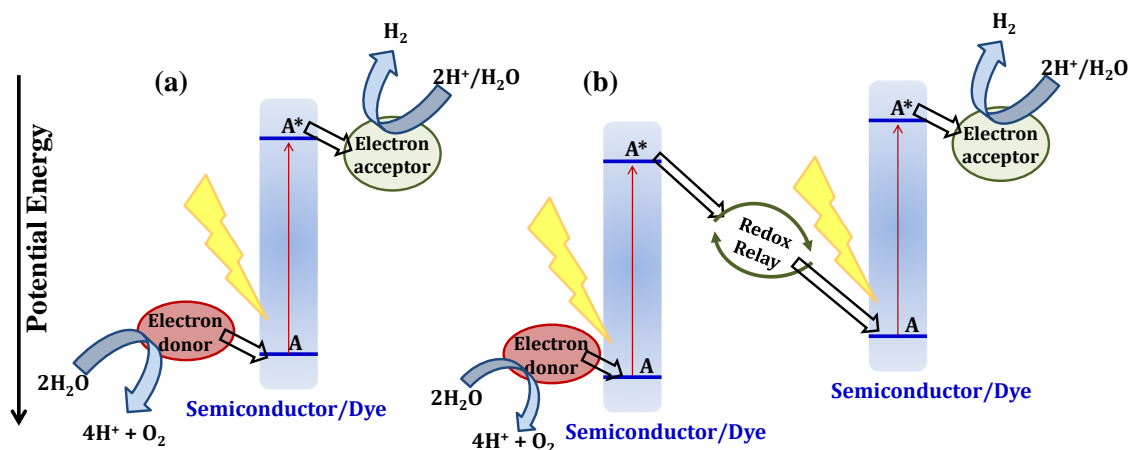
Figure 3. *Artificial photosynthesis by (a) single- and (b) two-step processes. (adapted from reference [11])*

In the two-step process, two photon absorbers are connected to each other by an electron transfer-relay material, the rest of the principles being similar to that of the single step process as shown in Figure 2 (b). A redox couple is used as the electron transfer relay. The two-step process is analogous to the Z-scheme of natural photosynthesis and utilizes two photons to generate one electron and one hole. In the case of the single-step process, on the other hand, the two components of the Z-scheme are combined into one. The single-step process is simple, but the disadvantage is that only a limited fraction of sunlight (<680 nm) can be used to initiate both the oxidation and reduction of water. The two-step process can be used for complete water splitting even with low excitation energy, as low as near-infrared wavelengths. This advantage is accompanied by the difficulty of maintaining the kinetics of the full electron-transfer process with minimal energy loss by charge recombination reactions. An ideal process of electron transfer is to have more than one electron acceptor or donor level closely spaced in energy as in natural photosysnthesis. However, this increases the complexity of the system and is somewhat difficult to achieve. Good electron acceptors like fullerenes[3,4] have been coupled with chromophores to achieve upto 95% charge separation. A simpler but less

effective strategy is to employ co-catalysts in semiconductor based light harvesters. Pt, Pd, NiO (for H_2) and RuO_2, IrO_2 (for O_2) satisfy the required conditions for use as catalysts.

The mechanism of photosysthesis (artificial or natural) thus comprises three aspects: i) light-harvesting, ii) charge generation and separation and iii) catalytic reaction as shown in Figure 3 (a). The photosynthetic catalysts can be classified as:

- Semiconductor- based photocatalysts

- Catalysts used in photoelectrodes.

- Dye-sensitized catalysts

✓ *Semiconductor-based photocatalysts*

These are the simplest of all catalysts with all the three processes of photosynthesis occurring in a single system. The semiconductor absorbs a photon with energy greater than its band gap and generates an electron-hole pair, followed by the migration of the electrons and holes to the surface of the semiconductor which participates in surface chemical reactions with water or other sacrificial agents.

For a semiconductor to act as a catalyst for water-splitting, it must satisfy the following energy level conditions. The bottom of the conduction band must be more negative than the reduction potential of H^+/H_2 (0 V vs. SHE), and the top of the valence band must be more positive than the oxidation potential of O_2/H_2O (1.23 V) as shown in Figure 4, limiting the theoretical minimum band gap for water splitting to 1.23 eV.
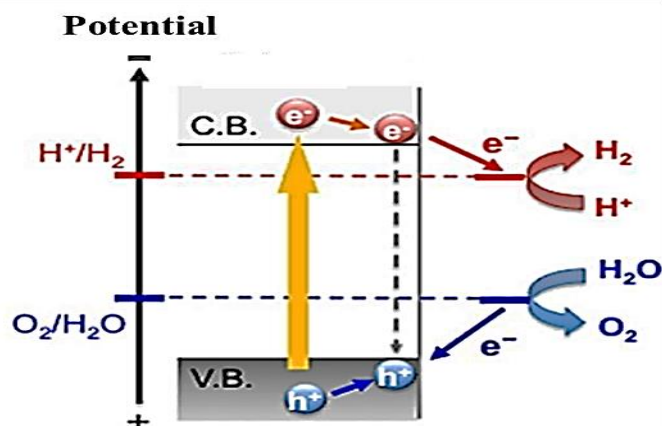
Figure 4. *The energy level requirements in semiconductor photocatalysis. (adapted from reference [5])*

Based on the above criterion, several semiconductors have been identified for H_2 evolution or oxygen evolution or both (Figure 5.). Semiconductors such as TiO_2, $SrTiO_3$, $BaTiO_3$, $FeTiO_3$, ZrO_2 and ZnO whose conduction band potential lie above the proton reduction potential can reduce water to produce H_2. On the other hand, semiconductors such as Fe_2O_3, SnO_2, $WO3$, *etc.* can only oxidize water. Semiconductor oxides, photocatalysts are highly stable with respect to sulfides and nitrides, and do not undergo oxidation or reduction during the processes of water splitting, they have an intrinsic limitation of having a highly positive valence band (O 2p). It is, therefore, difficult to find oxide semiconductors with a sufficiently negative conduction band to reduce H_2O to H_2, at the same time having a sufficiently small band gap to absorb visible light. [6] Metal sulfides and selenides (CdS, CdSe and MoS_2), on the other hand, ideal for visible light photocatalytic H_2 production by virtue of the sufficiently negative conduction band potential and small band gap (Figure 5.) [7].
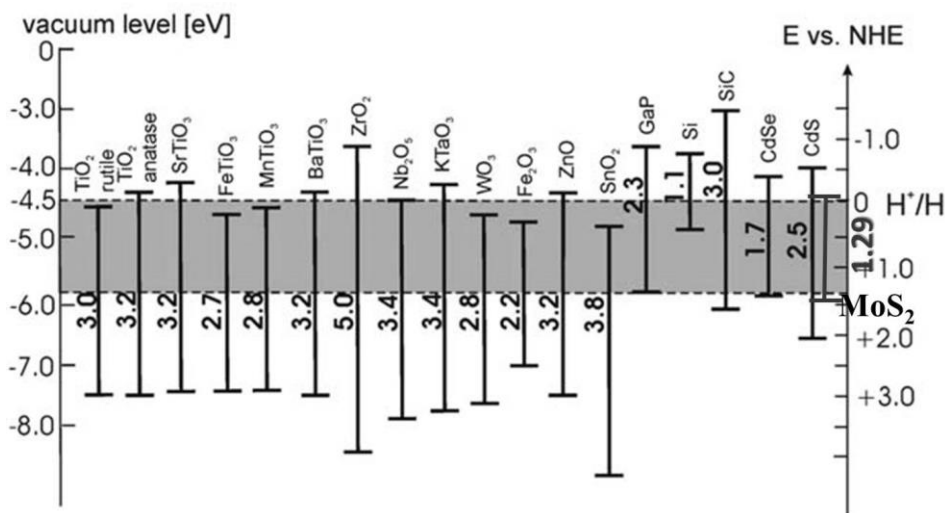
Figure 5. *Some semiconductor photocatalysts and their corresponding band positions with respect to the water redox potential. (adapted from reference [8])*

Recombination of e^- and h^+ competes with the process of charge separation reducing the efficiency of photocatalysis as illustrated in Figure 6. Grain boundaries and defects in the semiconducting particles act as charge recombination centers. Charge recombination can be minimized by decreasing the size of the particle to a few nm. [7] The electrons and holes would then have higher probability to traverse the surface and to be used to reduce and oxidize water respectively. Sometimes these can also be used up by a sacrificial electron or hole scavenger. A hole scavenger is a strong reducing agent such as an alcohol or a sulfide which gets oxidized by the photogenerated h^+ instead of water and thereby increases the system with electrons to be used for further reduction of water to generate H_2. Ag^+ and Fe^{3+} is used as electron scavengers for water oxidation. [7] A sacrificial system thus, eliminates back electron transfer and renders it feasible to examine only the oxidation or the reduction of water.
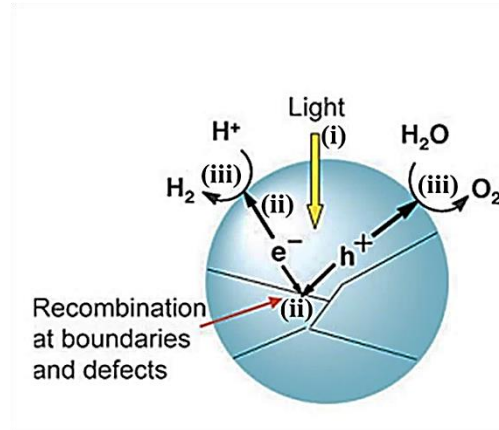
Figure 6. *Schematic representations of processes in photosynthesis (adapted from reference [2])*

✓ *Catalysts used in photoelectrodes*

In photo-electrocatalytic systems, the semiconductor acts as one of the electrodes of an electrochemical cell and is connected to the counter electrode via an external circuit. On absorbing light, the semiconductor generates the electron-hole pair. In the case of an n-type semiconductor photoelectrode, the photoexcited electron is transferred to the counter electrode (mostly Pt or Pt/C (wt 20 %)) via the external circuit where it reduces H^+ to H_2. The h^+ oxidizes water at the semiconductor surface.
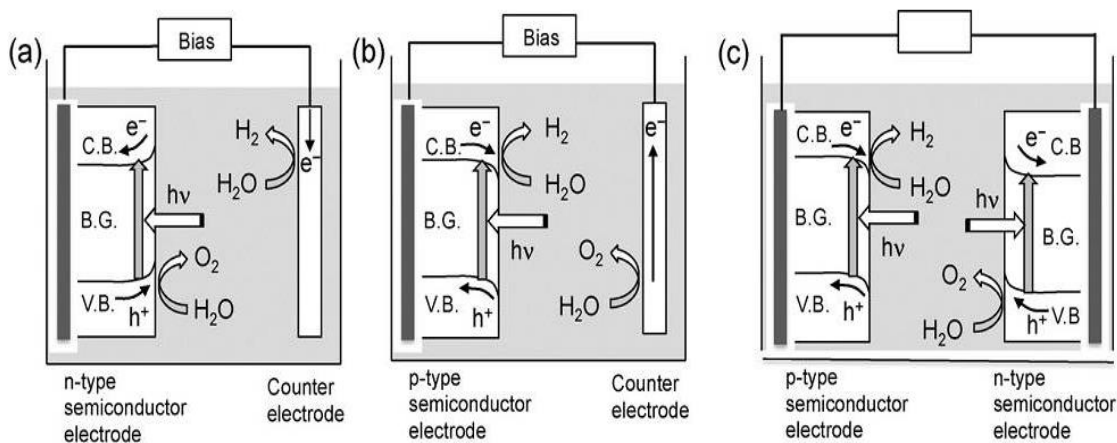
Figure 7. *Schematic representation of the processes of photo-electrochemical water splitting. (adapted from reference [2])*

In the case of a p-type semiconductor phototelectrode, the photogenerated electrons reduce water at the surface of the semiconductor while an electron from the counter electrode balances the h^+, oxidizing water at the counter electrode. The process of photo-electrochemical water splitting is demonstrated in Figure 7. Photo-electrochemical cells with both the anode and the cathode composed of photon absorbers have been used. Even though the semiconductor possesses suitable CB/VB levels for the reduction/oxidation of water, an external bias or a pH difference (chemical bias) needs to be maintained to overcome the resistance between the two electrodes in solution and at the interface between the solution and the semiconductor electrode. Here, charge-recombination is inhibited by the bias leading to greater efficiency, with the quantum yield approaching unity and a power conversion efficiency of ~18%.[9]

✓ *Dye-sensitized catalysts*

Use of semiconductors as photocatalysts imposes a limitation on the band gap of the semiconductor. Semiconductors with a large band gap absorb light in the UV region neglecting the entire visible and near infrared regions of the solar spectrum. Dye sensitization permits the use of semiconductors with energy levels matched with the redox potential of water, without compromising with the range of energies absorbed. On illumination with visible light, the excited dye transfers an electron to the conduction band of the semiconductor provided the excited state oxidation potential of the dye is more negative than the conduction band of the semiconductor (Figure 8) and the dye itself gets oxidized. A sacrificial electron donor or a redox shuttle such as the I^{3-}/I^- pair is used to regenerate the photosensitizer and sustain the reaction cycle. Photosynthesis broadens the spectrum response range and increases the efficiency of charge transfer by spatial separation of the electron and the hole
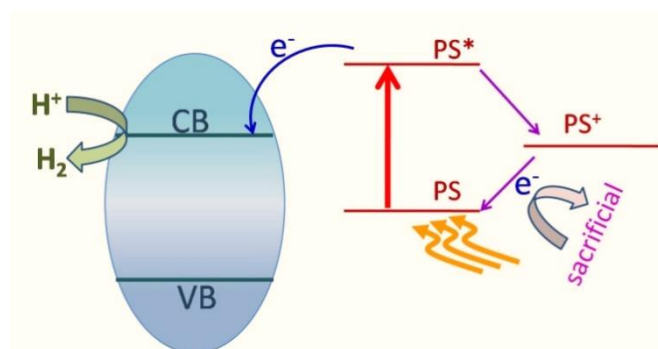
Figure 8. *Schematic representation of dye-sensitized H_2 evolution. (PS represents a photosensitizer/dye)*

Dye-sensitized photo-electrochemical cells having dye-sensitized photo electrodes also work on similar principles with the reduction of water occurring at the counter electrode and the sacrificial agent getting oxidized at the photosensitized electrode. Dye sensitized TiO_2 electrodes bearing IrO_2 nanoparticles have been used for complete water splitting. On sensitization, the dye loses an e^- to TiO_2 which transfers to the counter (Pt) electrode generating H_2. The IrO_2 particles donate e^- to the oxidized dye to regenerate the photosensitizer. [10]

In the following three chapters we have dealt with understanding the process of water oxidation and hydrogen evolution separately. In natural systems water oxidation happens during the light-reaction of photosynthesis at PSII. The water oxidation center is composed of water oxidizing complex called the WOC. In order to develop efficient catalysts for water oxidation with earth abundant and cost effective elements much study has been conducted on understanding and mimicking the WOC. Several metal complexes, hybrids and inorganic oxides having structure and composition similar to the core of WOC have been studied. In the first chapter we have studied the role and importance of Co^{3+} and Mn^{3+} behind water oxidation by inorganic transition metal oxides keeping in mind that oxidation state of the transition metal ion in WOC plays a crucial role in determining its catalytic properties.

We have tried to study the role transition metal dichalcogenides in water splitting. Transition metal dichalcogenides have become of great interest because of their lamellar structure like graphene and versatility in electronic properties. They can be used to serve various we have used TiS_2 and TaS_2 composite with CdS. Both TiS_2 and TaS_2 were inactive as catalyst but act as co-catalyst by enhancing the photocatalytic activity of the CdS. Also it supports that the metallic nature of the co-catalyst enhances the activity of the photocatalytic. Proton reduction to hydrogen is carried out naturally by hydrogenase an enzyme that catalyzes reduction of proton accompanied by oxidation of electron donors such as ferridoxin. Recently, it has become possible to anchor hydrogenase to an electrode surface, [11] and considerable progress has been made in the synthesis of compounds in solution resembling the hydrogenase active site and showing activity for hydrogen evolution. [12,13] Recently, MoS_2 has been identified to have free energy for H_2 evolution comparable to that of nitrogenase and hydrogenase with the edge structure of MoS_2 sheets having close resemblance with the catalytically active sites of these enzymes. In the second chapter we have studied the photocatalytic properties of two polymorphs of MoS_2 and their composites with graphene. To study the catalytic properties of inorganic transition metal oxides and MoS_2 dye sensitization technique has been utilized with sacrificial electron donors and acceptors present in solution.

In this thesis following studies are presented:

Chapter 2: Visible light induced oxidation of water by rare earth manganites, cobaltites and related oxides.

Chapter 3: Water Splitting based on few-layer TiS_2 and TaS_2.

Chapter 4: Highly Effective Visible-Light-Induced H_2 Generation by 2H and 1T forms MoS_2 and $MoSe_2$

References

1. Y. Tachibana, L. Vayssieres and J. R. Durrant. **Nat. Photon.** 2012, 6, 511.

2. R. Abe. **J. Photochem. Photobio. C,** 2010, 11, 179.

3. D. González-Rodríguez, E. Carbonell, G. d. M. Rojas, C. A. Castellanos, D. M. Guldi T. Torres. **J. Am. Chem. Soc.** 2010, 132, 16488.

4. G. Kodis, P. A. Liddell, A. L. Moore, T. A. Moore and D. Gust. **J. Phys. Org. Chem**. 2004, 17, 724.

5. A. Kudo and Y. Miseki. **Chem. Soc. Rev.** 2009, 38, 253.

6. X. Chen, S. S. Mao, **Chem. Rev.,** 2007, 107, 2891

7. K. Zhang and L. Guo, **Catal. Sci. Technol.,** 2013,3, 1672

8. A. L. Linsebigler, G. Lu, J. T. Yates, **Chem. Rev. ,** 1995, 95, 735

9. M. Batzill. **Energy Environ. Sc.** 2011, 4, 3275.

10. E. R. Kleinfeld and G. S. Ferguson. **Science** 1994, 265, 370.

11. W. J. Youngblood, S.-H. A. Lee, K. Maeda and T. E. Mallouk. **Acc. Chem. Res.** 2009, 42, 1966.

12. S. E. Lamle, K. A. Vincent, L. M. Halliwell, S. P. J. Albracht and F. A. Armstrong. **Dalton Trans.** 2003, 4152.

13. R. Mejia-Rodriguez, D. Chong, J. H. Reibenspies, M. P. Soriaga and M. Y. Darensbourg. **J. Am. Chem. Soc.** 2004, 126, 12004.

14. T. B. Rauchfuss. **Inorg. Chem.** 2003, 43, 14.

Chapter 2

Visible- light- induced oxidation of water by rare earth manganites, cobaltites and related oxides

Summary*

A study of the visible light induced oxidation of water by perovskite oxides of the formula $LaMO_3$ (M = transition metal) has revealed the best activity with $LaCoO_3$ which contains Co^{3+} in the intermediate-spin (IS) with one e_g electron. Among the rare earth manganites, only orthorhombic manganites with octahedral Mn^{3+} ion $(t^3_{2g}\ e^1_g)$ exhibit good catalytic activity, but hexagonal manganites are poor catalysts. Interestingly, not only the perovskite rare earth cobaltites but also solid solutions of Co^{3+} in cubic rare earth sesquioxides exhibit catalytic activity comparable to $LaCoO_3$, the Co^{3+} ion in all these oxides also being in the intermediate-spin state $t^5_{2g}\ e^1_g$. Octahedral Mn^{3+} and Co^{3+} ions with e^1_g configuration are responsible for the oxygen evolution reaction (OER).
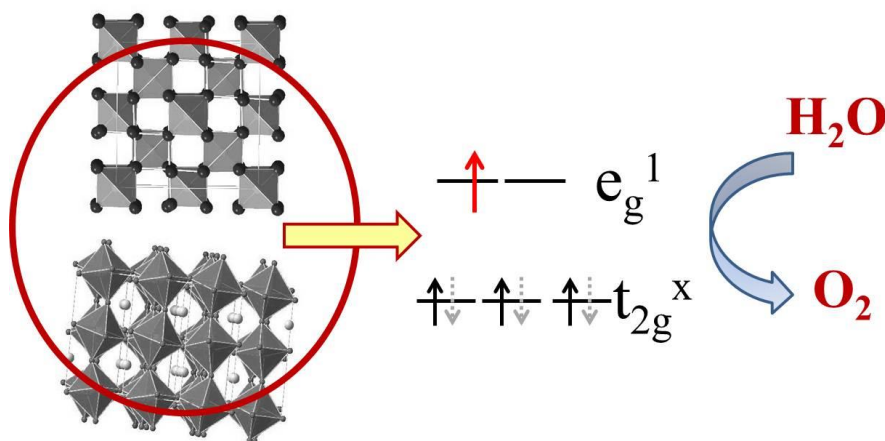
Introduction

As mentioned earlier, any strategy for solving the energy crisis would include the generation of fuels through artificial photosynthesis, involving the sun as the only source of energy. In order to complete the solar cycle, water has to act as the source of electrons, either to generate liquid fuels by the reduction of CO_2 or to yield H_2 through a complete cycle of transfer of electrons. Photovoltaics have been used for production of H_2, but cost of photovoltaic solar cells marginalizes the use of this route for the purpose. The challenge is to develop a water-splitting catalyst that is robust and composed of earth abundant non-toxic materials.

Due to the increase in energy needs, depletion of fossil fuels and environmental concerns, extensive search for clean, renewable and inexpensive form of energy is being perused. Solar energy, an abundant source of energy can only be used by converting it into a useful form of energy [1, 2]. Photocatalytic water splitting using sunlight to generate hydrogen, which is a clean form of energy, has thus emerged to be an important approach to solving the energy crisis [2]. In photocatalytic water splitting, oxidation of water involving the transfer of four electrons is the energy intensive step and it has therefore become necessary to find good visible light active catalysts for water oxidation [3]. While IrO_2 and RuO_2 are good water oxidation catalysts, they are expensive and scarce [4–8]. Careful photocatalytic water oxidation studies have indicated that cobaltites show better activity than manganites while nickelites and ferrites show poor activity. Furthermore, orthorhombic manganites show much higher activity than the hexagonal manganites. In the case of cobaltites of heavy rare earths such as Dy, Er, Yb and Y, the oxides obtained from the citrate gel decomposition depends on the reaction temperature, those prepared around or below 700^oC generally exist as cubic solid solutions of Ln_2O_3 and Co_2O_3 (space group Ia-3). We have examined the

photocatalytic activity of these solid solutions containing Co(III) ions and found it to be comparable to that of the perovskites. In order to be able to strictly compare catalytic performance of the various oxide materials, we have measured the oxygen evolved per mole of transition metal per unit surface area.

Scope of the present investigations

Catalysts based on Mn and Co oxides are inexpensive and there have been efforts to investigate the photocatalytic properties of these oxides for the production of oxygen [9–19]. It has been shown recently that trivalency of Co and Mn ions as well as the e^1_g electronic configuration are crucial factors in determining the catalytic activity [20]. Catalytic activity for electrochemical oxygen evolution by lanthanide perovskites is also suggested to be dependent on the 3d-electron occupancy in the e_g orbitals of B site cations [21]. Thus, Mn_2O_3 and $LaMnO_3$ with Mn(III) in the $t^3_{2g} e^1_g$ configuration as well as $Li_2Co_2O_4$ and $LaCoO_3$ with Co(III) in the $t^5_{2g} e^1_g$ configuration are found to be excellent catalyst for photocatalytic water oxidation [20]. We considered it to be of vital interest to explore the catalytic activity of a related series of perovskite, cobaltites and maganites of the type $LnCoO_3$ and $LnMnO_3$ (Ln = rare earth) and also of related oxides.

We have examined the photocatalytic activity of solid solutions containing Co(III) ions and found it to be comparable to that of the perovskites. In order to be able to strictly compare catalytic performance of the various oxide materials, we have measured the oxygen evolved per mole of transition metal per unit surface area.

Experimental Section

Synthesis

LnMO$_3$ (Ln=La, Pr, Nd, Sm, Dy, Y, Yb, Gd, Er and M=Mn, Co, Ni, Fe, Cr): All these materials were synthesized by citrate sol-gel method.

Mn(CH$_3$COO)$_2$.4H$_2$O, Co(CH$_3$COO)$_2$.4H$_2$O, Fe(NO$_3$)$_3$.9H$_2$O, Cr(NO$_3$)$_3$.9H$_2$O, Ni(NO$_3$)$_2$.6H$_2$O, Li$_2$CO$_3$, anhydrous citric acid, urea and conc. HNO$_3$ (70%) were used as starting materials.

In a typical synthesis procedure, 5 mmoles of lanthanum nitrate and 5 mmoles of transition metal nitrate were dissolved in 30 mL of distilled water. To this solution, 50 mmoles of anhydrous citric acid was added and heated to 80 °C while stirring to form gel and maintained at this temperature till dryness (around 9 h). This gel was kept in an electrical oven at 200 °C for 12 h and a small part of this gel was heated at required temperatures after grinding. For preparing lanthanide manganites, precursor citrate-gel was heated at 800 °C for 5h with heating rate of 7 °C/min whereas for lanthanide ferrites and lanthanide nickelites heated at 700 °C for 5 h. In case of orthorhombic lanthanide cobaltates, the heating temperature was varied with lanthanidesand details are given in Table.1

Powder X-ray diffraction (XRD) measurements were carried out with Bruker D8 Advance diffractometer using Cu Kα radiation. The average crystallite size was calculated by using Debye-Scherrer formula $t = 0.9\lambda/(\beta Cos\theta)$, where β is the full width at half maxima in radians, λ is the wavelength of X-rays, θ is the Bragg angle. Particle size was also examined from transmission electron microscope (TEM) images obtained with a JEOL

JEM 3010 operating at an accelerating voltage of 300 kV. Surface area was determined from N_2 adsorption measurements carried out in Quanta-chrome Autosorb instrument at 77K. Magnetic measurements were carried out with a vibrating sample magnetometer in the magnetic property measurement system (MPMS-SQUID VSM) of Quantum Design, USA.

Oxygen evolution measurements

Oxygen evolution measurements were carried out using oxygraph instrument, Hansatech Ltd, equipped with Clark type oxygen electrode. Calibration of the oxygen electrode was done with air saturated Millipore water and then deoxygenated by N_2 purging. Throughout all the measurements, temperature of the reaction chamber was maintained at 25 °C by using Julabo F 25 pump. In the reaction chamber, 0.022 M Na_2SiF_6 and 0.028 M $NaHCO_3$ buffer, 1.5 mM $[Ru(bpy)_3]Cl_2 \cdot 6H_2O$, 20 mM $Na_2S_2O_8$ and 80 mM Na_2SO_4 and 100 ppm catalyst was added. Total volume of the solution was 2 mL the solution was stirred continuously throughout the reaction with 100 rpm speed. The catalyst solution was sonicated for 5-10 min prior to adding into the reaction vessel. All the solutions were made freshly every day. This solution was purged with nitrogen till all the oxygen was purged out then the reaction chamber was closed with air tight plunger and waited till the oxygen level was constant. Then the reaction vessel was illuminated with 100W halogen lamp and small percentage of UV light was filtered with BG 38 filter. Light intensity was kept at 25,000 Lux.

Table.1. *Calcination conditions, crystallite size calculated from XRD, BET surface area measured by N_2 absorption at 77K, O_2 evolved per mole of catalyst, O_2 evolved per mole of catalyst per unit surface area of lanthanide manganites, cobaltites, ferrites and nickelates.*

Sample name	Calcination temperature (°C) and duration (h)	Crystallite size (nm)	BET Surface area (m^2/g)	O_2 evolved (mmole/ mole of catalyst)[&]	O_2 evolved (mmole/ mole of catalyst. m^2)[&]
[@]$LaMnO_3$	800, 5h	18	24	197	8.2
[@]$LaFeO_3$	700, 5h	19	29	48	1.7
[@]$LaCoO_3$	500, 8h	16	14	687	49
[@]$LaNiO_3$	700, 5h	14	12	76	6.3
$NdMnO_3$	800, 5h	26	12	131	10.9
$SmMnO_3$	800, 5h	32	11	114	10.3
$GdMnO_3$	800, 5h	35	9	107	11.9
$DyMnO_3$	800, 5h	33	13	116	8.9
[#]$YMnO_3$	800, 5h	23	20	39	1.9
[#]$YbMnO_3$	800, 5h	27	15	59	3.9
$PrCoO_3$	500, 8h	23	14	532	38
$NdCoO_3$	500, 8h	24	12	415	34.5
$SmCoO_3$	500, 8h	29	16	498	31.2
$GdCoO_3$	700, 8h	47	8	273	34.1
$DyCoO_3$	800, 8h	67	3	114	38
[!]$(Dy_2O_3) (Co_2O_3)$	500, 8h		13	471	36.2
[!]$(Y_2O_3) (Co_2O_3)$	500, 8h		24	468	19.5
[!]$(Er_2O_3) (Co_2O_3)$	500, 8h		16	634	39.6
[!]$(Yb_2O_3) (Co_2O_3)$	500, 8h		14	582	41.6

[@]Rhombohedral/Cubic perovskite,[#] Hexagonal Perovskite [!]Cubic (solid solution) Rest all are Orthorhombic Perovskites,[&] After 15 min of illumination

Results and Discussion

The process used to study water oxidation was designed similar to natural photosynthesis as shown in the Scheme (a). Chlorophyll acts as the photosensitizer in plants, $[Ru^{III}(bpy)_3]^{2+}$ was used in our processes and the photoexcited electron instead of being used up by CO_2 is taken up irreversibly by $Na_2S_2O_8$. The catalyst thus plays the exact role as that of the WOC (Water Oxidising Complex), donating electrons to regain the photosensitizer oxidizing water in the processes. Oxygen evolution property of the catalysts were studied under visible light in standard photoexcitation system[29] consisting of $[Ru^{III}(bpy)_3]^{2+}$ as photosensitizer and $Na_2S_2O_8$ as sacrificial electron acceptor in a solution buffered at pH = 5.8. The singlet $[Ru(bpy)_3]^{2+}$ on photoexcitation goes to triplet state denoted as $[Ru(bpy)_3]^{2+*}$. The species transfers its electrons to the sacrificial oxidant $S_2O_8^{2-}$. The resulting $[Ru(bpy)_3]^{3+}$ takes an electron from the metal oxide catalyst which in turn oxidizes water to molecular O_2, as demonstrated in Scheme (b). Oxygen evolved was quantified both by Clark type electrode.
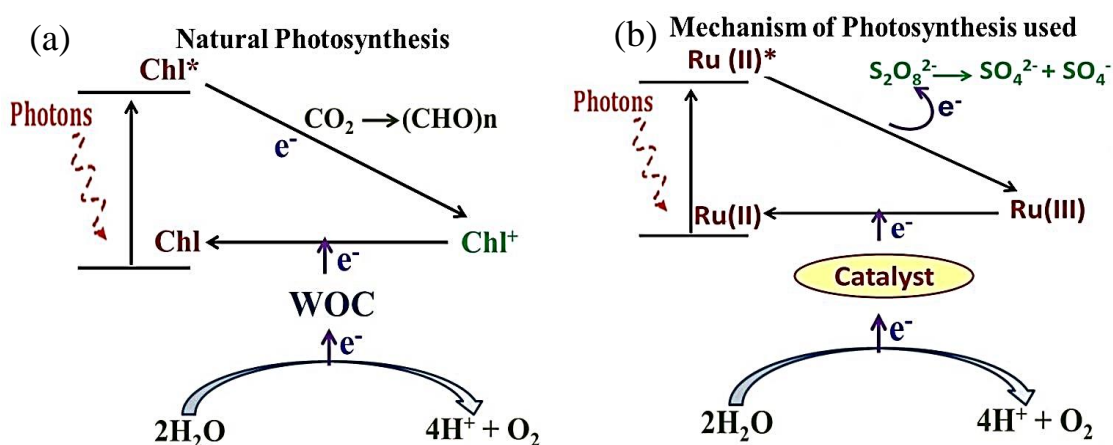
Scheme 1. *Comparison the processes used for photosynthetic oxidation of water with that of natural photosynthesis.*
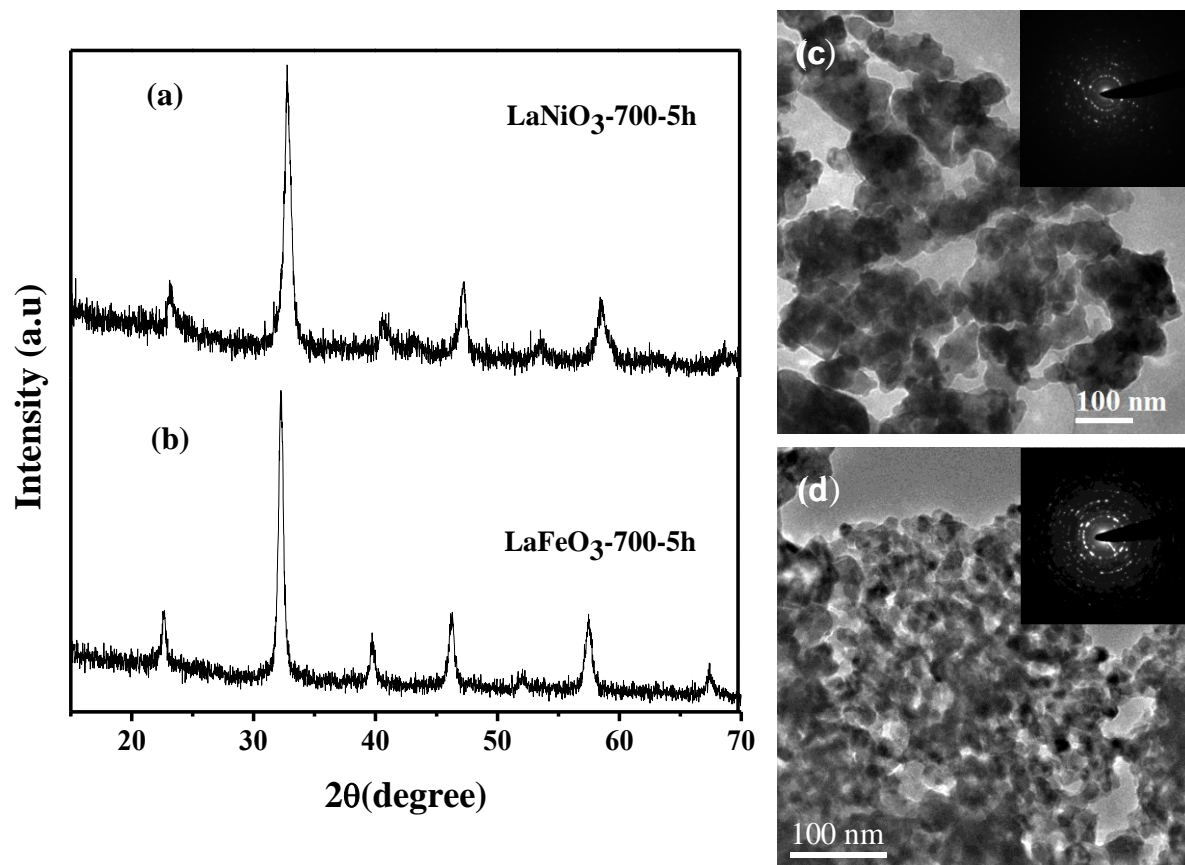
Figure 1. *(a), (b) XRD patterns and (c), (d) TEM images of LaNiO₃, LaFeO₃ respectively*

In order to be able to strictly compare catalytic performance of the various oxide materials, we have measured the oxygen evolved per mole of transition metal and normalized it with respect to BET surface area of the catalyst. Turn over frequencies (TOF) for each catalyst was calculated from the initial slope of O_2 evolved per mole of transition metal vs. time plot. In order to establish the role of the electronic configuration of the transition metal ion on the photocatalytic water oxidation, we first examined the photochemical catalytic activity of lanthanum perovskites of the formula $LaMO_3$ (M= Cr, Mn, Fe, Co and Ni). The crystallite sizes of these oxides obtained from X-ray diffraction patterns (Figure. 1) as well as their BET surface areas are listed in Table.1. The particle sizes obtained from TEM images are in the range 15-55 nm.

Oxygen evolution properties of these materials per mole of transition metal are shown in Figure. 2(a). $LaCoO_3$ shows the best water oxidation activity with a TOF of 1.4×10^{-3} s^{-1} followed by $LaMnO_3$ (4.8×10^{-4} s^{-1}). $LaNiO_3$ (1.2×10^{-4} s^{-1}) and $LaFeO_3$ (8.9×10^{-5} s^{-1}) show poor activity. $LaCrO_3$ does not show any oxygen evolution catalytic activity under similar conditions.
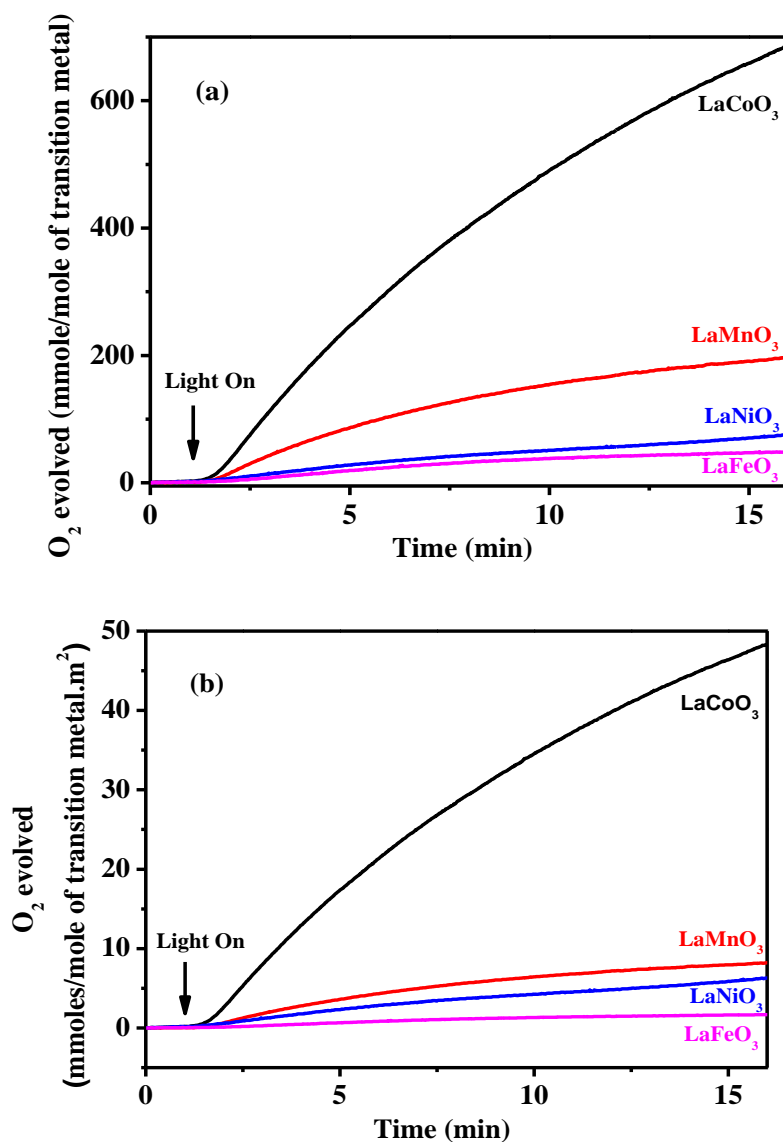
Figure 2. *O_2 evolved by $LaMO_3$ (M: Mn, Fe, Co and Ni) (a) per mole of transition metal, (b) per mole of transition metal per unit surface area.*

The oxygen evolved per mole of transition metal per unit surface area shown in Figure. 2(b) follows the same order as in Figure. 2(a). The oxygen evolved per mole of transition metal per unit surface area of $LaCoO_3$, $LaMnO_3$, $LaNiO_3$ and $LaFeO_3$ after 15 min are 48.3, 8.2, 6.3 and 1.7 mmoles/mole of ransition metal.m^2 respectively. We next studied the catalytic activity of the series of manganites $LnMnO_3$ with Ln= La, Nd, Sm, Gd, Dy, Y and Yb for the oxidation of water, having prepared all the manganites by citrate gel decomposition at 800°C. The manganites of Nd, Sm,Gd and Dy crystallize in the orthorhombic structure (space group Pbnm) whereas those of yttrium and ytterbium crystallize in the hexagonal structure (space group $P6_3cm$). $LaMnO_3$ crystallizes in rhombohedral phase.
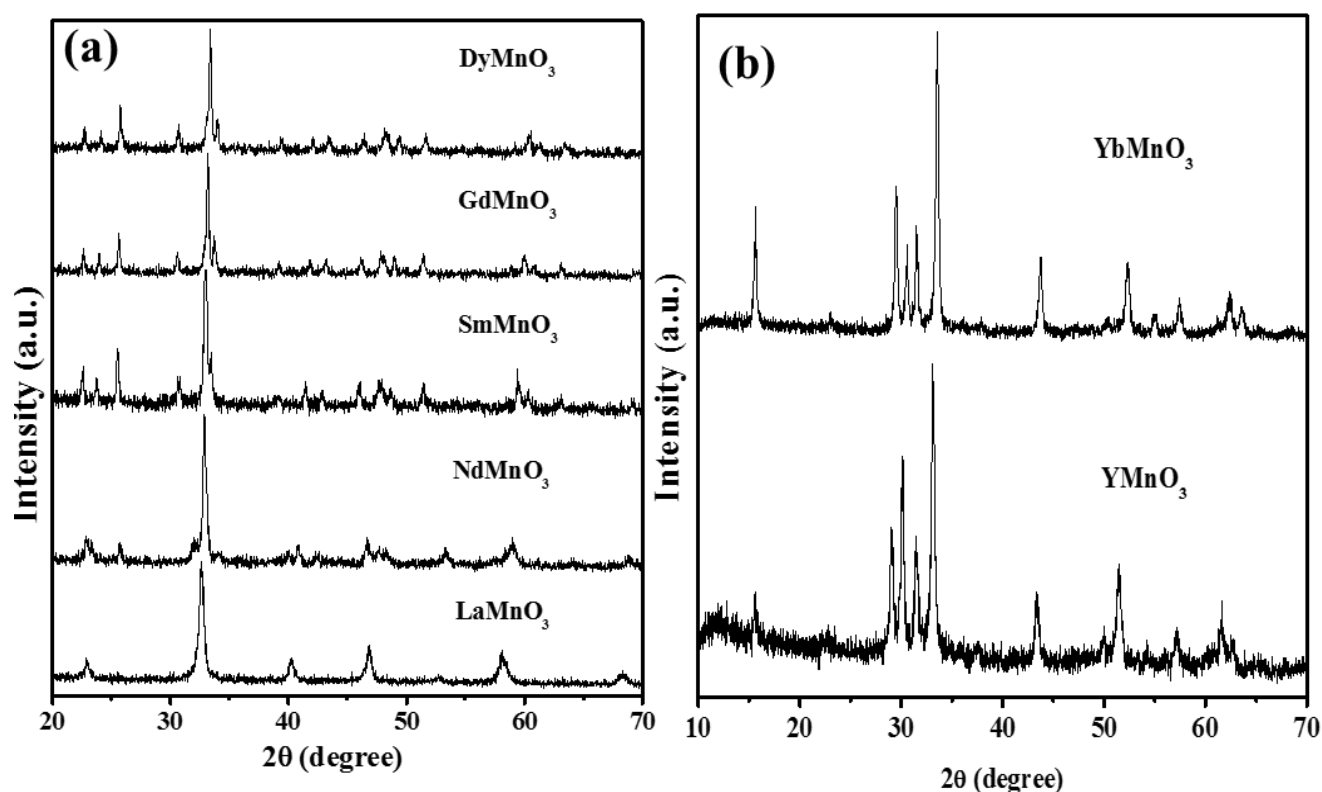
Figure 3. *XRD patterns of (a) orthorhombic (b) hexagonal lanthanide manganates prepared at 800 °C*

The XRD patterns of the manganites are given in Figure. 3. TEM images showed that the oxide materials were composed of crystalline nanoparticles (Figure. 4).
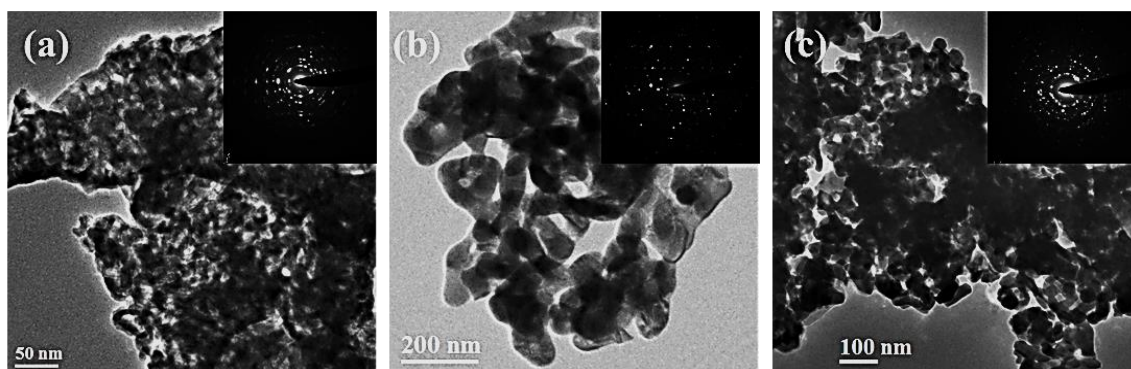
Figure 4. *TEM images of (a) LaMnO₃, (b) GdMnO₃, (c) YbMnO3. In insets respective SAED patterns were showed.*

The electron diffraction (ED) patterns shown in the inset of Figure. 4 confirm the crystalline nature of the catalysts. The crystallite size calculated from XRD patterns and the BET surface areas obtained from N_2 absorption at 77K are listed in Table.1. We have plotted the O_2 evolved per mole of manganese ion in Figure .5(a). Among the manganites, LaMnO₃ shows the highest catalytic activity with a TOF of 4.8×10^{-4} s^{-1}. All the other orthorhombic manganites (Ln= Nd, Sm, Gd and Dy) have comparable catalytic activities with a TOF between 2.4×10^{-4} s^{-1} and 2.1×10^{-4} s^{-1} corresponding to 119±7 mmole of O_2 per mole of Mn after 15 min of illumination. The hexagonal manganites (Ln= Y and Yb), on the other hand, show much lower O_2 yield of 49±10 mmole per mole of Mn after 15 min of illumination with a TOF of 5.2×10^{-5} s^{-1} for YMnO₃ and 9.2×10^{-5} s^{-1} for YbMnO₃. The data on oxygen evolved per mole of Mn per unit surface area are shown in Fig.5 (b). The rare earth manganites with the orthorhombic structure, including LaMnO₃ show somewhat comparable oxygen evolution of 10±1.8 mmoles/mole of Mn.m^2.

The hexagonal manganites show much lower values of O_2 evolved, in the range of 2.9 ± 1 mmoles/mole of Mn.m^2. Clearly, orthorhombic perovskite manganites show better catalytic activity as compared to hexagonal perovskites for photocatalytic water oxidation. It must be noted that in all these oxides, Mn is in +3 oxidation state.
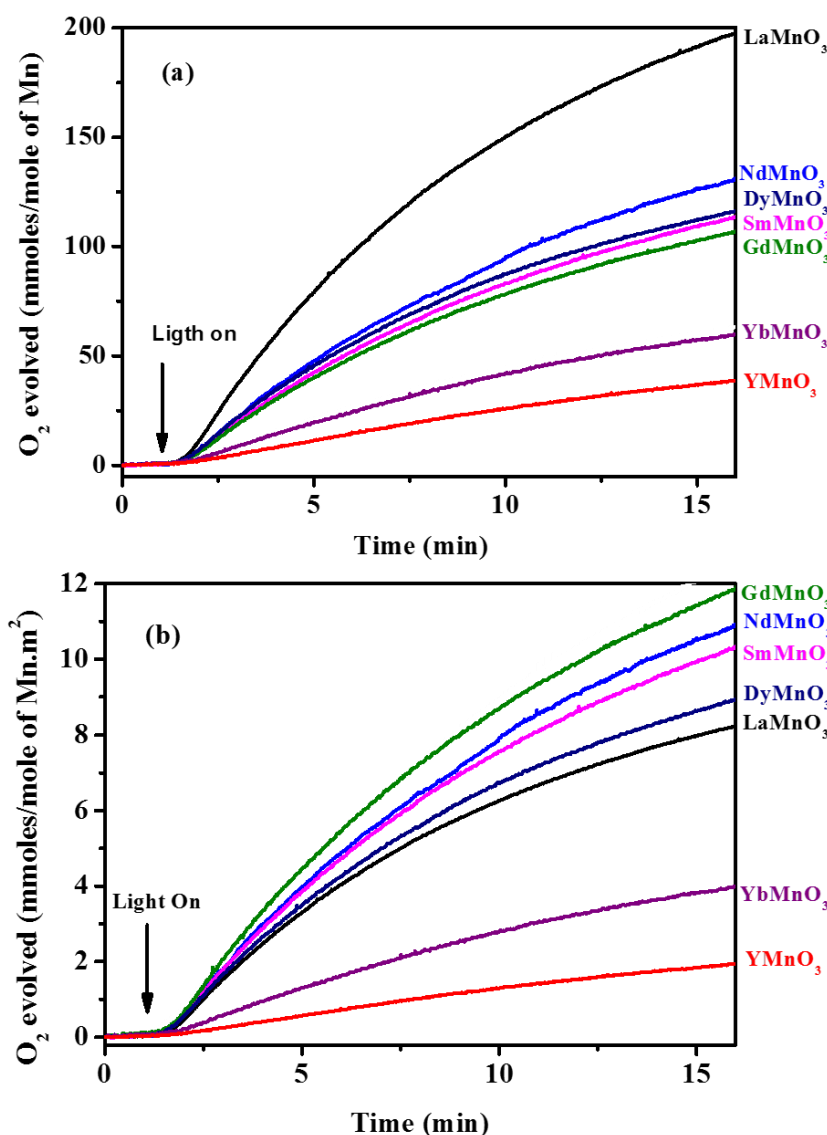
Figure 5. *O_2 evolved by rare earth manganates (a) per mole of Mn, (b) per mole of Mn per unit surface area*

The difference in the oxygen evolution catalytic activity between the orthorhombic and hexagonal manganites is considered to depend on the electronic configuration of Mn^{3+} (d^4)

ion which is determined by the nature of coordination. In the orthorhombic and rhombohedral manganites, Mn(III) exists in octahedral coordination and the electronic configuration is $t_{2g}^3 e_g^1$ which causes Jahn-Teller distortion of the octahedral [22]. In hexagonal manganites, Mn(III) exists in trigonal bipyramidal symmetry (MnO_5), the electronic configuration being $e''^2 e'^2 a_1'^0$ [22-24].

We have prepared several rare earth cobaltites, $LnCoO_3$ (Ln= Pr, Nd, Sm, Gd and Dy) with the orthorhombic crystal structure and $LaCoO_3$ with rhombohdral structure, by heating citrate gels to relatively high temperatures and examined their photocatalytic water oxidation properties. The XRD patterns of the cobaltites are shown in Figure. 6, and their crystallite size and BET surface areas listed in Table.1.
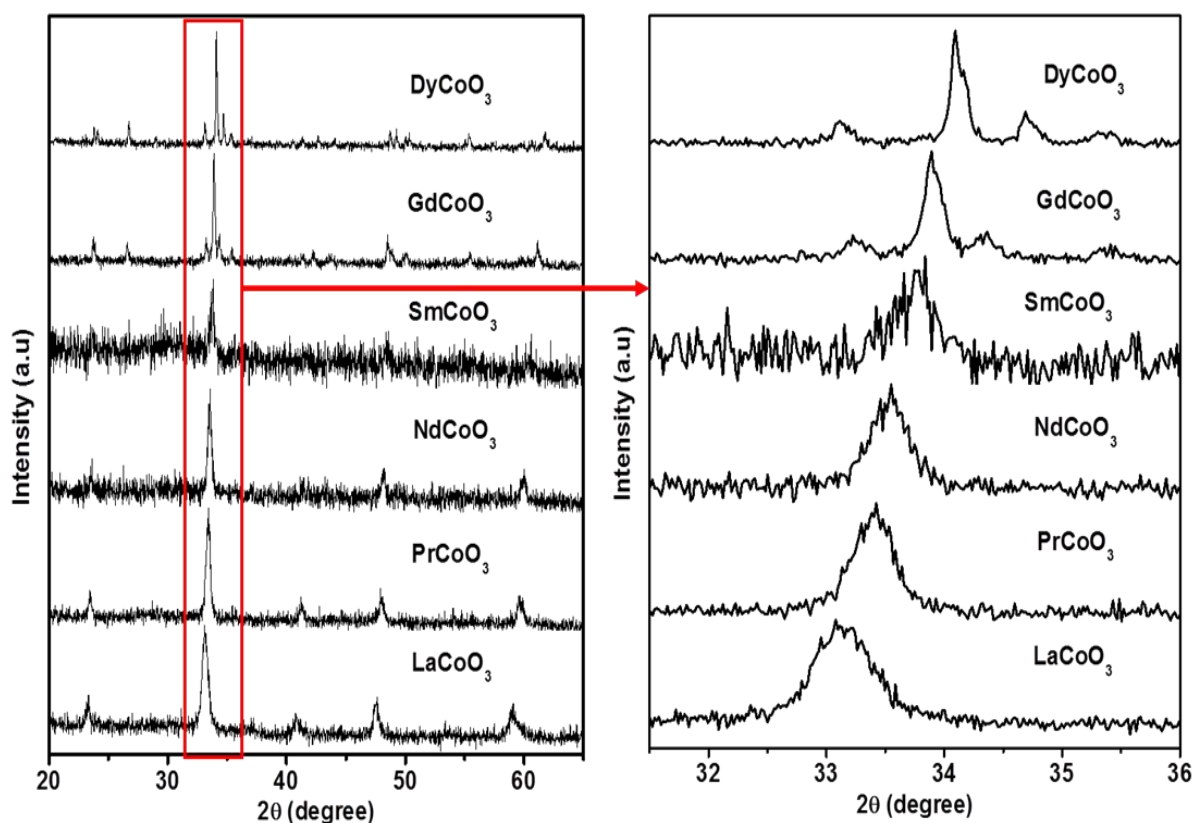
Figure 6. *XRD patterns of orthorhombic LnCoO₃ (Ln:La, Pr, Nd, Sm, Gd and Dy)*

The oxygen evolved by these orthorhombic cobaltites per mole of Co are presented in Figure 7(a). $LaCoO_3$ exhibits the best oxygen evolution catalytic activity with a TOF of 1.4×10^{-3} s^{-1}. $DyCoO_3$ shows poor catalytic activity with a TOF 2.8×10^{-4} s^{-1}. All the other cobaltites show catalytic activity between these two. On calculating the O_2 evolution activity per unit surface area, $LaCoO_3$ (Rhombohedral, $R\overline{3}C$) remains the most active catalyst with the 49 mmoles/mole of Co.m^2 while all orthorhombic cobaltites show comparable activities with a yield of 34.6 ± 3.4 mmoles/mole of Co.m^2 as shown in Figure. 7(b).
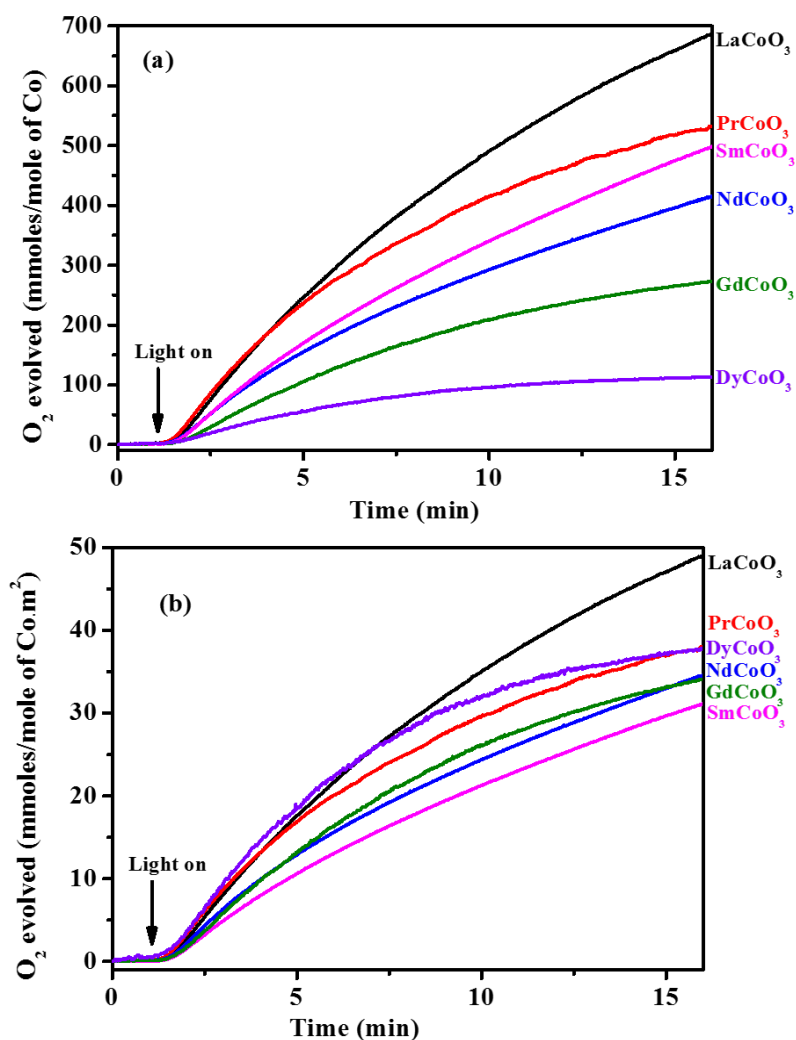
Figure 7. *O_2 evolved by rare earth cobaltates (a) per mole of Co, (b) per mole of Co per unit surface area*

It is reported that monophasic orthorhombic $YbCoO_3$ cannot be prepared on heating the citrate gel even to high temperatures [25]. What one gets instead is a solid solution of Co_2O_3 in Yb_2O_3 in the cubic rare earth oxide structure, with the cobalt in the +3 state. We prepared the solid solutions of the formula (Ln_2O_3) (Co_2O_3), (Ln = Dy, Y, Er and Yb) with the cubic structure by heating the citrate gels to 700°C or lower. The XRD patterns of the Dy-Co-citrate gel heated at different temperatures are shown in Figure. 8(a) along with the XRD patterns of Dy_2O_3 (Figure. 8(b)) prepared by the same method.
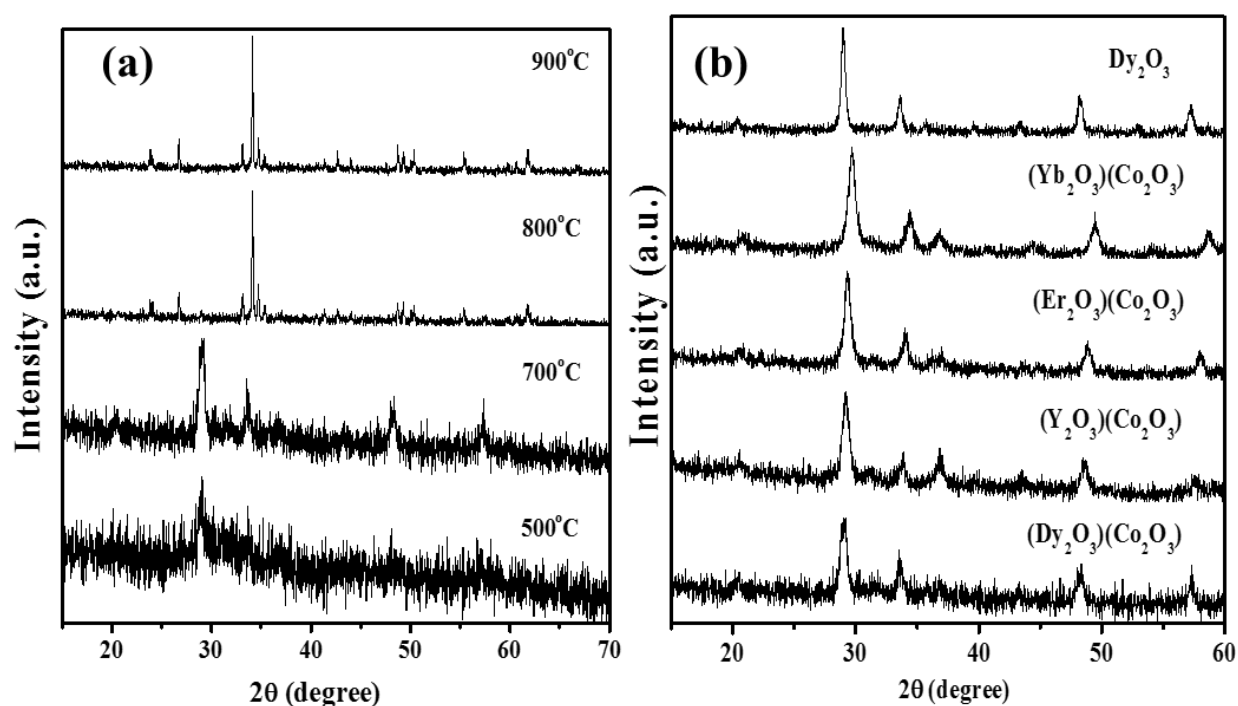
Figure 8. *XRD patterns of (a) Dy, Co citrate gel heated at 500°C, 700°C, 800°C, 900°C, (b) $(Ln_2O_3)(Co_2O_3)$ (Ln: Dy, Y, Er, Yb) solid solutions and Dy_2O_3 prepared at 700 °C*

The gel heated at 500°C and 700°C yields oxides crystallizing in the cubic structure similar to Dy_2O_3 and can be treated as the solid solutions $(Dy_2O_3)(Co_2O_3)$. Samples heated at 800°C and 900°C, however, crystallize in the orthorhombic perovskite structure. We found that in the case of yttrium the cubic phase is occurs up to 700°C and a mixture of the cubic and orthorhombic phases above 700°C. We obtain only the cubic $Ln_2O_3+Co_2O_3$ solid

solution up to 900°C in the case of Er and Yb (Figure. 9). Cubic C-type structures of Dy, Y, Er and Yb cobalt oxide derivatives prepared at 700°C are shown in Fig.8(b).
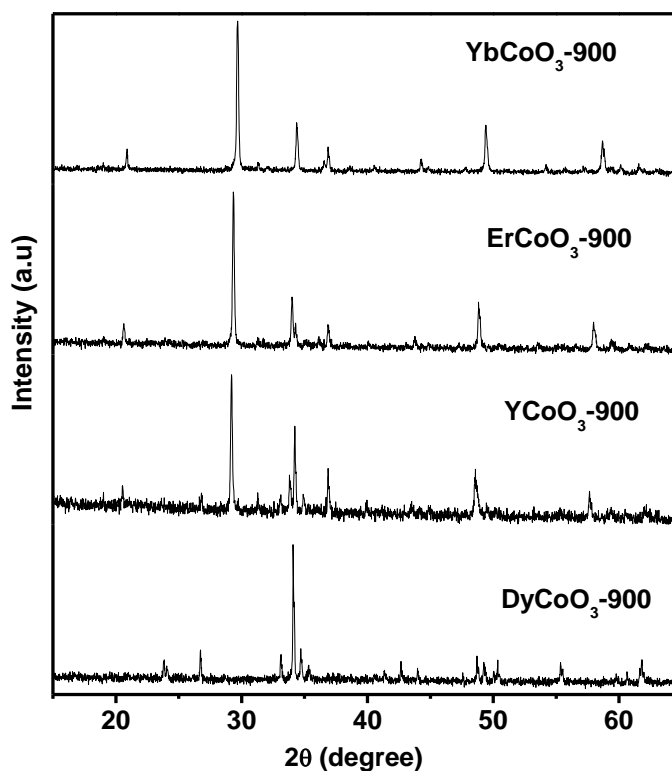
Figure 9. *XRD patterns of (Ln_2O_3)(Co_2O_3) (Ln: Dy, Y, Er and Yb) solid solutions heated at 900 °C*

All the cubic solid solutions of Co_2O_3 with Ln_2O_3 (Ln = Dy, Y, Er and Yb) show excellent catalytic activity with TOF values between 7.9×10^{-4} and 1.3×10^{-3} s^{-1} (Figure. 10(a)). The oxygen evolved per mole of Co per unit surface area is shown in Figure. 10(b). The cubic solid solution of Co_2O_3 with Y_2O_3 show somewhat lower catalytic activity of 19.5 mmoles/mole of Co.m^2 after 15 min, but all the other solid solutions show a high activity of around 38.9±2.7 mmoles/mole of Co.m^2 after 15 min.
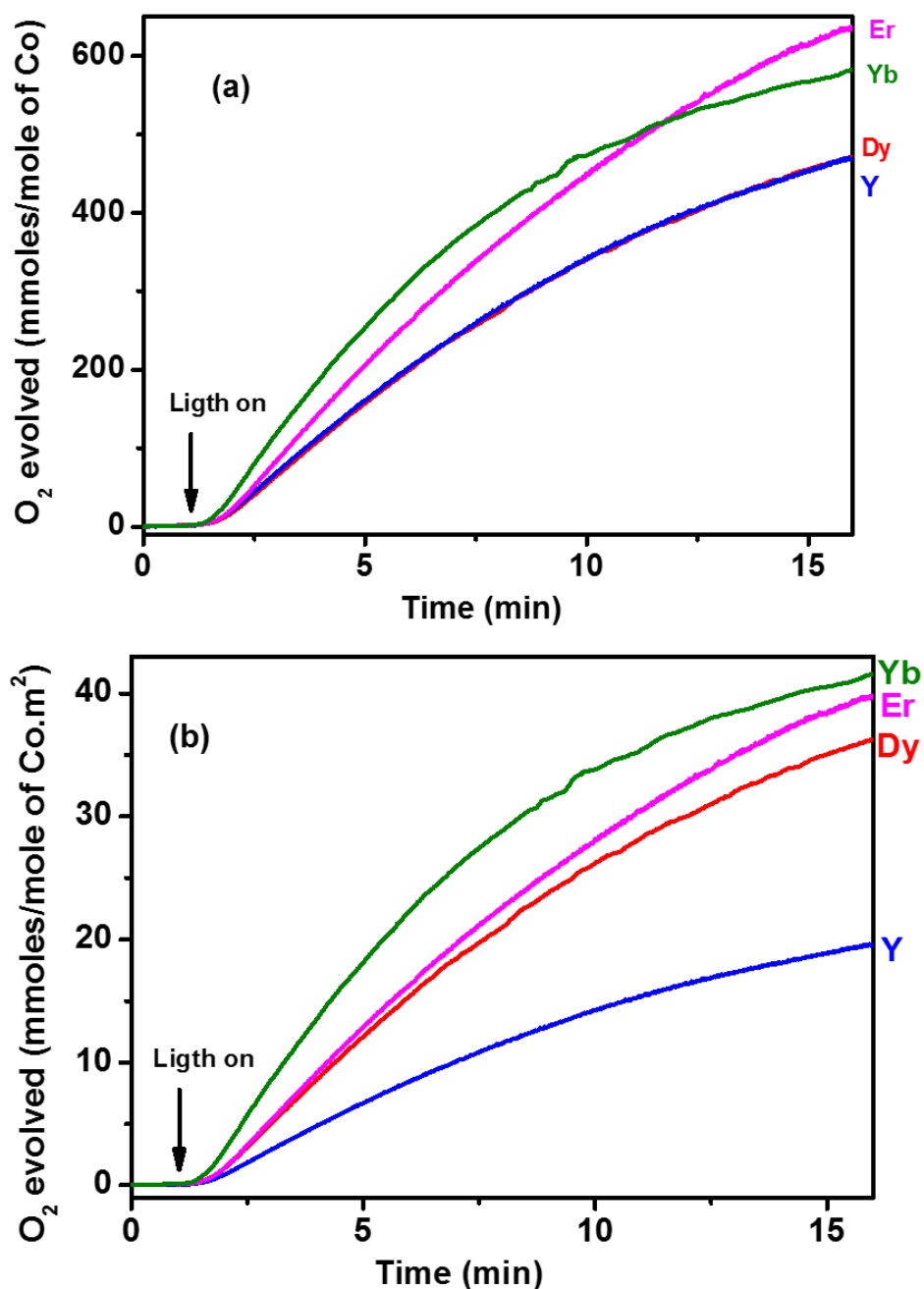
Figure 10. *O₂ evolved by (Ln₂O₃)(Co₂O₃) (Ln: Dy, Y, Er and Yb) prepared at 500 °C (a) per mole of Co, (b) per mole of Co per unit surface area*

Having found good catalytic activity in solid solutions of Co_2O_3 and Ln_2O_3, we examined the electronic configuration of Co in these oxides by carrying out magnetic susceptibility measurements of the solid solution of Y_2O_3 and Co_2O_3. The plot of inverse

magnetic susceptibility as function of temperature (Fig.11) gives a magnetic momentum 2.41 μB, indicating that cobalt in the intermediate-spin state, $t_{2g}^5 e_g^1$.
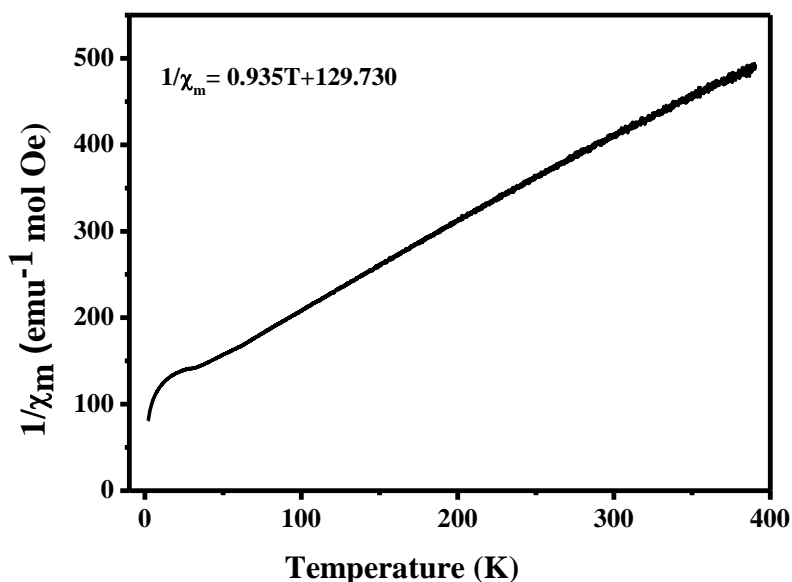
Figure 10. *Magnetic susceptibility plot of (Y$_2$O$_3$)(Co$_2$O$_3$)*

Interestingly, the yield of O$_2$ evolved by these solid solutions per mole of Co per unit surface area (38.9 ± 2.7 mmoles/mole of Co.m^2) is comparable to that of orthorhombic perovskite LnCoO$_3$ (34.6 ± 3.4 mmoles/mole of Co.m^2), the only commonality between the two being the electronic configuration of Co^{3+} ($t_{2g}^5 e_g^1$). We have compared the O$_2$ evolution activities (TOF values) of best reported manganese, cobalt based catalysts with our catalysts and shown in Table 2. The activities of some of our catalysts are comparable with best reported values.

Table 2. Comparison O_2 evolution activities (Turn of Frequencies, TOF) of our oxygen evolution catalysts with reported catalysts.

Catalyst	TOF/ s^{-1}	Reference No.
λ-MnO_2	3×10^{-5}	11
δ-MnO_2	1.56×10^{-5}	12
Mn_3O_4	1.6×10^{-4}	14
Mn_2O_3	5×10^{-4}	20
$MgMn_2O_4$	0.8×10^{-4}	20
$LaCoO_3$	1.4×10^{-3}	20
$Li_2Co_2O_4$	1.0×10^{-3}	17
$LaCoO_3$	1.4×10^{-3}	Present work
$LaMnO_3$	4.8×10^{-4}	Present work
$LaNiO_3$	1.2×10^{-4}	Present work
$LaFeO_3$	8.9×10^{-5}	Present work
$DyCoO_3$	2.8×10^{-4}	Present work
$YMnO_3$	5.2×10^{-5}	Present work
$YbMnO_3$	9.2×10^{-5}	Present work
$(Er_2O_3)(Co_2O_3)$	1.3×10^{-3}	Present work
$(Y_2O_3)(Co_2O_3)$	7.9×10^{-4}	Present work

Conclusions

Careful photocatalytic water oxidation studies have indicated that cobaltites show better activity than manganites while nickelites and ferrites show poor activity. Furthermore, orthorhombic manganites show much higher activity than the hexagonal manganites. In the case of cobaltites of heavy rare earths such as Dy, Er, Yb and Y, the oxides obtained from the citrate gel decomposition depends on the reaction temperature, those prepared around or below 700°C generally exist as cubic solid solutions of Ln_2O_3 and Co_2O_3 (space group Ia-3).

Orthorhombic rare earth manganites $LnMnO_3$ (Ln= La, Nd, Sm, Gd and Dy) with the perovskite structure exhibit fairly good photocatalytic properties for the oxidation of water unlike the hexagonal manganites, $YbMnO_3$ and $YMnO_3$. The presence of Mn^{3+} ions ($t_{2g}^3 e_g^1$) in the distorted octahedral environment in the orthorhombic manganites is clearly an important factor. In the rare earth cobaltites of perovskite structure $LaCoO_3$ (Rhombohedral, $R\overline{3}C$) shows the highest catalytic activity, while the other orthorhombic cobaltites $LnCoO_3$ (Ln= Pr, Nd, Sm, Gd and Dy) show comparable activity, although little lower than that of $LaCoO_3$. The heavier rare earths (Dy, Er, Yb and Y) do not form orthorhombic perovskites readily and remain in the form of cubic solid solutions of Co^{3+} in Ln_2O_3 when prepared around 700°C or lower. These solid solutions with the cubic C-type rare earth oxide structure containing Co^{3+} present in the intermediate-spin configuration ($t_{2g}^5 e_g^1$) just as in $LaCoO_3$, interestingly exhibit catalytic activity for the oxidation of water comparable to $LaCoO_3$.

References

1. N. Armaroli, V. Balzani, **Angew. Chem. Int. Ed.**, 46, 2007, 52.

2. N.S. Lewis, D. G. Nocera, **Proc. Natl. Acad. Sci. USA**, 2006,103, 15729.

3. W. Ru¨ttinger, G. C. Dismukes, **Chem. Rev.**, 1997, 97, 1.

4. N. D. Morris, M. Suzuki, and T. E. Mallouk, **J. Phys. Chem. A.,** 2004**,** 108 9115.

5. F.A. Frame, T.K. Townsend, R.L. Chamousis, E.M. Sabio, Th. Dittrich, N.D. Browning, F.E. Osterloh, **J. Am. Chem. Soc.,** 2011, 133 , 7264.

6. E. Tsuji, A. Imanishi, K. Fukui, Y. Nakato, **Electrochim. Acta.,** 2011, 56, 2009.

7. Y. Lee, J. Suntivich, K.J. May, E.E. Perry, Y. Shao-Horn, **J. Phys. Chem. Lett.**, 2012, 3, 399.

8. A. Harriman, I.J. Pickering, J.M. Thomas, P.A. Christensen, **J. Chem. Soc., Faraday Trans., 1988,** 1, 84, 2795.

9. M.M. Najafpour, T. Ehrenberg, M. Wiechen, P. Kurz, **Angew. Chem. Int. Ed.,** 2010, 49, 2233.

10. A. Iyer, J. Del-Pilar, C.K. King'ondu, E. Kissel, H.F. Garces, H. Huang, A.M. El-Sawy, P.K. Dutta, S.L. Suib, **J. Phys. Chem. C.,** 2012, 116, 6474.

11. D.M. Robinson, Y.B. Go, M. Greenblatt, G.C. Dismukes, **J. Am. Chem. Soc.,** 2010, 132, 11467.

12. V.B.R. Boppana, S. Yusuf, G.S. Hutchings, F. Jiao, **Adv. Funct. Mater.**, 2013, 23, 878.

13. V.B.R. Boppana, F. Jiao, **Chem. Commun.**, 2011, 47, 8973.

14. D.M. Robinson, Y.B. Go, M. Mui, G. Gardner, Z. Zhang, D. Mastrogiovanni, E. Garfunkel, J. Li, M. Greenblatt, G. C. Dismukes, **J. Am. Chem. Soc.**, 2013, 135, 3494.

15. D. Shevchenko, M.F. Anderlund, A. Thapper, S. Styring, **Energy Environ. Sci.**, 2010, 4, 1284.

16. F. Jiao, H. Frei, **Angew. Chem. Int. Ed.**, 2009, 48, 1841

17. G.P. Gardner, Y.B. Go, D.M. Robinson, P.F. Smith, J. Hadermann, A. Abakumov, M. Greenblatt, G.C. Dismukes, **Angew. Chem. Int. Ed.,** 2012**,** 51, 1616

18. M.W. Kanan, Y. Surendranath, D.G. Nocera, **Chem. Soc. Rev.**, 2009, 38, 109

19. Y. Yamada, K. Yano, D. Hong, S. Fukuzumi, **Phys. Chem. Chem. Phys.**, 2012, 14, 5753.

20. U. Maitra, B.S. Naidu, A. Govindaraj, C.N.R. Rao, **Proc. Natl. Acad. Sci. USA**, 2013, 110, 11704.

21. J. Suntivich, K.J. May, H.A. Gasteiger, J.B. Goodenough, Y. Shao-Horn, **Science**, 2011, 334, 1383.

22. J.-S. Zhou, J.B. Goodenough, J.M. Gallardo-Amores, E. Morán, M.A. Alario Franco, R. Caudillo, **Phys. Rev. B.,** 2006, 74, 014422.

23. A. Filippetti, N.A. Hill, **J. Magn. Magn. Mater.,** 2006, 236, 176.

24. T. A. Betley, Y. Surendranath, M.V. Childress, G.E. Alliger, R. Fu, C.C. Cummins, D.G. Nocera, **Phil. Trans. R. Soc. B**., 2008, 363, 1293.

25. L.B. Farhat, M. Amami, E.K. Hlil, R.B. Hassen, **J. Alloy. Compd**., 2009, 479 594.

Chapter 3

Water splitting based on few-layer TaS$_2$ and TiS$_2$

*Summary**

Graphene analogues of TaS$_2$ and TiS$_2$ (3-4 layers), prepared by Li-intercalation followed by exfoliation in water, have been characterized. Nanocomposites of CdS with few-layer TiS$_2$ and TaS$_2$ have been employed for visible-light-induced H$_2$ evolution reaction (HER). Benzyl alcohol was used as the sacrificial electron donor, which gets oxidized to benzaldehyde during the reaction. Few-layer TiS$_2$ is a semiconductor with a band gap of 0.7 eV and its nanocomposites with CdS shows an activity of 1000 μmol h^{-1} g^{-1}. The nanocomposite of few-layer TaS$_2$, on the other hand, gives rise to higher activity of 2320 μmol h^{-1}g^{-1}. The higher activity is attributed to the metallic nature of the few-layer TaS$_2$. The amount of hydrogen evolved after 20 hours was 14833 μmol and 28132 μmol after 16 hours with turnover frequencies of 0.24 h^{-1} and 0.57 h^{-1} respectively for CdS/TiS$_2$ and CdS/TaS$_2$ nanocomposites respectively.
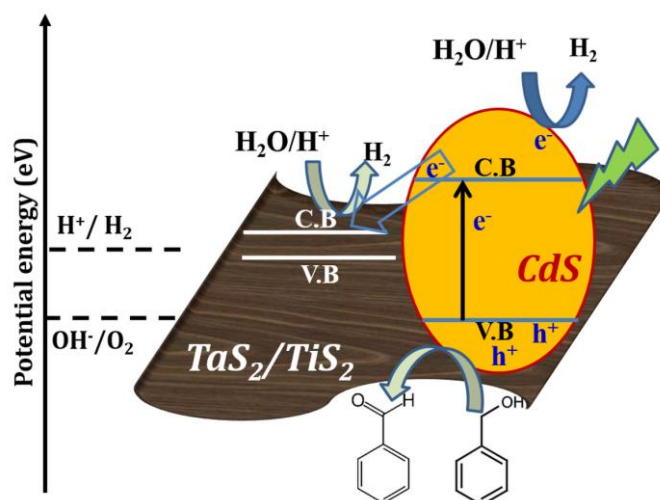
Introduction

Artificial photosynthesis has emerged as a potential means of splitting water for the generation of H_2. Of the various strategies employed for this purpose, dye sensitization and use of semiconducting nanostructures or their heterostructures are some of the most explored ones. TiO_2 was first used photocatalyst for H_2 generation from water.[1] Since then numerous photocatalysts, especially oxides, have been used for the generation of H_2 from water, either photocatalytically or photoelectrochemically [2-3]. Though oxide photocatalysts are highly stable with respect to sulfides and nitrides, and do not undergo oxidation or reduction during the processes of water splitting, they have an intrinsic limitation of having a highly positive valence band (O 2p). It is, therefore, difficult to find oxide semiconductors with a sufficiently negative conduction band to reduce H_2O to H_2, at the same time having a sufficiently small band gap to absorb visible light. [4-5] Metal sulfides and selenides, on the other hand, generally possess a less positive valence band and are visible-light-active. Sulfides and selenides of Cd possess a sufficiently negative conduction band to reduce protons to H_2 and can be used for the photocatalytic hydrogen evolution reaction (HER).[6-11]

A n-type semiconductor CdS, with a band gap of 2.4 eV is suitable for HER due to the fact that it shows high activity in almost the entire visible range (up to 600 nm) [12] and has a negative flat band potential. [13] CdS alone is, however, less active in photocatalytic H_2 production due to high charge recombination and degradation of the catalyst during the reaction. [14] In the presence of co-catalysts such as Pt and Pd, it shows good photocatalytic activity [15-16] and the challenge that we face today is to develop cost-effective catalysts and co-catalysts comprising non-noble metals. Numerous efforts have been made to replace noble metals with low-cost co-catalysts. Cost-effective substitutes for the co-catalyst

would require materials which are metallic or highly conducting like graphene [17-23] to allow easy transfer of electrons to water thus enhancing water splitting. Most of the transition metal dichalcognides are direct or indirect band gap semiconductors. TiS_2 is semimetallic like graphene and TaS_2 is metallic.

Scope of the present investigations

Group 4 (TiS_2) and Group 5(TaS_2) transition metal dichalcogenides are semi-metallic and metallic respectively in their bulk form (see Appendix in the end of Chapter 3). Making them few-layer species would introduce effects due to their quantum confinement These metallic dichalcogenides have high in-plane conductivities and can be used for separation of photogenerated charge carriers. TiS_2 being semiconducting in few-layer structure demonstrates the role of the cocatalyst in charge separation of photogenerated charge carriers and how this property affects the HER. Metallic few-layer TaS_2 on the other hand acts as an electron conductor from CdS to water. Both transition metal dichalcogenides have their conduction band minimum above water reduction value. This would make them a material of interest for HER.

Experimental Section

Synthesis

TiS_2 was prepared by using sealed tube method. In a typical experiment Ti metal powder was ground with sulfur powder and the homogeneous powder was filled in a quartz tube and heated in box furnace at 800 °C for 72 hours. TaS_2 sample used for all the experiments was procured commercially (Alfa Aesar 99.8% metal basis). Few-layer TaS_2 and TiS_2 were prepared as follows. Firstly, Li was intercalated by soaking 1g of the metal

disulfide in 3.5 mL (1.6 M in hexane) of n-butyl lithium in 12 mL of hexane in a nitrogen atmosphere for 72 h at 300K. The intercalated samples were washed with hexane several times to remove unreacted n-butyl lithium. The intercalated samples were exfoliated by ultrasonication in distilled water in a closed vial for four hours. The suspension was centrifuged and the solid product collected. Nanocomposites of few-layer TiS_2 and TaS_2 with CdS nanoparticles were prepared as follows. CdS nanoparticles were prepared by adding 0.1mM (10 mL) of sodium sulfide into 0.1mM (10 mL) of cadmium acetate under stirring; the precipitate formed was centrifuged and dried at 60 ºC. 10 mg of TiS_2 or TaS_2 was dispersed in water (10mL) by sonication for one hour. 0.1 mM of $Cd(CH_3COO)_2$ ($CdS/MS_2 = 1.4:1.0$ (M=Ta,Ti)) was added to the above dispersion and the mixture was stirred for eight hours, followed by addition of 0.1 mM of Na_2S in 10 ml water. Yellow CdS particles were obtained as the final product was centrifuged and dried in air at 60 ºC for 12 hours. To prepare nanocomposites with different mass ratios of the CdS/TaS_2 (0.7:1.0, 1.4:1.0 and 2.1:1.0 of CdS/TaS_2) required amounts of $Cd(CH_3COO)_2$ were added to 10 mg of TaS_2 in 10 mL of water.

Characterization

All samples were characterized by using a powder X-ray diffractometer (Bruker D8 Advance, Cu Kα source, (λ=0.1541 nm). Transmission electron microscope (TEM) images were obtained by using a JEOL TEM 3010 instrument fitted with a Gatan CCD camera operating at an accelerating voltage of 300 kV. Atomic force microscopic (AFM) measurements were performed by using an Innova atomic force microscope. Electronic absorption spectra were recorded with a PerkinElmer Lambda 650 UV/Vis spectrometer. Raman spectra of samples were recorded by using a 632 nm He–Ne laser with a Jobin Yvon LabRam HR spectrometer. Surface area measurements of the few-layer samples

were done by using a Quantachrome Autosorb instrument at 77 K. Conductivity measurements were done by using 6 mm gap gold electrodes on SiO_2/Si substrates.

Photocatalytic measurements

Photocatalytic activies of the CdS/TaS_2 (TiS_2) nanocomposites was evaluated by the generation of hydrogen in the presence of benzyl alcohol in acetic acid as sacrificial agents under visible light irradiation. In a typical photocatalytic study, 2.5 mg of the photocatalyst was dispersed in a 50ml of water. 2ml of benzyl alcohol was dissolved in 5ml of acetic acid. It was then added to dispersion, of catalyst and water, in a cylindrical quartz cell with flat surfaces being exposed to light. The solution was purged with N_2 for 30 min prior to activity tests to remove all dissolved gases and to maintain inert atmosphere. The solution was exposed to light using 450 W Xe arc lamp (working at 400W) (New Port, 6280) fitted with water filter and 399 nm cut-off filter. The H_2 evolved was quantified using gas chromatography (Perkin Elmer, Clarus 580 GC) equipped with TCD detector by manually injecting 1 ml of evolved gases from headspace of the quartz vessel after every 1hr. Similar experiment was performed using 0.1M Na_2S and 0.1M Na_2SO_3 as sacrificial reagent.

Turn over frequency (TOF) and turn over number (TON) was calculated as follows:

$$TOF\ (h^{-1}) = \frac{\text{Moles of } H_2 \text{ evolved per hour}}{\text{Moles of Active Catalyst}} \qquad (Equation\ 1)$$

$$TON = \frac{\text{Moles of } H_2 \text{ released (after certain time)}}{\text{Moles of Active Catalyst}} \qquad (Equation\ 2)$$

Results and Discussion

The system follows a typical semiconductor type mechanism where incident light excites an electron to conduction band of the semiconductor which then transfers the electron to the co-catalyst (generally Pt and, TaS_2 and TiS_2 in our study). Then electron on the surface of the co-catalyst would then be transferred to water for HER.
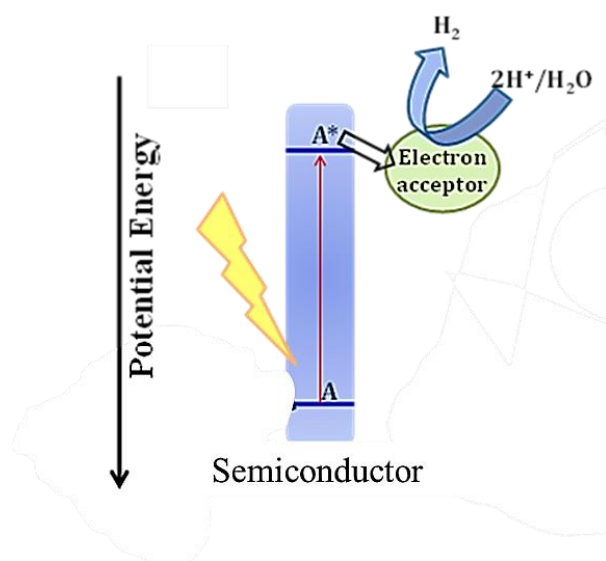
Scheme 1 *The processes used for photosynthetic reduction of water with aid of cocatalyst.*

The compound were synthesized and characterized and their photocatalytic activity were studied.
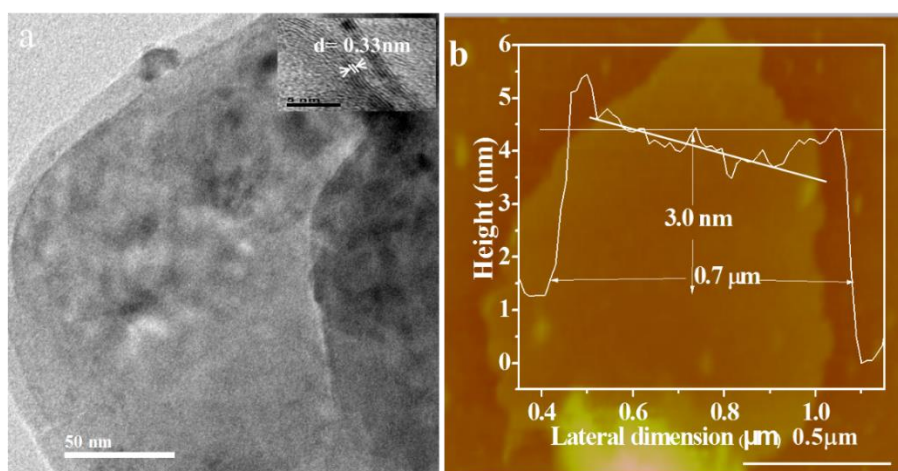
Figure 1. *(a) TEM image (b) AFM image of the exfoliated TiS2.*

In Figure 1a, we show a TEM image of the few-layer TiS_2 obtained after exfoliation of the Li intercalated material. Figure 1b shows the AFM image and the corresponding height profile of few-layer TiS_2. The height profile gives a layer thickness of 3.0 nm corresponding to 4 layers, with a lateral dimension of 1.5 μm. The phase purity of the as-synthesized and exfoliated TiS_2 samples was confirmed by x-ray diffraction (XRD).
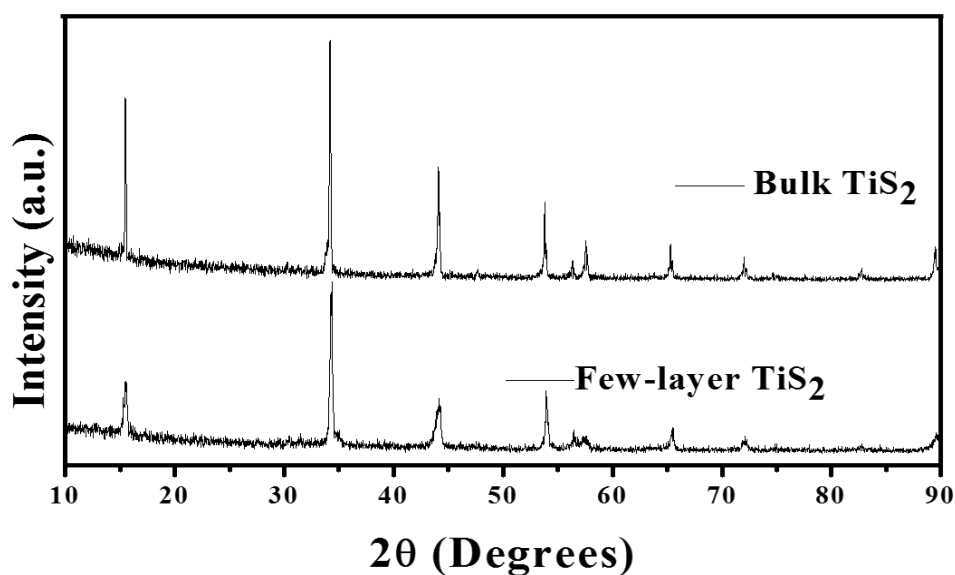
Figure 2. *Comparison of the X-ray Diffraction bulk TiS_2 with few-layer TiS_2*

In the XRD pattern of exfoliated TiS_2, the intensity of the reflection corresponding to stacking direction (001) was considerably lower and line-widths were larger. (Figure 2).

The A_{1g} band in Raman spectrum, corresponds to the out of plane mode in metal dichalcogenides is observed at 330 cm^{-1} of few-layer TiS_2 (Figure 3.) shows a red shift of 4 cm^{-1} of the A_{1g} mode compared to the bulk sample.
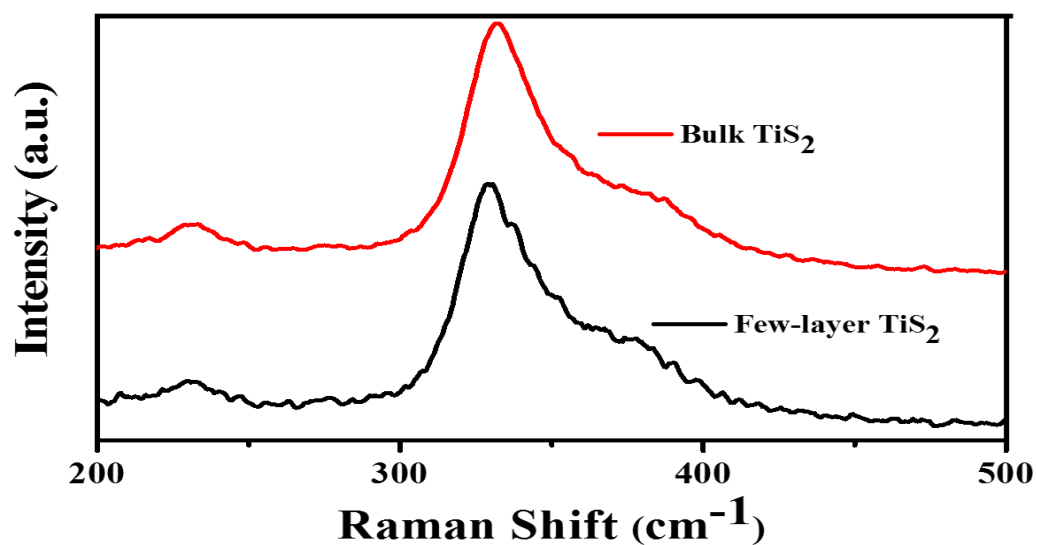
Figure 3. *Comparison of the A_{1g} band in Raman spectra of bulk TiS_2 with few-layer TiS_2*

As the number of layers decreases, the restoring forces decrease causing a softening and broadening of the in plane A_{1g} mode [24].

TEM image of exfoliated TaS_2 is shown in Figure 4a and the AFM image in Figure 4b. The AFM height profile of the few-layer TaS_2 has a layer thickness of 2.6 nm corresponding to 3 layers, with a lateral dimension of 2.5 μm.
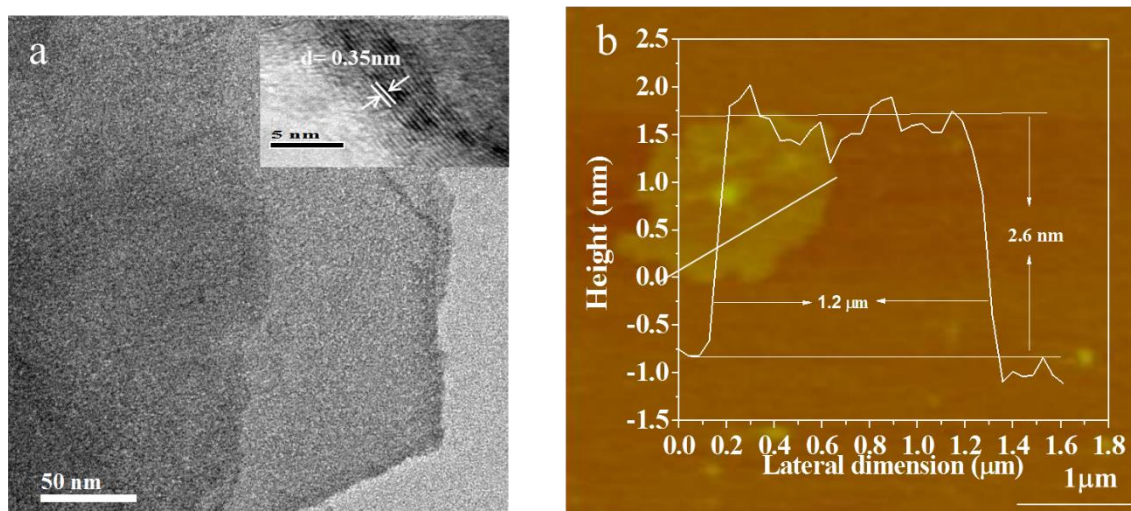
Figure 4. *(a) TEM image (b) AFM image of the exfoliated TaS_2.*
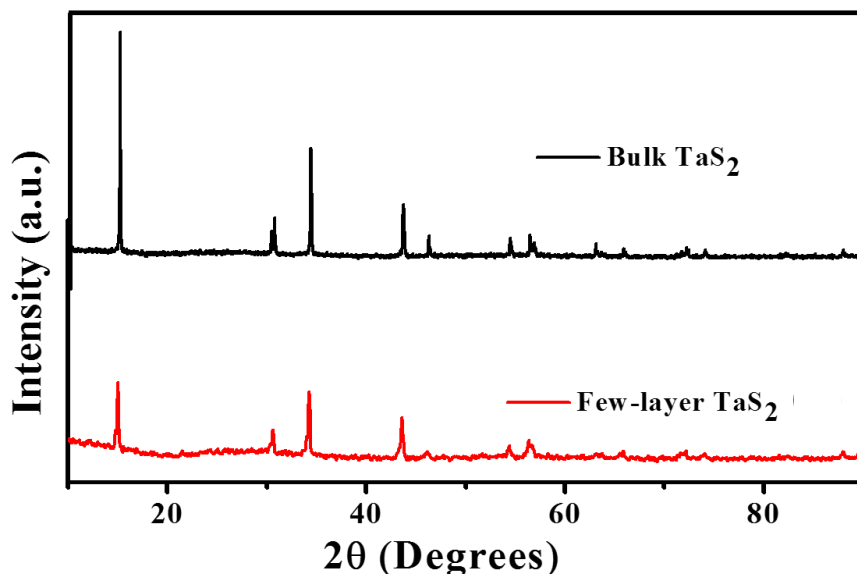
Figure 5. *Comparison of the X-ray Diffarction bulk TaS₂ with few-layer TaS₂*

The XRD of bulk TiS_2 was compared with few-layer TaS_2 and we observed broadening of peaks in case of few-layer TaS_2 shown in Figure 5.

N_2 adsorption isotherms recorded at 77K (Figure 6) give surface areas of 48.2 m²/g (Figure 6.a) and 20.8 m²/g (Figure 6.b) respectively for few-layer TiS_2 and TaS_2. TaS_2 shows type II adsorption isotherm signifying unrestricted monolayer-multilayer adsorption.
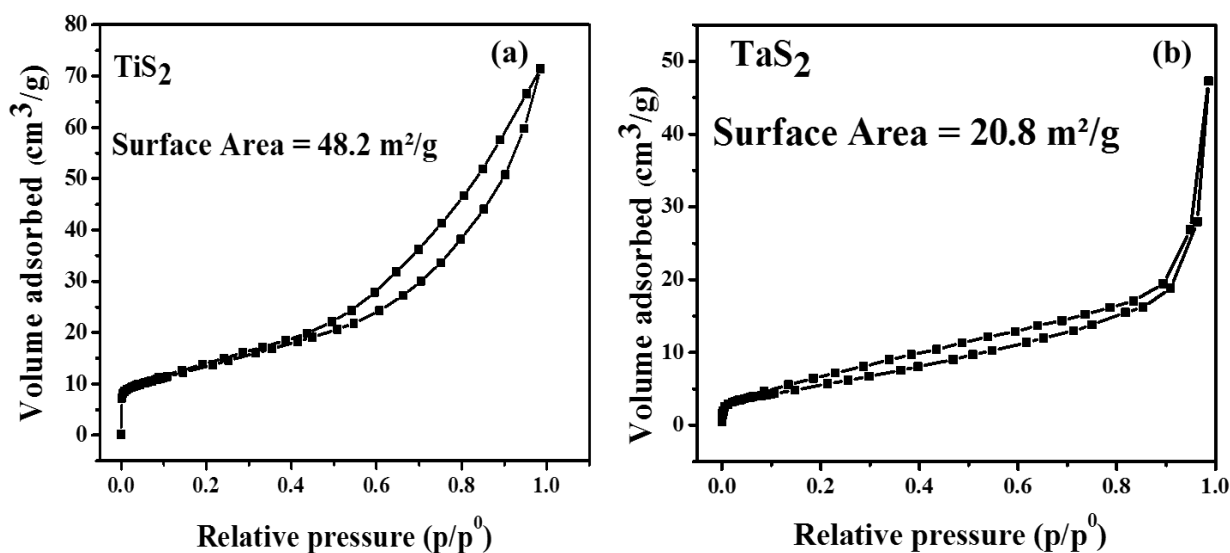
Figure 6. *N₂ adsorption isotherm of (a) few-layer TiS₂ and (b) of few-layer TaS₂*

Beyond relative pressure (p/p°) of 0.025 (the beginning of the almost linear middle section of the isotherm), we see evidence of completion of monolayer coverage and initiation of multilayer adsorption. TiS_2 on the other hand shows type IV adsorption isotherm, with a hysteresis loop near 0.45 relative pressure, associated with capillary condensation taking place in the mesopores, and the limiting uptake over a range of high p/p°. The initial part of the isotherm shows Type II behaviour [25].
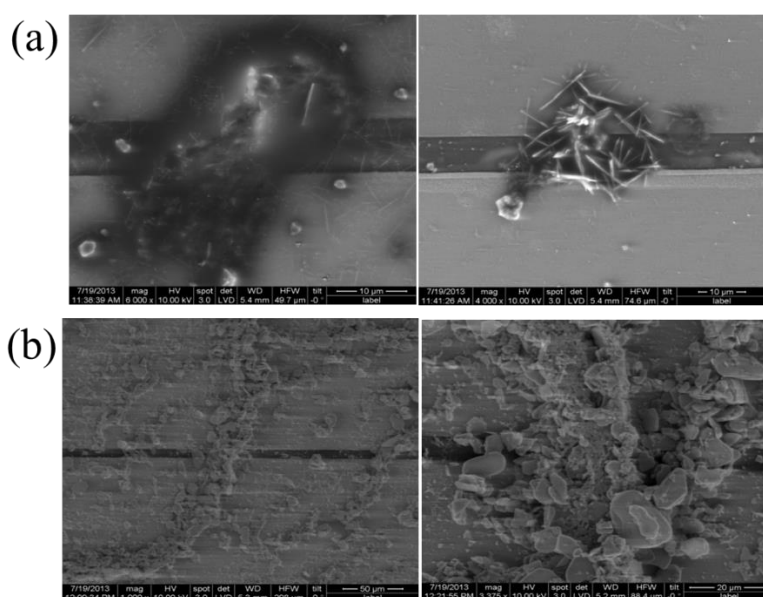
Figure 7. *Fesem image of the few-layer (a) TiS_2 and (b) TiS_2 at the gap electrodes*

Conductivity measurements of bulk and few-layer samples of TiS_2 and TaS_2 were carried out on 6 μm gap gold electrodes on SiO_2/Si substrates (see Figures 7a and 7b).
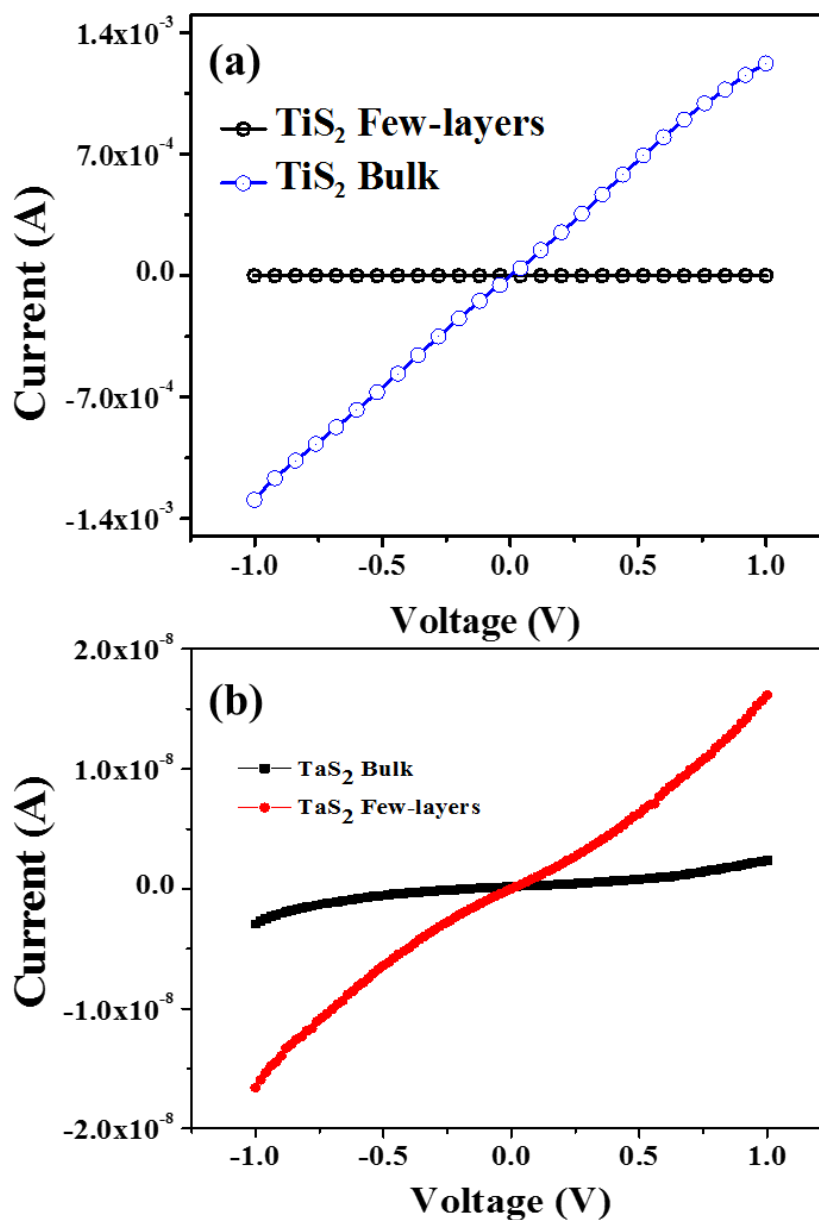
Figure 8. *Comparison of Current (I) vs Voltage (V) of (a) few-layer TiS₂ with bulk and (b) few-layer TiS₂ with few layer TaS₂*

Figure 8a shows the current (I) vs voltage (V) plots of few-layer TiS_2 in comparison with that of bulk TiS_2, and Figure 8b shows the current vs voltage plots of few-layer TaS_2 in comparison with that of bulk. While the current vs. voltage plot changes from linear to

non-ohmic behavior on reduction of the bulk to few-layers in the case of TiS_2 [26], few-layer TaS_2 remains Ohmic even in the few-layer samples. [27-28].
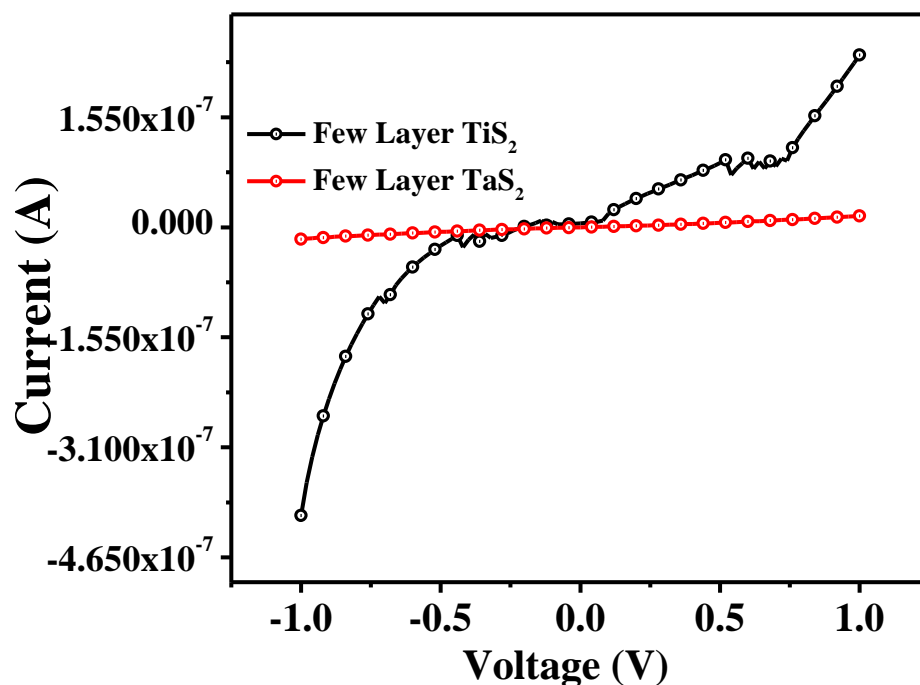
Figure 9. *Comparison of Current (A) vs Voltage (V) of few-layer TiS₂ with few-layer TaS₂*

Comparison between few-layer TiS_2 and few layer TaS_2 is shown in Figure 9. Theoretical calculations do suggest bulk TiS_2 is to be semi-metallic while the few-layer material is semiconducting. The surface layer has an electronic structure similar to that of a semiconductor with a small energy gap of 0.7 eV. The semiconducting nature decreases (metallicity increases) as number of layers increases from few-layers to that of bulk. The exfoliated sample was employed in photocatalytic applications. Both few layer TiS_2 and TaS_2 are not active as hydrogen evolution reaction catalyst, we can use them as co-catalyst for their energy levels lies near the photoreaction values of H_2O. We have synthesized composite of both few layer TiS_2 and TaS_2 with CdS.
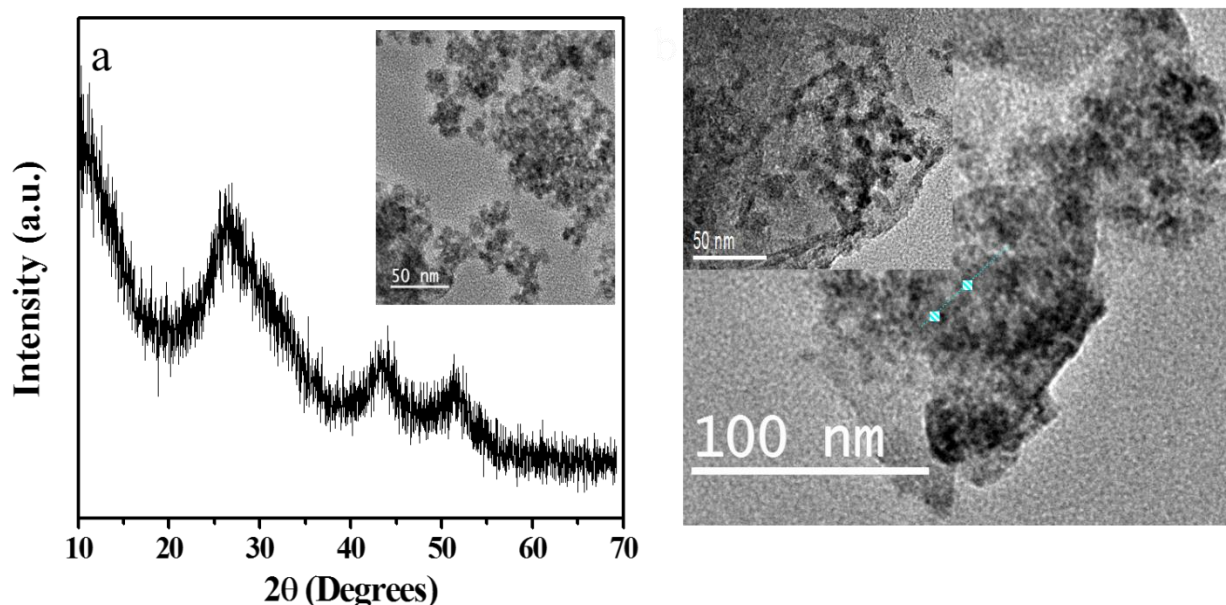
Figure 10. *(a) XRD pattern of CdS nanoparticles. Inset in (a) shows a TEM image of CdS nanoparticles (b) TEM image of the nanocomposite of CdS with TiS_2 ($CdS:TiS_2=1.4:1.0$). Inset in (b) shows a TEM image of the nanocomposite of CdS with TaS_2 ($CdS:TaS_2=1.4:1.0$).*

Figure. 10a gives the XRD pattern of as-prepared CdS. Broad reflections in the x-ray pattern confirm the presence of small particles. The TEM image of the CdS nanoparticles, shown in the inset of Figure 10a reveals the presence of 5-12 nm nanoparticles. TEM images of the composites of CdS/TiS_2 and CdS/TaS_2 in Figure 10b show the dispersion of CdS nanoparticles on the two-dimensional sheets.

We have carried out H_2 evolution studies using few-layer TaS_2 and TiS_2 as co-catalysts for CdS, by using the nanocomposites of TaS_2 and TiS_2 with CdS nanoparticles. CdS nanoparticles alone show an activity of 336 $\mu mol\ h^{-1}g^{-1}$ (see inset of Figure 11) with TOF and TON of 0.049 h^{-1} and 0.417 respectively after 8 hours. The amount of H_2 evolved after 8 hours for 2.5mg catalyst was 7.2 μmol. The role of benzyl alcohol as a sacrificial agent in enhancing photocatalytic H_2 evolution has been described by Rao et al. [29] Benzyl

alcohol gets converted to benzaldehyde, while acting as hole scavenger and thereby minimizing electron-hole recombination.
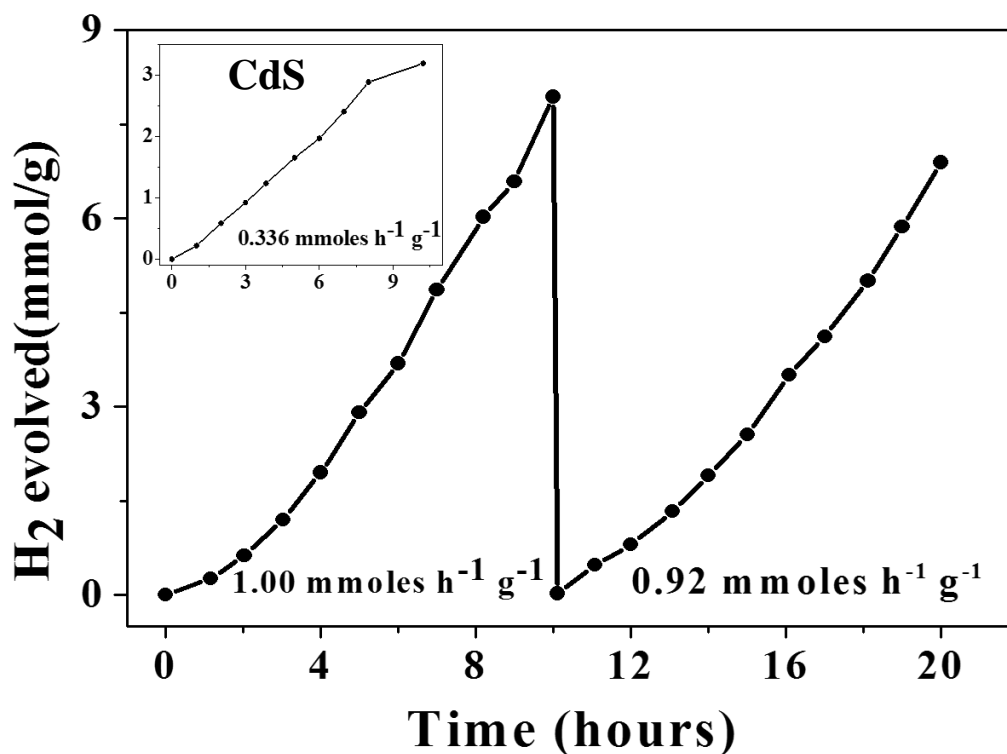
Figure 11. *H_2 evolution activity of (a) the CdS-TiS$_2$ (1.4:1.0) nanocomposite. Inset shows the H_2 evolution activity of CdS nanoparticles.*

CdS does not show any activity in acetic acid, but the acid inhibits photocorrosion of CdS [15]. Being a low band gap semiconductor, TiS$_2$ alone does not show any activity for H_2 evolution. However, on coupling with CdS, it increases the activity of CdS from 336 μmol h^{-1}g^{-1} to 1000 μmol h^{-1}g^{-1} as shown in Figure 11. The TOF increases from 0.049 h^{-1} to 0.244 h^{-1}, a five-fold increase while the TON (after 8 hours) was 1.472 for CdS/TiS$_2$. The total amount of H_2 evolved after 20 hours by 2.5 mg of the composite is 37.2 μmol clearly, few-layer TiS$_2$ aids electron transport from CdS to water. Since the conduction band (CB) of CdS is above the conduction band of TiS$_2$, the interface between the two allows electron transfer from the CB of CdS to that of TiS$_2$, thereby allowing electron-hole separation. Furthermore, the CB level of TiS$_2$ is slightly more negative than the water

reduction potential and aids H_2 evolution. Activity of the composite with benzyl alcohol as sacrificial agent was much higher than in 0.1M Na_2S and 0.1M Na_2SO_3. Increasing the concentration of benzyl alcohol did not affect the activity much. The electron transfer probability becomes considerably higher by the use of metallic TaS_2 in place of semiconducting TiS_2.
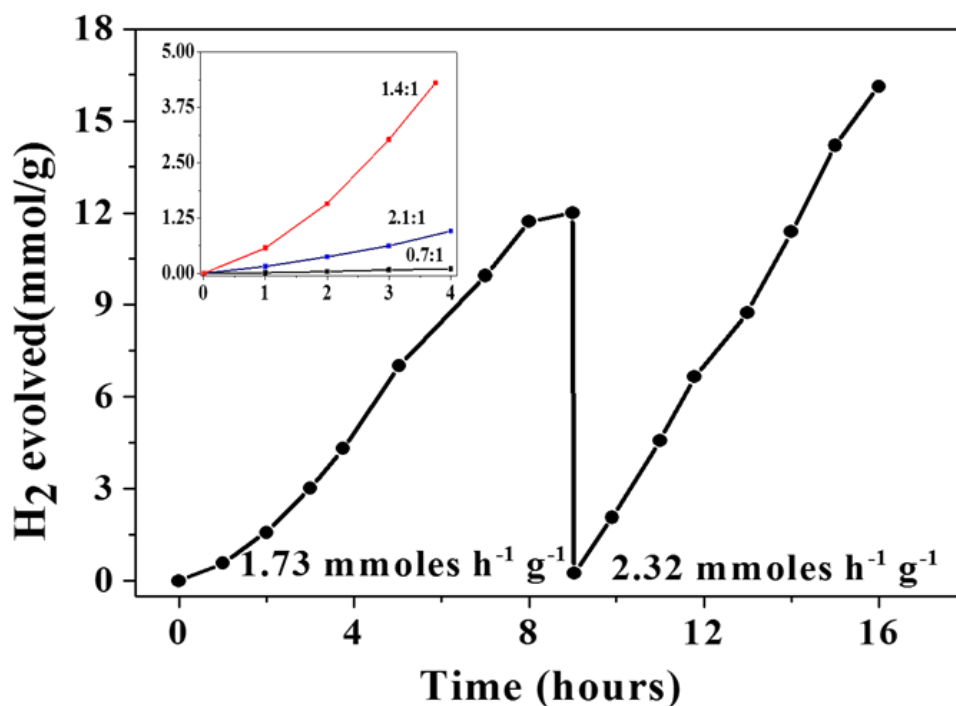
Figure 12. *H_2 evolution activity of CdS-TaS$_2$ (1.4:1.0) nanocomposite. Inset shows the activity of H_2 evolution and TOF values for CdS and TaS$_2$ composites with different CdS:TaS$_2$ ratios*.

The hydrogen evolution activity of the CdS/TaS$_2$ nanocomposite is shown in Figure 12. While TaS$_2$ alone does not show any activity, CdS/TaS$_2$ has as an activity of 1732 μmol h^{-1} g^{-1}, with a TOF of 0.432 h^{-1} and TON of 2.864. Note that the activity has increased almost 8 fold after 8 hours. Interestingly, the activity of the composite increases with further cycling to 2320 μmol h^{-1}g^{-1} with a nearly 11 fold increase in the activity as

compared to CdS a TOF as 0.566 h^{-1} and TON of 3.959 after 8 hours. This could possibly arise due to further oxidation of benzaldehyde. The total amount of H_2 evolved after 16 hours for 2.5mg was 70.5 µmol. We studied HER activity at dilute concentrations (2.5 mg/ 50 ml of water) to enhance the total absorption of light by the catalyst. TaS_2 favours electron-hole separation by taking away the electron generated on the surface of CdS nanoparticles just as nanoparticles of Pt, Pd, Rh and such metals. From the electronic structure of TaS_2, we see that the e_g orbitals in the 5d conduction band lies close to the Fermi level [13], making it suitable for the hydrogen evolution reaction. Conductivity measurements reveal the metallic nature of few-layer TaS_2 while few-layer TiS_2 is semiconducting showing thereby why TaS_2 acts as a better cocatalyst for CdS than few-layer TiS_2. The determining factor is the ease of transfer of photogenerated electrons from CdS to the cocatalyst.
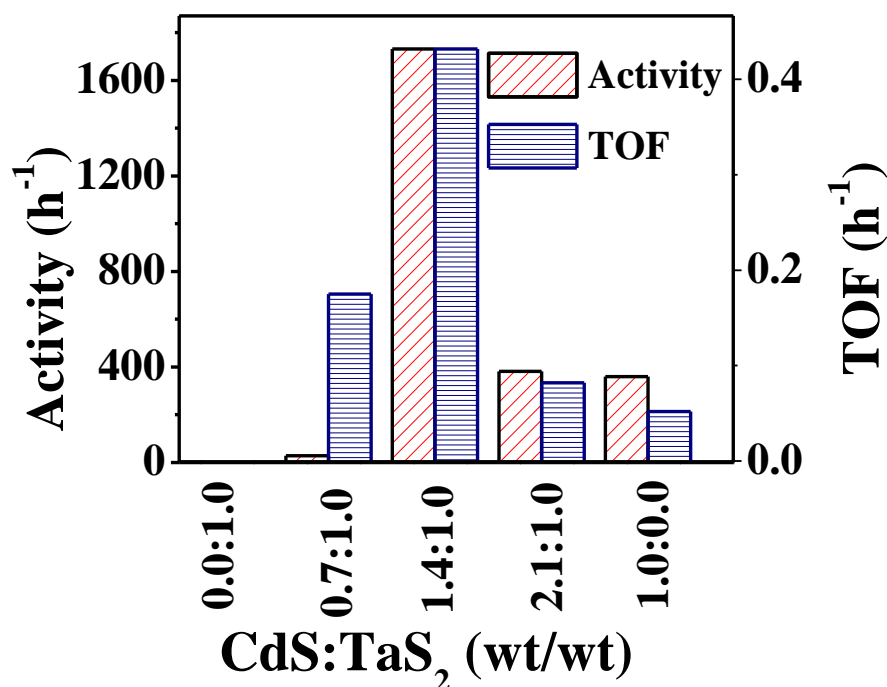
Figure 13. *Histogram of activity of H_2 evolution and TOF values for CdS and TaS_2 composites with different $CdS:TaS_2$ ratios.*

We have studied the effect of changing the ratio of CdS to TaS_2 in the nanocomposite (see inset of Figure 12 and Figure 13). While TaS_2 alone does not show any activity, H_2 evolution increases with increasing ratio of CdS reaching a maximum around a $CdS:TaS_2$ of 1.4:1.0. For CdS: TaS_2 of 0.7:1.0 TOF is only 0.175 h-1 but is twice that of CdS: TaS_2 = 2.1:1.0 (0.082 h-1). This observation demonstrates the role of TaS_2 in enhancing the activity of CdS. In Table 1, we compare the results reported in the literature on CdS-based catalysts with the results of the present study.

Table 1. *Comparitive result of photocatalytic HER of the composite with similar catalyst in the literature*

Composite	Sacrificial Agent	Activity (μmole h^{-1}g^{-1})	TOF (h^{-1})
CdS[a]	2ml Benzyl alcohol	336	0.049
CdS/TiS$_2$[a]	2ml Benzyl alcohol	1000	0.24
CdS/TaS$_2$[a]	2ml Benzyl alcohol	2320	0.57
CdS/Pt[31,b]	0.35M Na$_2$SO$_3$ and 0.25M Na$_2$S	726	0.116
CdS/Pt [33,b]	0.1 M Na$_2$S and 0.1 M Na$_2$SO$_3$	396	0.057
CdS/N-Graphene [32,b]	0.1M Na$_2$S and 0.1M Na$_2$SO$_3$	1050	0.155
CdS/NiS[31,b]	0.35M Na$_2$SO$_3$ and 0.25M Na$_2$S	1131	0.172
CdS/MoS$_2$[34,b]	10% (v/v) Lactic acid	5400	0.784

[a]400W Xe Lamp(λ>399nm) [b] 300W Xe Lamp(λ>420nm)

The activity of CdS/Pt in UV light is generally higher than with visible light as in the present study, and the visible light activity of CdS/Pt composite is generally small in most cases.[31-32] We see the present results on CdS/TaS_2 and CdS/TiS_2 compare

favorably in HER activity with other materials reported in the literature including CdS/NiS and CdS/N-graphene.[33]

Conclusions

The present study clearly reveals that few-layer TiS_2 having band gap of 0.7 eV and few-layer TaS_2 which is metallic can both be employed as co-catalysts for CdS for HER, favoring H_2 evolution in visible range. That TaS_2 is superior to TiS_2 in performance is related to metallic nature. This also supports why metallic cocatalyst like Pt, Pd are better than the semiconducting cocatalyst.

References

1. A. Fujishima and K. Honda, **Nature**, 1972, 238, 37

2. R. Abe, **J. of Photochem. Photobiol. C: Photochem. Rev.,** 2010, 11, 179

3. A. Kudo and Y. Miseki, **Chem**. **Soc. Rev.,** 2009,**38**, 253

4. J. G. Yu, L. F. Qi, M. Jaroniec, **J. Phys. Chem. C**, 2010,114, 13118

5. X. Chen, S. S. Mao, **Chem. Rev.,** 2007, 107, 2891

6. A. L. Linsebigler, G. Lu, J. T. Yates, **Chem. Rev.,** 1995, 95, 735

7. J. G. Yu, J. Zhang, S. W. Liu, **J. Phys. Chem. C,** 2010, 114, 13642

8. J. G. Yu, J. Zhang, **Dalton Trans.,** 2010, 39, 5860

9. J. Zhang, J. G. Yu, M. Jaroniec, J. R. Gong, **Nano Lett.,** 2012, 12, 4584

10. J. G. Yu, B. Yang, B. Cheng, **Nanoscale,** 2012, 4, 2670

11. Q. J. Xiang, J. G. Yu, M. Jaroniec, **J. Am. Chem. Soc.**, 2012, 134, 6575

12. S. Shen, L. Guo, X. Chen, F. Ren, S. S. Mao, **Int. J. Hydrogen Energy,** 2010, 35, 7110

13. M. Matsumura, S. Furukawa, Y. Saho, H. Tsubomura, **J. Phys.Chem.,** 1985, 89, 1327

14. D. J. Ferm_n, E. A. Ponomarev, L. M. Peter, **J. Electroanal. Chem.,** 1999, 473, 192

15. X. Zong, H. Yan, G. Wu, G. Ma, F. Wen, L. Wang, C. Li, **J. Am. Chem. Soc.,** 2008, 130, 7176

16. H. Yan, J. Yang, G. Ma, G.Wu, X. Zong, Z. Lei, J. Shi, C. Li, **J. Catal.,** 2009, 266, 165

17. Q. Li, B. Guo, J. Yu, J. Ran, B. Zhang, H. Yan, J. R. Gong, **J. Am. Chem. Soc.,** 2011, 133, 10878

18. Q. Xiang, J. Yu, M. Jaroniec, **Chem. Soc. Rev.,** 2012, 41, 782

19. Q. Xiang, J. Yu, **J. Phys. Chem. Lett.**, 2013, 4, 753

20. G. Xie, K. Zhang, H. Fang, B. Guo, R. Wang, H. Yan, L. Fang, J. R. Gong, **Chem. Asian J.**, 2013, 8,2395

21. G. Xie, K. Zhang, B. Guo, Q. Liu, L. Fang, J. R. Gong, **Adv. Mater.**, 2013, 25, 3820

22. K. Zhang, L. Guo, **Catal. Sci. Technol.,** 2013, 3, 1672

23. Q. Xiang, J. Yu, M. Jaroniec, **J. Phys. Chem. C.,** 2011, 115, 7355

24. Y. Ding, Y. Wang, J. Ni, L. Shi, S. Shi, W. Tang, **Physica B,** 2011, 406, 2254

25. K. S. W. Sing, D. H. Everett, R. Haul, L. Moscou, R. A. Peirotti, J. Rouquerol, T. Siemieniewska, **Pure Appl. Chem.,** 1982, 54, 2201

26. C. M. Fang, R. A. de Groot, C. Haas, **Phys. Rev. B,** 1977, 56, 4455

27. R. A. Pollak, D. E. Eastman, F. J. Himpsel, P. Heimann, **Phys. Rev. B,** 1981, 24, 7435

28. Y.B. Qiao, Y.-L. Li, G.-H. Zhong, Z.Zeng, X.-Y. Qin, **Chin. Phys.,** 2007, 16, 3809

29. S. R. Lingampalli, U. K. Gautam, C. N. R. Rao, **Energy Environ. Sci.,** 2013, 6, 3589

30. J. Jin, J. Yu, G. Liu, P. K. Wong, **J. Mater. Chem. A,** 2013, 1, 10927

31. J. Zhang, S. Z. Qiao, L. Qi, J. Yu, **Phys. Chem. Chem. Phys.,** 2013, 15,12088

32. L. Jia, D. Wang, Y. Huang, A. Xu, H. Yu, **J. Phys. Chem. C,** 2011, 115, 11466

33. Y. Wang, Y. Wang, R. Xu, **J. Phys. Chem. C,** 2013, 117, 783

34. X. Zong, G. Wu, H. Yan, G. Ma, J. Shi, F. Wen, L. Wang, C. Li, **J. Phys. Chem. C,** 2010, 114, 1963

Appendix

A brief overview on transition metal dichalcogenides

Introduction

Recently, 2D-materials have opened up a new dimension of research as not only composition or structure of material but also dimension of the material will play a crucial role in their basic properties. Single layer of graphite also known as graphene, shows phenomenal properties which were absent in its 3D-form graphite [1-3]. Increasing interest in graphene has led to exploration of other 2D-materials [4-17]. Among all the 2D materials transition metal dichalcogenides, having structure similar to graphite, have been of particular interest for their different electronic properties, like from metallic to sizable band gaps. Also this materials are readily available in nature. Graphene, by nature is metallic in nature and in order to introduce band gap in graphene or some functionality we need to modify it with other molecules [18] or functional groups, which result in loss of some of its properties. However, in single-layered 2D transition metal dichalcogenides exhibit variety of properties and chemistry. This opens up wide variety of applications in electronics, catalysis, energy storage and other applications. In bulk they also exhibit variety of properties like insulating HfS_2, semiconducting such as MoS_2, semi-metallic such as $TiSe_2$, to true metallic system like NbS_2. Some transition metal dichalcogenides like exhibit low temperature superconductivity, Charge density wave and Mott metal to insulator transition. [19-21]

Many transition metal dichalcogenides crystallize in graphite-like layered structure which leads to anisotropy in their electrical, thermal, mechanical and sometimes chemical properties [22].

On exfoliating these materials into mono to few-layers generally preserves their property and sometimes brings up new properties due to their confinement in particular dimension. [7-9].

Crystal phases and electronic structure

Group 4–7 transition metal dichalcogenides are generally layered, whereas some of group 8–10 Transition metal dichalcogenides are commonly non-layered structures.

Single-layered 2D transition metal dichalcogenides has general formula of MX2, where M is a transition metal of groups 4–10 and X is a chalcogenides. Metal atoms are hexagonally packed and sandwiched between two layers of chalcogen atoms. The intra-layer M–X bonds are covalent in nature, whereas the sandwich layers are weakly bonded by van der Waals force. Thus we can readily exfoliate the crystal along the layer surface. The single layers are stabilized by development of a ripple structure similar to graphene. [23, 24]

There are two co-ordination type, trigonal prismatic (with point group as D_{3h}) or trigonal antiprismatic or octahedral (with point group as D_{3d}) which gives rise to three crystal phases (Figure 1.) trigonal, hexagonal and rhombohedral. They are depicted as 1T, 2H and 3R where letters stand for trigonal, hexagonal and rhombohedral, respectively and the number represent the number of MX_2 units in the unit cell. Both 3R and 2H form has trigonal prismatic co-ordination, while 1T has octahedral coordination.
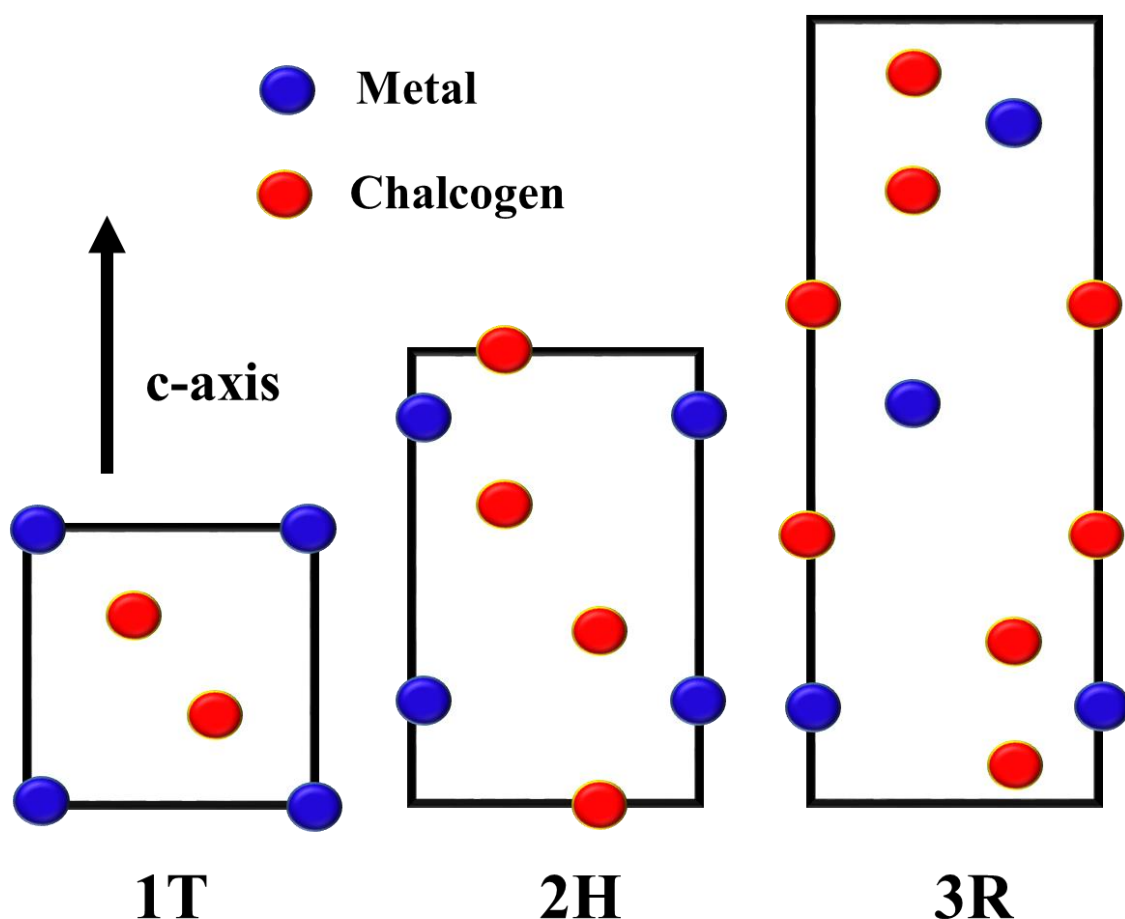
Figure 1. *Schematic showing the stacking sequences and coordination in the 1T, 2H and 3R polytype of Metal (M shown in blue) and chalcogen (X=shown in red). The structures are shown as projections onto the (110) plane.*

In 2H crystal structure we have AbA type of packing, in 1T phase we have AbC type packing and in 3R phase we have AbA CaC BcB type of packing [25], (The upper case shows chalcogen and lower case shows metal atoms.). These crystal structure can be differentiated by using different techniques like high resolution transmission electron micrography in annular dark field mode [12, 26].

Metal atom provide four electrons to fill the bonding states so that the oxidation states of the metal (M) is +4 and chalcogen (X) atom is –2. The lone-pair electrons of the chalcogen atoms terminate the surfaces of the layers, and the absence of dangling bonds makes them stable

against reactions in ambient conditions. The electronic structure of transition metal dichalcogenides depends upon the d-electron count of the metal atom.
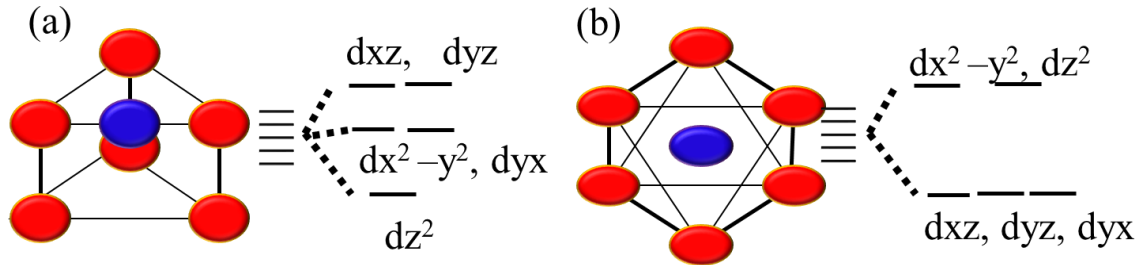
Figure 2. *Shows coordination and splitting of the d-orbital of the metal (shown in blue) ion co-ordinated by chalcogen (shown in red) in (a) trigonal prismatic field and (b) octahedral.*

The metal atom in transition metal dichalcogenides can be either trigonal prismatic or octahedral (trigonal-antiprismatic) typically distorted shown in Figure. 2, depending on the combination of the metal and chalcogen elements, one of the two coordination modes is thermodynamically preferred and also splitting of these orbitals in their field is shown in the Figure 2. In trigonal prismatic (D_{3h}) coordination the d-orbitals split into three sets of orbitals, d_z^2 (a_1), $d_{x^2-y^2}$, d_{yx} (e) and d_{zx}, d_{yz} (e') having a band gap near (~1eV) between the a_1 to e set of orbitals. In octahedral (D_{3h}) environment, the d-orbitals split into two set of degenerate orbitals d_z^2, $d_{x^2-y^2}$ (e_g) and d_{yx}, d_{zx}, d_{yz} (t_{2g}) (Shown in Figure. 2).

For example, MoS_2 is naturally present in 2H-form, whereas TaS_2 is present as 1T-form in nature. In both the form, the non-bonding d-bands of the transition metal dichalcogenides are located in the gap between the bonding (σ) and non-bonding ($\sigma*$) bands of metal chalcogen bonds shown in Figure 3 with respect to Fermi-level. Progressive increase in number of d-electrons from group 4 to 10 gives different electronic property illustrated in Figure 3.
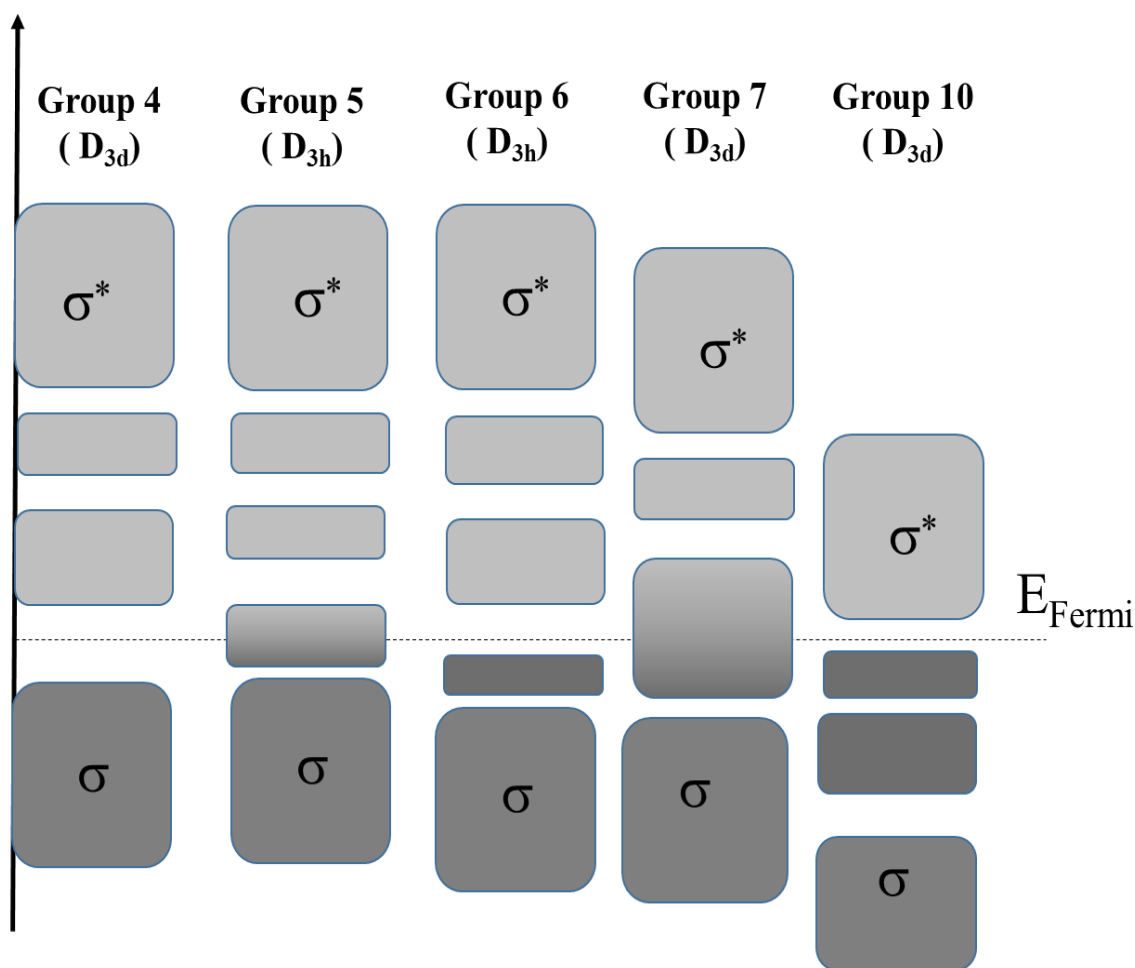
Figure 3. *Schematic representation showing filling of electrons in d orbitals that are located within the bandgap of bonding (σ) and non-bonding (σ*) bands of transition metal dichalcogenides of Group 4-7, 10 of their naturally abundant state. The filled and unfilled are shaded as grey and light grey respectively.*

Transition metal dichalcogenides of Group 4 (d^0) can be present as semiconductor and band gaps vary depending on the metal atom and chalcogen atom. Group 5 (d^1) is metallic in nature as the orbital is partially filled and Fermi level lies within the band. Group 6 (d^2) has fully filled orbital and the Fermi level is in the energy gap, so it is semiconducting in nature. Similarly band gap varies on the nature of metal and chalcogen atom in group 6. Similar to group 5, group 7 (d^3) has partially filled d orbital with Fermi level within the band, so it exhibits

metallic properties. Similarly for group 10 (d^{10}) we have fully filled d-orbital and the Fermi level lies in the energy gap, therefore they are semiconductor.

Interestingly one can change the electronic property of the transition metal dichalcogenides by changing the crystal structure. For example, lithium intercalation in MoS_2 followed by exfoliation transforms from 2H to 1T polymorph [25-29]. This implies that semiconducting 2H-MoS_2 will become metallic in 1T-MoS_2, in principle. The reverse takes places in case of TaS_2, 1T-phase to 2H-phase transition, on Li intercalation [30]. This destabilization of the original phase is be because of the change in the *d*-electron count by transfer of an electron from the valence *s* orbital of the alkali metal to the *d* orbital of the transition metal and also due to the relative change in the free energy of the two phase.

In the following chapters we have studied the transition metal and dichalcogenides of Group 4 (TiS_2), Group 5 (TaS_2) and Group 6 (MoS_2 and $MoSe_2$). We have studied their electrical and structural properties and their applications in Hydrogen evolution reaction (HER).

References

1. K. S. Novoselov, A. K. Geim1, S. V. Morozov, D. Jiang, Y. Zhang, S. V. Dubonos, I. V. Grigorieva1, A. A. Firsov, **Science**, 2004, 306, 666–669

2. A. H Castro Neto, F. Guinea, N.M.R Peres, K.S Novoselov, A.K Geim, **Rev. Mod. Phys.,** 2009, 81, 109–1623

3. A.K Geim, **Science,** 2009, 324, 1530–1534

4. Q.H. Wang, K. Kalantar-Zadeh, A. Kis, J.N Coleman, M.S. Strano, **Nature Nanotech.,** 2012, 7, 699–712

5. K. F. Mak, C.Lee, J. Hone, J. Shan, T.F Heinz, **Phys. Rev. Lett**., 2010, 105, 136805.

6. A. Splendiani et al., **Nano Lett., 2010,** 10, 1271–12757.

7. Cao, T. et al. **Nature Commun**.,2012, 3, 887.

8. H. Zeng, J. Dai, W. Yao, D. Xiao, X. Cui, **Nature Nanotech**., 2012, 7, 490–493

9. K.F Mak, K. He, J. Shan, T.F Heinz, **Nature Nanotech.,2012, 7,** 494–498.

10. H. Li, *et al.* **Small,** 2012, 8, 682–686.

11. G. Eda, *et al.* **Nano Lett.**, 2011, **11,** 5111–5116

12. G. Eda, T. Fujita, H. Yamaguchi, D. Voiry, M. W Chen, M. Chhowalla, **ACS Nano 6,** 2012, 7311–7317

13. Z. Yin, *et al.* **ACS Nano***,*2012*,* 6**,** 74–80.

14. A. Castellanos-Gomez *et al.* **Nano Lett.,** 2012**,** 12**,** 3187–3192.

15. J. Feng, *et al.* **Adv. Mater.**,*2012,* **24,** 1969–1974

16.H.S.S.R Matte, *et al.* **Angew. Chem. Int. Ed.**, 2010, 49**,** 4059–4062.

17. H. Li, H. *et al.* **Small***,* 2012, **8,** 63–67.

18. K.P Loh, Q. L Bao, G. Eda, M. Chhowalla, **Nature Chem.***,* 2010, **2,** 1015–1024.

19. B. Sipos, *et al.* Nature Mater. 2008, **7,** 960–965.

20. R.A Gordon, D. Yang, E.D Crozier, D.T Jiang, R.F Frindt, **Phys. Rev. B**, 2002, 65**,** 125407.

21. A. Kuc, N. Zibouche, T. Heine **Phys. Rev. B,** 2011, 83, 245213.

22. J. A. Wilson, F. J. Di Salvo, S. Mahajan, **Adv. Phys., 1975,** 24**,** 117–201.

23. J. C. Meyer, A. G. Geim, M. I Katnelson, K.S Novoselov, S. Roth, **Nature,** 2006 446, 60–63.

24. S. Bertolazzi, J. Brivio, A. Kis, **ACS Nano***,* 2011, 5**,** 9703–9709.

25. J. A Wilson, A. D Yoffe, **Adv. Phys., 1969** 18**,** 193–335.

26. U. Maitra, U. Gupta, M. De, R. Datta, A. Govindaraj, C. N. R. Rao, **Angew. Chem. Int. Ed.**, 2013, 52, 13057–13061

27. R. Bissessur, M. G.. Kanatzidis, J. L Schindler, C. R Kannewurf, **J. Chem. Soc. Chem. Commun.,** 1993 1582–1585.

28. R. F. Frindt, A. D Yoffe, **Proc. R. Soc. Lond. A***,* 1963, **273,** 69–83.

29. M.A Py, R. R Haering, **Can. J. Phys.,** 1983, 61**,** 76–84.

30. P. Ganal, W. Olberding, T. Butz, **Solid State Ionics***,* 1993*,* 59, 313–319.

Chapter 4

Highly Effective Visible-Light-Induced H₂ Generation by 2H- and 1T- forms MoS₂ and MoSe₂

Summary*

The 2H polymorph of MoS₂ has earlier been proven to be a good catalyst for electrochemical as well as photochemical hydrogen evolution reaction. Band offset of Group 6 metal dichalcogenides have their conduction band minimum which lies above the water reduction position and would therefore be an appropriate material for hydrogen evolution reaction (HER).Theoretical and experimental studies indicate that metallic edges of MoS₂ are catalytically active while the basal plane remains inert, so a metallic MoS₂ would greatly enhance its photocatalytic activity. On lithium intercalation and exfoliation of bulk Group 6 metal dichalcogenides yield metallic 1T-form which has been employed for the visible-light-induced generation of hydrogen. The 1T-form is found to be superior than the 2H-form in producing hydrogen from water which is supported by first principles calculations, which reveal that the 1T-form has a lower work function than the 2H-form, making it easier to transfer an electron from 1T form for the production of H₂. In addition, it is also found that 1T-MoSe₂ is superior not only to its 2H-form but also to both 1T and 2H MoS₂ as the conduction band minimum of MoSe₂ is ~0.37eV higher than that of MoS₂.
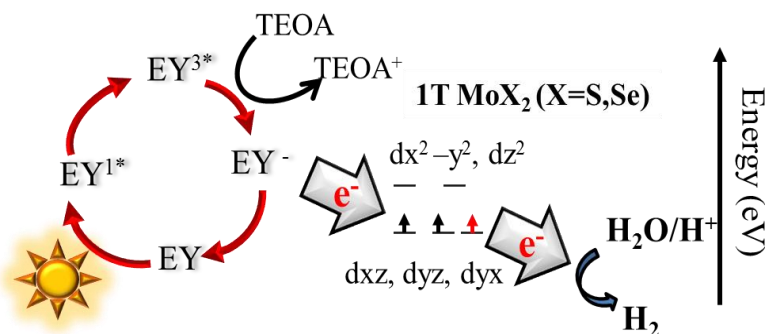
Introduction

Over the past decade, replacing fossil fuels by renewable sources of energy has become a major research goal not only because of the dwindling resources of fossil fuels but also due to harmful effects of CO_2 and other gases produced by combustion of the fuels. Hydrogen produced from water using solar energy is clearly the ultimate source of clean renewable energy. Traditionally, H_2 is generated from water using Pt electrodes, and several catalysts have been used for electrocatalytic, photocatalytic and photoelectrocatalytic production of hydrogen.[1,2]
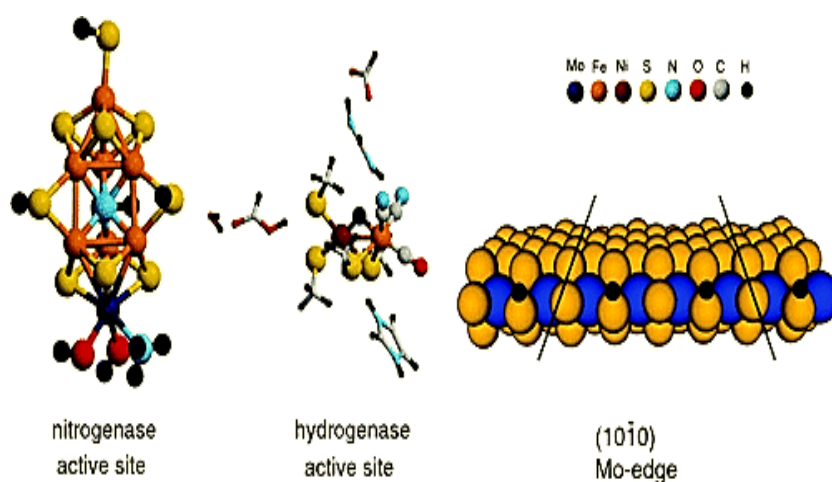
Figure 1. *(Left) Nitrogenase FeMo cofactor (FeMoco) with three hydrogen atoms bound at the equatorial í2S sulfur atoms. (Middle) Hydrogenase active site with one hydrogen atom bound. (Right) MoS₂ slab with sulfur monomers present at the Mo edge. The coverage is 50%, i.e., hydrogen is bound at every second sulfur atom. The lines mark the dimension of the unit cell in the x-direction. [adapted from ref. 3]*

In natural systems proton reduction is catalyzed by hydrogenase and nitrogenase, enzymes catalytic centre of which is mainly composed of earth abundant non-noble metal elements like Fe, Ni, Mo (Figure 1). Recent DFT calculations have revealed that free energy of hydrogen evolution on MoS_2 is comparable to hydrogenase, nitrogenase as well

as Pt (Figure 2). The free energy was calculated based on the consideration that a catalyst should bind atomic H with just the appropriate strength (not too strong and not too weak) such that both binding and release of hydrogen is equally feasible.
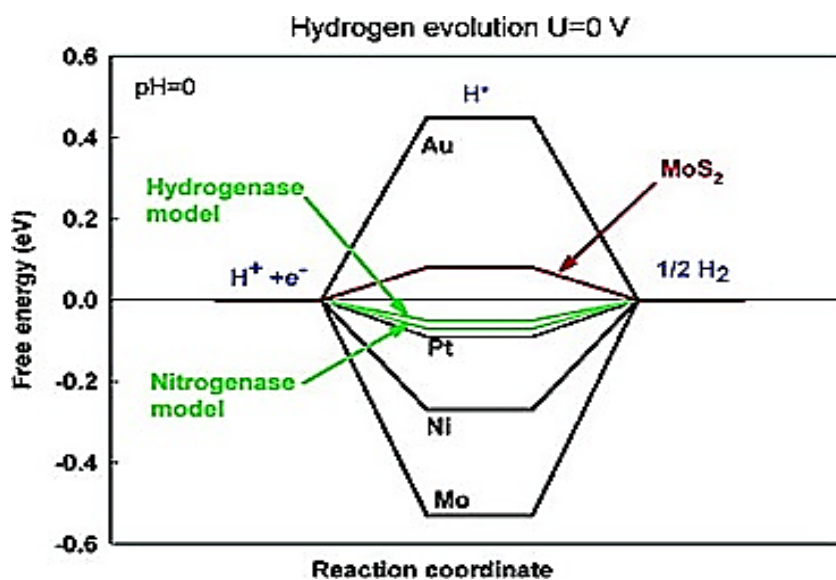
Figure 2. *The free energy of H atoms bound to different catalysts is then found by calculating the free energy with respect to molecular hydrogen including zero-point energies and entropy terms. (adapted from ref 3.)*

Based on this consideration the necessary condition for a catalyst to act as a good proton reduction catalyst is that the free energy of adsorbed H is close to that of the reactant and product i.e. the $\Delta G^0 \approx 0$.[3] It was also found that the edge structure of MoS_2 sheets have close resemblance with the catalytically active sites of nitrogenase and hydrogenase.

MoS_2 is an established catalyst for the hydrodesulfurization reaction [4] proven to be a good catalyst for electrochemical as well as photochemical hydrogen evolution reaction (HER) [5-8]. Theoretical and experimental studies indicate that edges of MoS_2

are catalytically active while the basal plane remains inert.[3,9] Nanoparticles of MoS_2 with single-layered truncated triangular morphology with exposed Mo edges,[9, 10] or those grown on highly ordered pyrolytic graphite[11] or graphitic carbon[12] are catalytically active. Electrochemical HER carried out with nanoparticles of MoS_2 supported on carbon[13] and fluorine-doped tin oxide electrode[14] show higher yields of H_2. Hydrogen evolution appears to be further enhanced by using graphene[15] or carbon nanotubes[4] to support nanocrystalline MoS_2, the favorable conductivity of the nanocarbons ensuring efficient electron transfer to the electrodes. MoS_2 possessing the double gyroid structure with a large number of interconnected pores showing the highest photo-electrocatalytic activity [16] While electrochemical HER by MoS_2 has been studied in detail, photocatalytic HER by MoS_2 has received less attention. Bulk MoS_2 being an indirect band gap (1.29 eV) semiconductor does not absorb the solar spectrum efficiently. If we somehow can put an electron on the conduction band of the MoS_2we can expect MoS_2 to perform as photocatalytic HER (Scheme 1.), like on sensitization with $[Ru(bpy)_3]^{2+}$ ions colloidal MoS_2 nanoparticles show photocatalytic HER activity with a turn over number (TON) of 93. The method utilizes a three-component system with ascorbic acid as the reductive quencher for excited state $[Ru(bpy)_3]^{2+}$ which in turn transfers electrons to MoS_2.[17] MoS_2 loaded on TiO_2[18] and CdS[19] has been investigated for H_2 evolution where TiO_2 and CdS act as both light absorbers and catalysts.
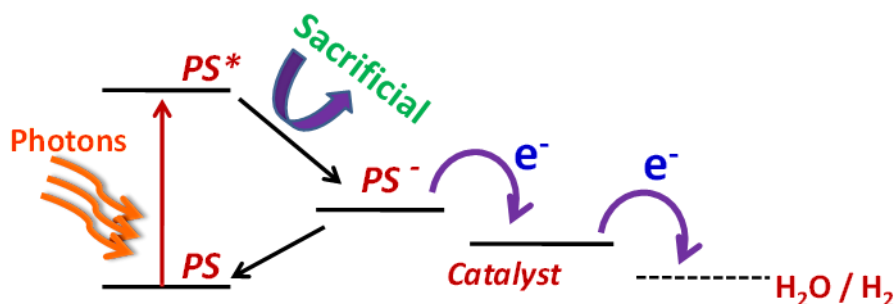
Scheme 1. *Schematic representation of dye-sensitized catalysts for reduction of water.*

Few-layer MoS_2 loaded on reduced graphene oxide (RGO) shows good HER activity compared to MoS_2 or its physical mixture with RGO, with EosinY as sensitizer.[20] Here in graphene–MoS_2 composites, graphene acts as a channel for transferring electrons to MoS_2 enhancing the visible-light driven H_2 generation by few-layer 2H-MoS_2. Nitrogen incorporation in graphene is expected to improve the catalytic activity of the composite with 2H-MoS2 layers since it enhances the electron donating ability of the graphene, composite with heavily nitrogenated RGO (%N ca. 15) which shows excellent HER activity of 10.8 mmoles h^{-1} g^{-1} and a turn over frequency of 2.9 h^{-1} under a 100W halogen lamp[21].

Scope of the present investigations

Exfoliation of these dichalcogenides into single or few-layers often brings out drastic changes in the electronic structure as compared to their bulk forms. Dichalcogenides of MoS_2 and WS_2 mostly occur in the 2H form *i.e.* having trigonal prismatic arrangement of hexagonal S-M-S (M = Mo/W) triple layer and are among the most studied of the layered metal chalcogenides owing to their interesting electronic properties. While 2H forms of these metal dichalcogenides are semiconducting, their 1T forms are metallic [22-24].

For the band off set diagram of the Group 6 transition metal dichalcogenides (Figure 3.) We observe that the conduction band of MoS_2 is more negative than water reduction value and more positive than water oxidation value [25, 26]. While in case of $MoSe_2$ the conduction band is more negative that water reduction potential and also MoS_2.
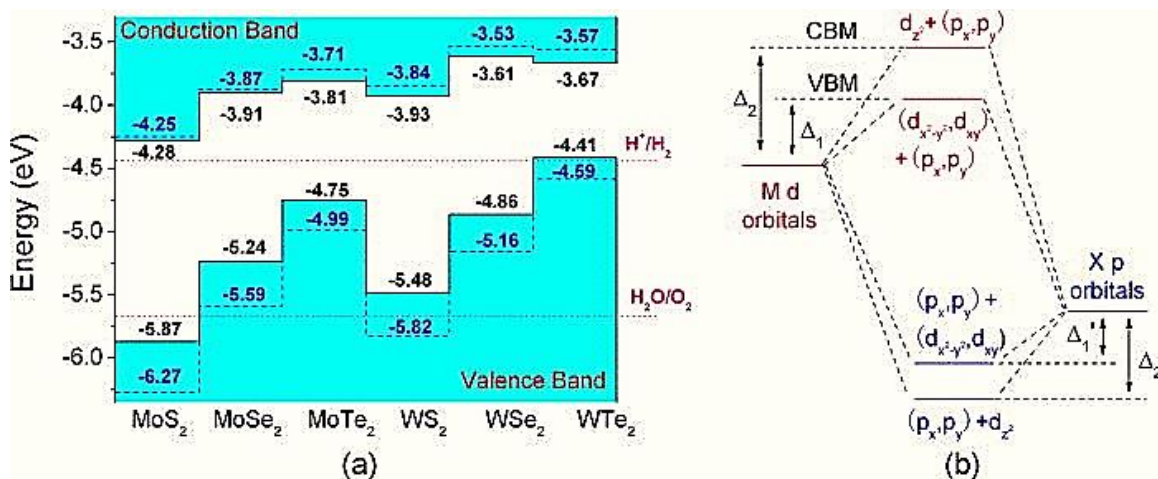
Figure 3. *(a) Calculated band alignment for MX_2 monolayers. Solid lines are obtained by PBE, and dashed lines are obtained by HSE06. The dotted lines indicate the water reduction (H^+/H_2) and oxidation (H_2O/O_2) potentials. The vacuum level is taken as zero reference. (b) Schematic of the origin of CBM and VBM in MX_2. (adpted from ref. 26)*

The CBM is located at a more negative potential than the proton reduction potential (H+/H2), while the VBM is positioned more positively than the oxygen reduction potential (O_2/H_2O). The bandgap of about 1.7 eV is ideal for visible light active photocatalyst as well as the effective utilization of the solar energy.

The rate constant of a chemical reaction can be given by Arrhenius equation,

$$K = Ae^{RT/Ea} \qquad (Equation. 1)$$

where A is the pre-exponential factor, R is the universal gas constant, and E_a is the reaction energy barrier. The reaction barrier in photocatalytic redox reactions of water is complex. In a much closer examination, the oxidizing power (denoted as Δ_2 that is defined as the

difference between VBM band edge and the oxygen reduction potential. However, the reducing power (denoted as Δ_1), which is defined as the difference between the proton reduction and the CBM edge potentials.

But, it can be understood by the difference between the reaction rate of reduction and oxidation. The energy barrier can be minimized by reducing the difference between Δ_1 and Δ_2, and improved efficiency of the reaction can be achieved. Which also suggests that MoS_2 is a good candidate for reduction but not for oxidation. The bigger the barrier (large difference between Δ_1 and Δ_2) would imbalances the reduction and oxidation reactions, which inhibits the progress of the overall redox reaction. If we can decrease the difference between Δ_1 and Δ_2 we can further improve its efficiency for water splitting. The difference between Δ_1 and Δ_2, can loosely be termed as the band gap of the material, and if we can reduce the band gap of the material we can increase the activity of MoS_2 one of the way would be using Se, as band gap of $MoSe_2$ is less than that of MoS_2 and other would by using 1T-MoS_2 prepared by the exfoliation of bulk MoS_2 by Li-intercalation. However, imbalance between the reduction reaction and oxidation reaction would prevent the process of redox reactions. If we can find an oxidizing material which oxidizes at lower potential then water this process can be enhance effectively.

This is shown in literature 1T-MoS_2 is a better catalyst than its 2H form electrochemically [27-28]. As in case of 1T-MoS_2, the 1T form of $MoSe_2$ too is metallic and could be expected to be a better catalyst than its 2H analogue for visible-light-induced water reduction.

Experimental Section

Synthesis

300mg of $MoSe_2$, procured from Alfa-aesar was taken in a 20 ml vial with a cap and to it 10 ml of 1.6M n-butyl lithium in Hexane was added and was stirred for 3 weeks. The sample was washed with hexane 3 times and centrifuged at 8000 rpm for 5 minutes each. The centrifuged product was then exfoliated in water by sonication. The dispersion was dialysed for 12 hours to remove excess of LiOH from the solution. [29-31]

The few layer 2H-$MoSe_2$ was synthesized using selenourea, where Molybdic acid and selenourea in mass ratio 1:24 was heated at $500^{\circ}C$ under N_2 flow for 5 hours. Both 1T-MoS_2 and 2H-MoS_2 were synthesized under similar conditions for comparison with $MoSe_2$. [32]

Characterization

HRTEM was performed in a FEI TITAN cubed double aberration corrected 80–300 keVmicroscope. Negative Cs imaging was used (Cs $\approx$ 35–40 mm, $\Delta f \approx$ +8 nm) to image atoms with white contrast and direct interpretation. Raman spectra were recorded with a Horiba-Jobin Yvon LabRAM HR Raman spectrometer using Ar laser (λ = 514.5nm) with D1 filter. Inductively coupled plasma optical emission spectroscopy (ICP–OES) was used to determine the concentration of $MoSe_2$ and MoS_2 in the water dispersion of 1T-MoX_2 using a Perkin-Elmer Optima 7000 DV instrument.

Photocatalytic measurements

Photocatalytic measurements of the sample were carried out as follows. The required amount of dispersion of the catalyst was t dispersed in water (40 mL) and triethanolamine (15% v/v; 8 mL). The vessel was thoroughly purged with N_2. 1ml of 0.015 mM solution Eosin Y in Ethanol was then added as the sensitizer. The vessel was irradiated under 100W halogen lamp (flux of 300 Wm^{-2}) with constant stirring of the mixture. 1 mL of evolved gases were manually collected from the headspace of the vessel at regular time interval and analyzed in PerkinElmer Clarus ARNEL 580 gas chromatograph.

Turn over frequency (TOF) was calculated as follows

$$TOF\ (h^{-1}) = \frac{\text{Moles of } H_2 \text{ evolved per hour}}{\text{Moles of Active Catalyst}} \qquad (Equation.\ 2)$$

Results and Discussion

As discussed in the chapter 3 Group 6 transition metal dichalcogenides undergo change in phase from 2H to 1T on lithium intercalation and exfoliation.Bulk MoX_2 in the 2H form was intercalated with lithium using n-butyl lithium and exfoliation carried out by reacting the intercalated product with water [29-31].The energy liberated during the formation LiOH is highly exothermic and provides the driving for the formation of layers of the 1T form.
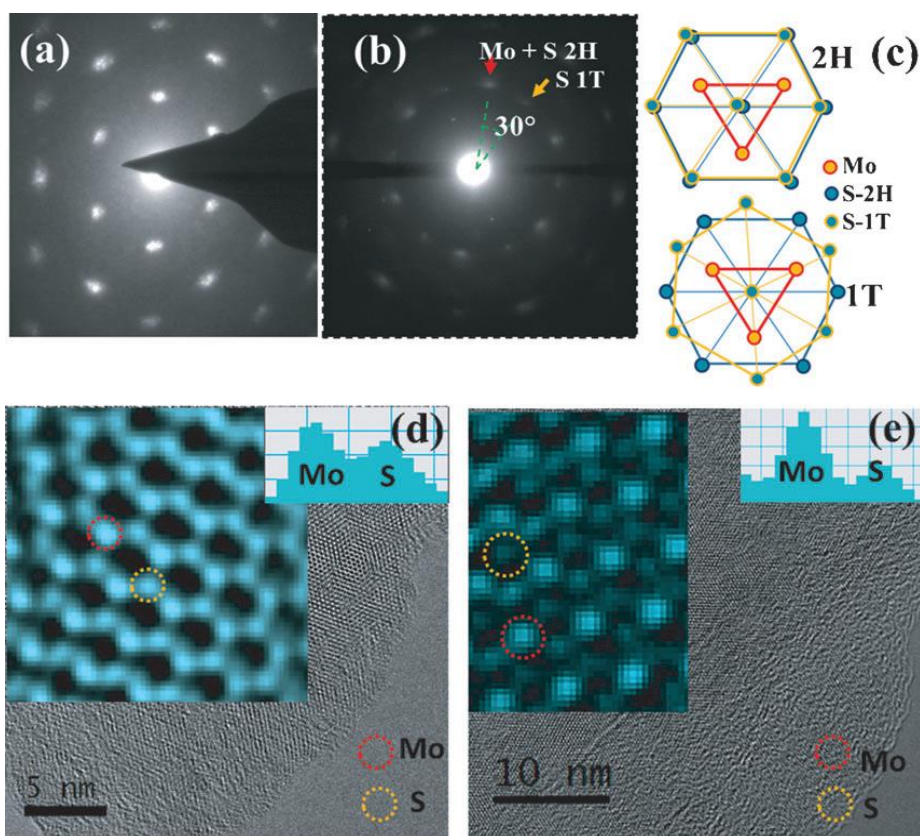

Figure 4. Electron diffraction patterns from single-layer MoS_2 with a) the 2H and b) 1T structures. c) Schematic structural model corresponding to the 2H and 1T structures. HRTEM images of the d) 2H and e) 1T structures. The insets in (d) and (e) show magnified images of Mo and S atomic arrangements in 2H and 1T structures as well as intensity line scans through Mo and S atoms.

The electron diffraction pattern of 2H-MoS$_2$ shows the usual hexagonal spot pattern (Figure 4a), but 1T-MoS$_2$ shows an extra the electron diffraction pattern and the HRTEM images of 2H and 1T MoS$_2$ are given in Figure hexagonal spot at 30° angular spacing in between the hexagonal spots of the 2H structure (Figure 4b).Figure 4c shows the schematic representation of 2H- and 1T-MoS$_2$ structures. 2H-MoS$_2$ has trigonal prismatic arrangement of Mo and S atoms, with the S atoms in the lower layer lying directly below those of the upper layer. In 1T-MoS$_2$, on the other hand, the S atoms in the upper and lower planes are offset from each other by 30° such that the Mo atoms lie in the octahedral holes of the S layers. The extra spot in electron diffraction arises from this rotation of one of the S atomic layers with respect to another. Figure 4d and 4e show the HRTEM images for single layer of 2H-MoS$_2$ and 1T-MoS$_2$. In case of 2H-MoS$_2$ three S atoms surrounds one Mo atom whereas for the 1T structure six S atoms can be seen surrounding one Mo atom. Intensity line scans through Mo and S atoms show a higher intensity difference for the 1T structure (one S atom in projection) compared to the 2H structure (2S atoms together in projection). This difference in contrast is related to the corresponding phase shift (related to the net atomic number) under negative Cs (third-orderspherical aberration coefficient) imaging conditions.[33] HRTEM of 1T-MoSe$_2$(Figure 5 a)form has the $\sqrt{3}a \times a$ arrangement which is related to its electronic structure.[30,34] The shifting of the atoms from their equilibrium positions, probably arises because of the Jahn-Teller instability, resulting in chain clusterization of the metal atoms with the formation of a superlattice.[35]
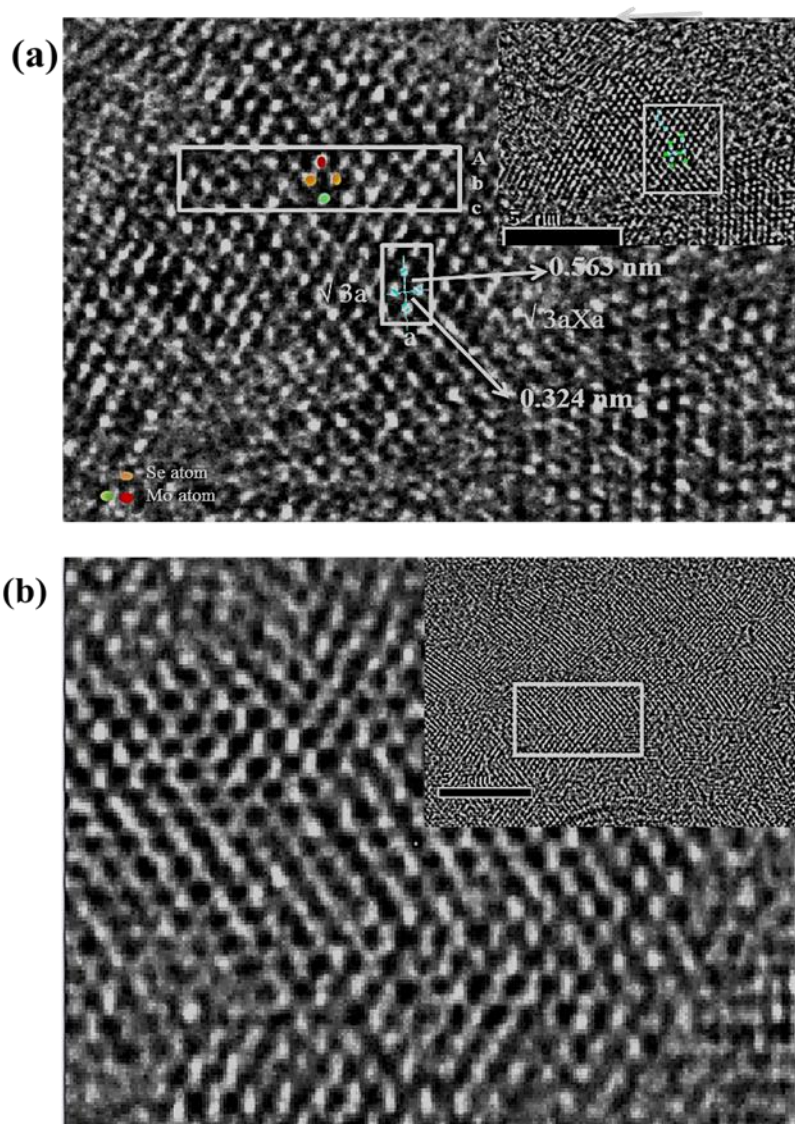
Figure 5. *HRTEM of (a) 1T-MoSe$_2$ (b) 2H-MoSe$_2$*

The Mo atoms in the 2H form of MoSe$_2$ have trigonal prismatic coordination as is evident from the high resolution TEM image in Figure 5b. The packing of atoms in 2H MoSe$_2$ is AbA type while in the 1T form it is AbC type.

The point group of the trigonal prismatic 2H-MoS$_2$ and MoSe$_2$ is D$_{3h}$ while the 1T polytype belongs to the D$_{3d}$ point group [34]. The 1T phase exhibits a Raman spectrum which is distinctly different from that of the 2H-phase. In Figure 6, weshow the Raman Spectra of

the 1T phases of $MoSe_2$ and MoS_2 and compare them with the corresponding spectra of the 2H phases.
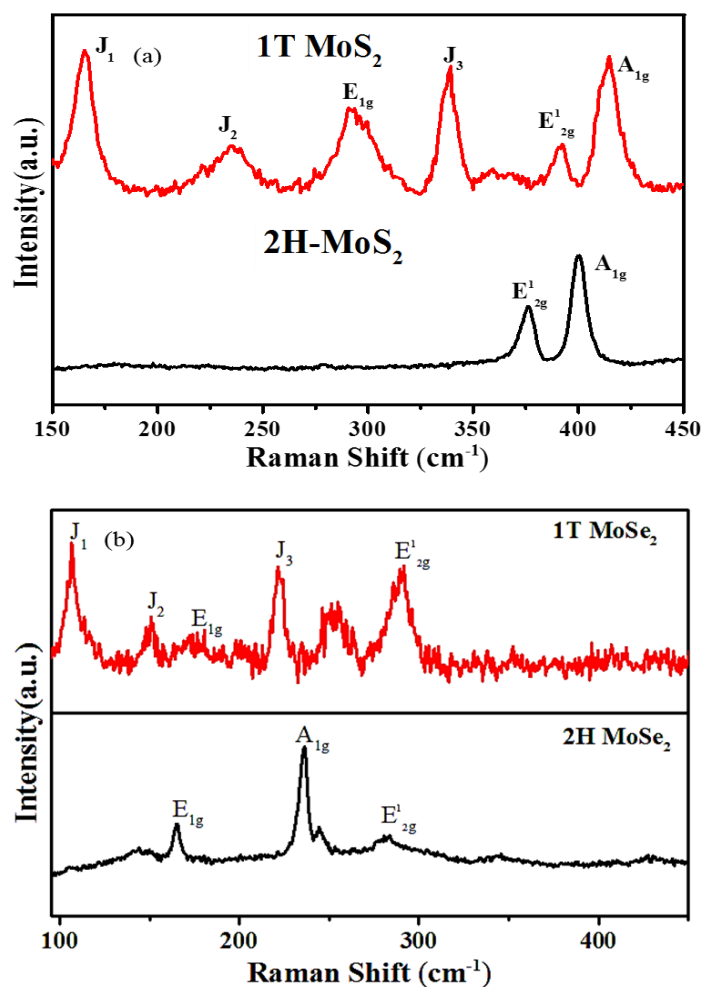
Figure 6.*Comparison of Raman spectra of (a) 1T-MoS₂ and 2H-MoS₂ and (b) 1T-MoSe₂ and 2H-MoSe₂*

The Raman spectrum of 2H-MoS_2 (Figure 6a) shows E^1_{2g} and A_{1g} bands at 375.9 and 400 cm^{-1} respectively. For 1T phase exhibits J_1,J_2 and J_3bands at 165.4, 236.6 and 339.3 cm^{-1}respectively, not present in 2H-MoS_2. The E^1_{2g} band, corresponding to in-plane vibration of MoS_2sheets is observed at 391.3 cm^{-1} in the 1T form and A_{1g} band, corresponding to out-of-phase, at 414.3 cm^{-1}.

The Raman spectrum of 2H-MoSe$_2$ shows E$_{1g}$, A$_{1g}$ and E$^1_{2g}$ bands at 165, 236.2 and 284 cm^{-1}, while the 1T phase exhibits J$_1$,J$_2$ and J$_3$ bands at 106.4, 150.7 and 221.4 cm^{-1} respectively, not present in 2H-MoSe$_2$. The E$^1_{2g}$ band, corresponding to in-plane vibration of MoSe$_2$ sheets is observed at 289.4 cm^{-1} in the 1T form and at 284 cm^{-1} in the 2H form. Interestingly, A^1_g band corresponding to out-of-phase vibration of MoSe$_2$, does not appear in the spectrum of the 1T form. (Figure 6b).

In Table 1, we provide a comparative table of the Raman frequencies of the 1T and 2H polytypes of MoSe$_2$ and MoS$_2$.

Table 1. *Raman band positions of 1T and 2H MoSe$_2$ and MoS$_2$*

Raman Modes	Few Layer 2H MoSe$_2$ (cm^{-1})	Few Layer 2H MoS$_2$ (cm^{-1})	1T-MoSe$_2$ (cm^{-1})	1T-MoS$_2$ (cm^{-1})	MoSe$_2$ bulk (cm^{-1})
J$_1$	---	---	106.4	165.4	---
J$_2$	---	---	150.7	236.6	---
J$_3$	---	---	221.4	339.3	---
A$_{1g}$	236.2	400	---	414.3*	240.1
E$_{1g}$	165		---	292.4	166.7
E$^1_{2g}$		375.9	289.4	391.3	---

Some 2H contribution.

The electronic structure of 1T-MoX$_2$ is different from that of 2H-MoX$_2$. The electronic structure proposed by Tenne *et. al.*[23] in the case of MoS$_2$ would apply to MoSe$_2$ (Figure 7.)
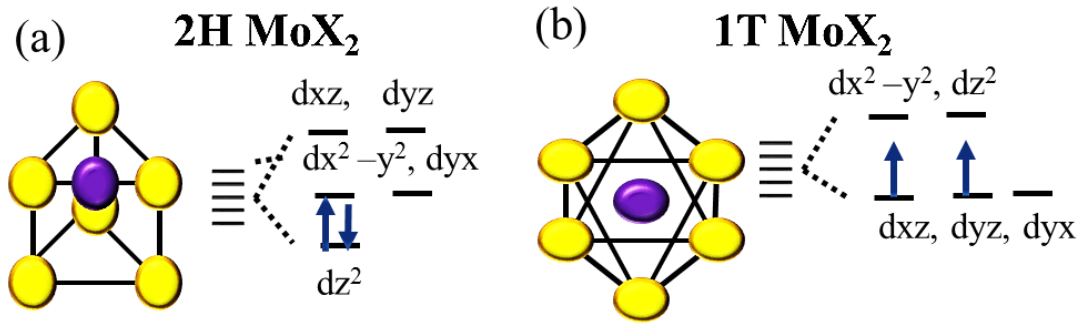
Figure 7. *The crystal field induced electronic configuration of (a) 2H-and (b) 1T- MoSe2 (Yellow = chalcogen atoms, Purple = Mo atom)*

The valence band of 2H-MoX$_2$ is composed of Se np states and the conduction band (CB) composed of Mo 4d states that lie above the Fermi level. According to crystal-field theory, hexagonal (D_{3h}) symmetry in 2H-MoSe2 would induce splitting of the Mo 4d orbitals into three sets of orbitals of closely spaced energies: dz2(a$_1$) and two pair of doubly degenerate orbitals composed of d$_{yx}$, d$_x^2$-$_y^2$(e) and dxz, dyz (e') as shown in Figure. 7a. The Mo 4d$_z^2$ level is occupied and spin-paired forming the valence band minimum (VBM), while the other four orbitals form the empty conduction band minimum (CBM). The symmetry of 1T-MoSe2 is D_{3d}, with Mo in octahedral coordination. The crystal-field splitting of Mo 4d under the octahedral $O_h$field generates three triply degenerate orbitals d$_{yx}$, d$_{zx}$, d$_{zy}$ (t$_{2g}$) containing two unpaired electrons and two empty doubly degenerate orbital d$_x^2$-$_y^2$, d$_z^2$ orbitals. The incompletely filled d$_{yx}$, d$_{zx}$, d$_{zy}$(e$_g$) orbital. It has now partially filled (Mo 4d^3) d orbital with Fermi level within the band, so it exhibits metallic properties. Based on the electronic configuration of 1T and 2H phases of MoX$_2$ it is clear that when an extra electron is added to 2H MoX$_2$, it resides in the degenerate d$_{yx}$, d$_x^2$-$_y^2$ states and destabilizes the lattice, while in case of 1T-MoX$_2$ the extra electron induces half-filled configuration of d$_{yx}$, d$_{zx}$, d$_{zy}$ and increases the stability of the 1T phase.

The hydrogen evolution activity of MoX_2 was studied using Eosin Y as the sensitizer and triethanolamine as the sacrificial electron donor. The reaction of dye-sensitized H_2 evolution over $MoSe_2$ involves photosensitization of Eosin Y followed by formation of Eosin Y anion (EY^-). EY^- being highly reactive donates this electron to MoX_2, which then catalyzes the reduction of proton to H_2 as shown in Figure 8.
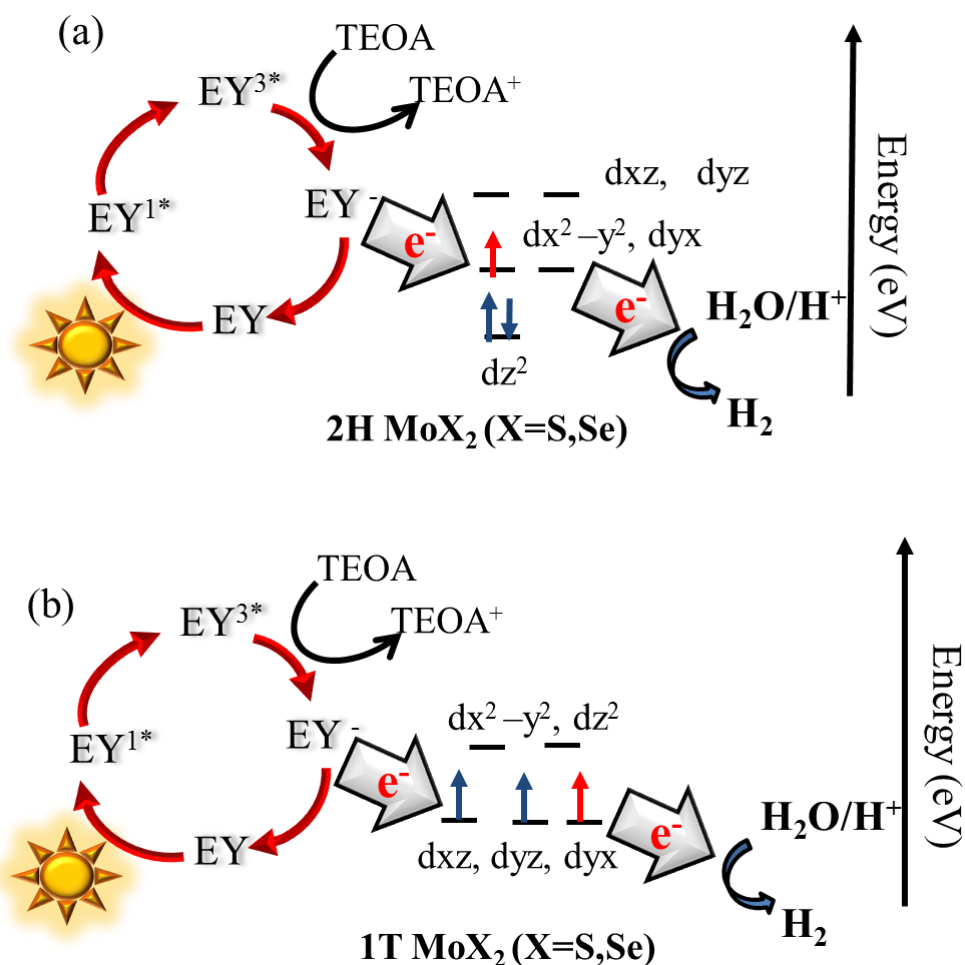
Figure 8. *The plausible mechanism of HER in case of (a) 2H-MoX₂ and (b) 1T-MoX₂*

In case of 2H MoX_2, only metallic edge sites are active and not the basal plane [3, 9]. When 2H-phase we have when electron is transferred from EY^- to 2H-MoX_2, the extra e^- added goes to conduction band $d_{x^2-y^2}$ and from there it is transferred to water which then catalyzes the reduction of proton to H_2 (Figure 8a). In 1T-MoX_2 is metallic in nature, it enhances the charge

separation and also increases the mobilityon its surface. EY$^-$ donates this electron to $4d_{yx}$ which then catalyzes the reduction of proton to H$_2$(Figure 8b).

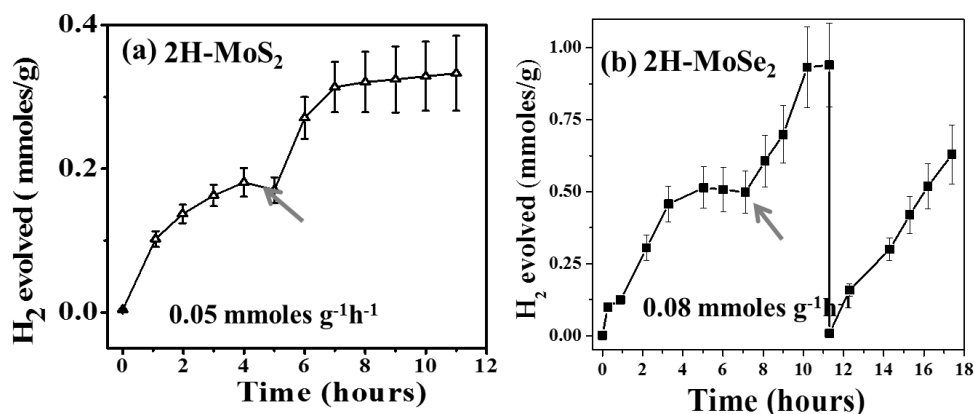The photocatalytic generated hydrogen was collected and regular time intervals and calculated.

Figure. 9. *HER activity of 2H form of (a) MoS$_2$ and (b) MoSe$_2$ over a period of time.*

Figure. 9 shows the time course of hydrogen evolution by 2H MoS$_2$ and MoSe$_2$. The 2H form of MoS$_2$ has activity of 0.05 mmol g^{-1}h^{-1} with TOF of 0.02 h^{-1} while MoSe$_2$ has activity of 0.08 mmol g^{-1}h^{-1} with a TOF of 0.008 h^{-1} shows better activity than that of 2H-MoS$_2$.

Photocatalytic activities of 1T-MoS$_2$ were studied by taking 2 ml of the dispersion of the sample in 50 ml 15% TEOA/water. The concentration of MoS$_2$ in the dispersion was determined from ICPES analysis. The concentration varied between 0.5 mg/ml to 2 mg/ml.We show the time course of H$_2$ evolution of single-layer 1T-MoS$_2$ in Figure 10(a). This catalyst evolved almost 30 mmoles g^{-1}h^{-1} of H$_2$, 600 times higher than few-layer 2H-MoS$_2$. Even under 100W irradiation, the TOF of the catalyst is estimated to be 6.2 h^{-1}, higher than any MoS$_2$ based system reported so far. The highest TOF reported thus far is 6 h^{-1}(under 300W Xe lamp) for [Ru(bpy)$_3$]$^{2+}$ sensitized colloidal MoS$_2$ nanoparticles (see

Table 1). 1T-MoS$_2$ evolves around 250 mmoles of H$_2$ corresponding to about 5.6 L of H$_2$per g of MoS$_2$ for 10 hrs.

The activity of the 1T-MoS$_2$ samples prepared by us varies from sample to sample depending on the amount of 1T phase present in the sample. Coexistence of metallic 1T-phase and semiconducting 2H-phases within chemically homogeneous nanosheets is known to occur in single-layer MoS$_2$ prepared by Li-intercalation and exfoliation. Figure 10(a) shows the time course of H$_2$ evolution by the sample showing the least yield among 10 experiments on different samples carried out by us, while Figure 11 (b) shows that for the sample with the highest yield. The sample showing the highest yield evolved ~55 mmoles g^{-1}h^{-1} with a TOF of ~ 11 h^{-1}. Figure 11 (b) shows the time course of H$_2$ evolution by 1T-MoS$_2$ over a period of 30 hrs, with the sample being purged after every 6hrs. The catalytic activity slowly degrades over the period from 55 mmoles g^{-1}h^{-1} to 30 mmoles g^{-1}h^{-1}.This could probably be because of the slow degradation of the 1T phase under the effect of heat from the light source. However, no significant quenching of the dye was observed even after 30hrs of reaction indicating and photogenerated species EY$^-$does transfer its elctrons to 1T-MoS$_2$ efficiently. To confirm that the high catalytic activity of MoS$_2$ prepared by Li-intercalation and exfoliation arises from 1T phase and is not a result of better dispersion and other such extrinsic factors we carried out control experiments with 2H-MoS$_2$ obtained directly from the 1T-MoS$_2$.1T-MoS$_2$ is reported to get converted to the 2H analogue on annealing under inert atmosphere. [36]We dried the dispersion by liophylization to obtain fluffy mass of 1T MoS$_2$. Since liophylization is carried out at low temperatures 1T-phase of MoS$_2$ is retained after liophylization.
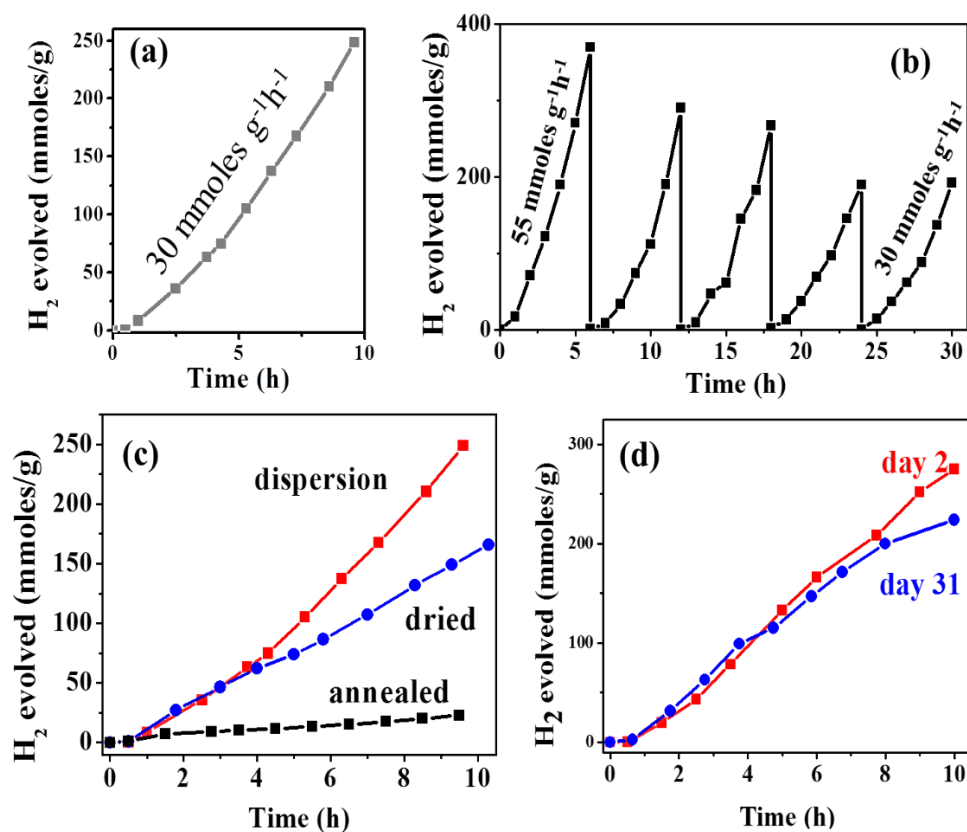
Figure 10.*Time course of H₂ evolution by 1T-MoS₂ - (a) sample showing the lowest yield of H₂, (b) sample showing the highest yield of H₂ shown over a period of 30 hrs with purging after every 6 hrs, (c) as prepared dispersion, dried by liophylization and annealed at 300°C for 1 hr and (d) as prepared dispersion, dispersion stored for 30 days.*

The lyophilized sample was annealed at 300°C for 1hto obtain the 2H analogue. We observe a drastic reduction in the catalytic activity of the annealed sample with rate of H_2 evolved being only 2.5 mmoles $g^{-1}h^{-1}$ a value closer to that found with 2H-MoS₂ (Figure 10 (c)). The 1T phase, of MoS₂ being the metastable polytype of MoS₂, is known to readily undergo transition to more stable 2H-polytype with time.[36] We therefore carried out photocatalytic H_2 evolution studies on fresh and 1 month old samples. The rate of H_2

evolution reduced only slightly over this period from 30 mmoles $g^{-1}h^{-1}$ to 26 mmoles $g^{-1}h^{-1}$ (Figure 10(d)).
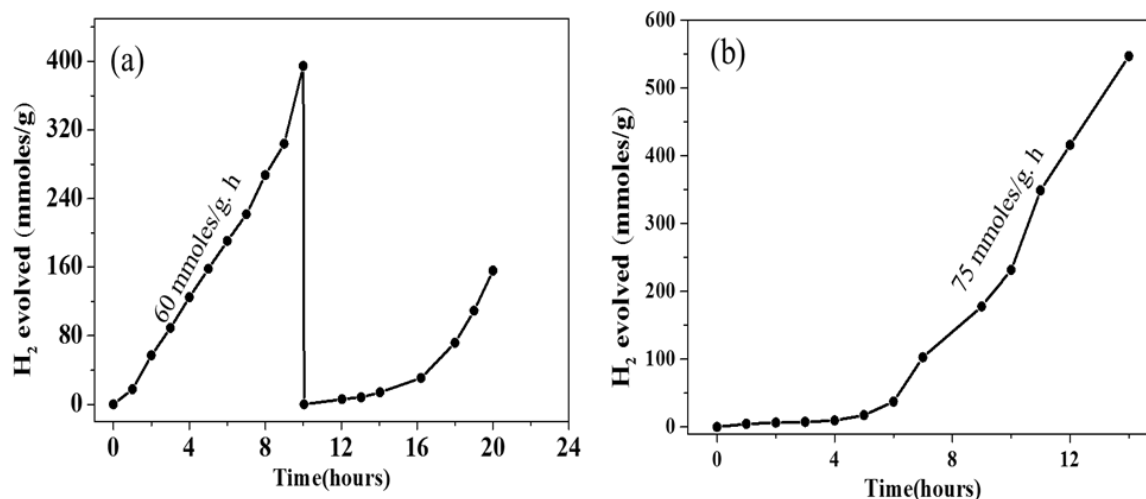

Figure 11. *Time course of H2 evolution by two independently prepared 1T-MoSe2 shown in (a) and (b) The slow reaction initially in (b) is due to the slow mixing of the reactants arising from the syrupy nature of triethanol amine.*

Based on these findings we have explored HER properties of $MoSe_2$, 2H and 1T form because of the fact that CBM of $MoSe_2$ ishigher than that of MoS_2.The yields of hydrogen are in range of the 60-75 mmol.$g^{-1}h^{-1}$. The turn over frequencies (TOF) are in the range 15-19 h^{-1}. The catalytic activity of the 1T form of $MoSe_2$ is nearly 750-900 times higher than that of the 2H form (activity of 0.08mmol g^{-1} h^{-1}) (Figure 9). It is noteworthy that the yield of H_2 and TOF with 1T-$MoSe_2$ is superior even to those found with 1T MoS_2. In Table 2, we have compared the hydrogen evolution activity and TOF of different transition metal chalcogenides. 1T-$MoSe_2$ shows higher activity compared to these transition metal chalcogenides and their composites. However, the activity for H_2 evolution is much lower in these systems as compared to 1T-$MoS_2$and 1T-$MoSe_2$. Greater stability afforded by the extra electron to Mo 4d level by inducing half-filled configuration of d_{yx}, d_{zx}, d_{zy}, as compared to

84

Ta 5d (with 1 electron) and Ti 3d (with no electron) is probably the reason for higher activity

of 1T-MoS$_2$ and 1T-MoSe$_2$.

Table 2.*Hydrogen evolution activity of MoSe$_2$, MoS$_2$ and TaS$_2$ based catalysts from earlier literature and present work.*

Compounds	Light Source	Activity (mmol h^{-1} g^{-1})	TOF (h^{-1})	Reference
MoS$_2$ /CdS	300 W Xe lamp	5.3	ca. 0.7	19
TaS$_2$ /CdS	400 W Xe lamp ($\lambda > 399$nm)	2.32	0.57	37
2H MoS$_2$[a]	100 W Halogen lamp	0.05	0.008	Present work
NRGO-MoS$_2$[a]	100 W Halogen lamp	10.8	2.9	21
1T MoS$_2$[a]	100 W Halogen lamp	30	6.5	Present work
1T-MoSe$_2$ [a]	100 W Halogen lamp	75	19.2	Present work
Few layer 2H MoSe$_2$[a]	100 W Halogen lamp	0.08	0.02	Present

TOF calculated per mole of catalytically active material (Graphene is considered to be inactive compared to MoS$_2$). [a] Eosin Y dye sensitized

First Principle analysis

(First principle analysis were done by Mrs. Anjali Singh and Ms. Sharmila Shirodkar and Prof. U.V. Waghmare in Theoretical Science Unit, JNCASR)

In order to understand the higher activity of 1T-MoSe$_2$ in comparison to 2H-MoSe$_2$ and

the 1T- and 2H- forms of MoS$_2$, we have carried out first-principles calculations based on

density functional theory as implemented in Quantum ESPRESSO package [38], in which the

ionic and core-valence electron interactions are modeled with ultrasoft pseudopotentials [39].

The exchange-correlation energy of electrons is treated within a Generalized Gradient

Approximation (GGA) functional as parametrized by Perdew, Burke and Ernzerhof

(1996).[40] We use an energy cutoff of 35Ry to truncate the plane wave basis used in

representing the Kohn-Sham wave functions, and an energy cutoff of 280 Ry to represent

the charge density. Structures are relaxed till the Hellman-Feynman forces on each atom are

less than 0.02 eV/Å. We have used a periodic supercell geometry to simulate a 2D sheet,

including vacuum of 15 Å to separate the adjacent periodic images of the sheet. For self-consistent Kohn-Sham (scf) calculations, configurations of √3x√3 and √3x1 supercells, the BZ integrations are sampled over uniform meshes of 7x7x1 and 12x7x1 k-points respectively. Since KS-DFT typically underestimates electronic band gaps (a known limitation), we employ hybrid functional based on Hartree-Fock-Exchange (HSE)[41] with screened Coulomb potential to estimate the band gaps more accurately. The calculations were based on first-principles DFT using Projector Augmented Wave (PAW) method [42, 43] as implemented in the VASP (Vienna Ab-initio Simulations Package). [44] We have studied two super-structures of 1T-MoX$_2$ (where X = S and Se),√3x√3 and √3x1 [45] (Figure 11). Amongst the two superstructures, √3x1 is metallic and shows dimerization of Mo atoms, and √3x√3 is semiconducting with trimerized Mo atoms.

From phonon dispersion, we find that, both MoS$_2$ and MoSe$_2$ are stable in the √3x√3 and √3x1 superstructures

(a)   (b)
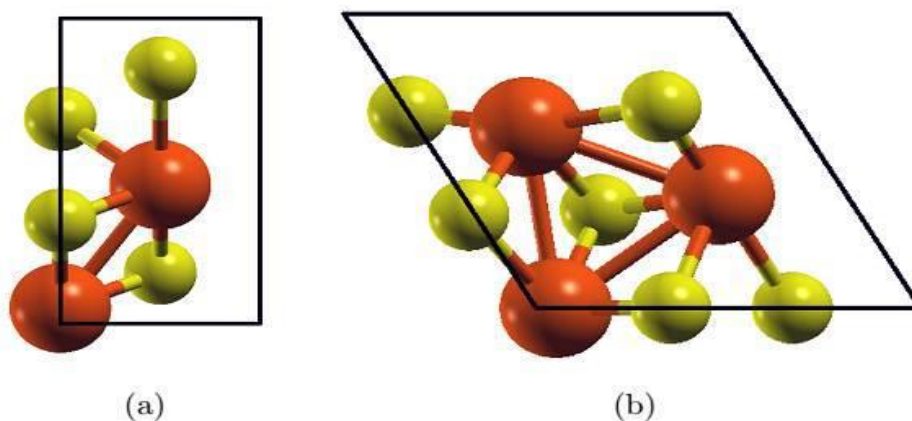
Figure 11. *√3x1 and √3x√3 superstructures of 1T-MoX$_2$ (where, X= S and Se). (a) √3x1 superstructure of 1T-MoX$_2$ showing dimerization of Mo atoms.(b) √3x√3 superstructure of 1T-MoX$_2$ showing trimerization of Mo atoms. Mo atoms are shown in orange color and X atoms are in yellow*

However, MoS_2 is energetically more stable in the $\sqrt{3}x\sqrt{3}$ compared to $\sqrt{3}x1$ by 27 meV/f.u., while the $\sqrt{3}x1$ super-structure of $MoSe_2$ is energetically more stable than the $\sqrt{3}x\sqrt{3}$ super-structure by 33 meV/f.u.

Experimentally, $MoSe_2$ is found to be in the $\sqrt{3}x1$ super-structure, in agreement with our first-principles results. Hence-forth, we shall consider the $\sqrt{3}x\sqrt{3}$ superstructure for MoS_2 and $\sqrt{3}x1$ superstructure for $MoSe_2$. To determine the efficiency of MoX_2 in reducing a proton to hydrogen as observed in experiments, we have estimated their electron affinities (EA) and work function (φ). For 1 metallic states, the relevant property here is the work function. The EA is estimated as the difference between the vacuum potential (Evac) and the lowest energy conduction band (ECB). Since DFT is a ground state theory, estimation of the band gap and hence the ECB is not accurate. Hence, we replace the ECB with EVB + Eg, where EVB is the energy of the highest energy valance band and Eg is the band gap. Since Eg is grossly underestimated in DFT calculations, we use the HSE corrections (using VASP) to determine Eg accurately. For the monolayered MoS_2, experimental value of bandgap (1.8 eV [46]) is available.

Comparison of the experimental bandgap with calculated bandgap for 2H-MoS_2 reveals that Kohn Sham bandgap is underestimated by 7.2% and the HSE bandgap is overestimated by 17.7% (see Table 3), in agreement with Ahuja *et.al.*[47] It is thus clear that the HSE method overestimates the experimental bandgap, whereas the KS-DFT calculation (GGA) yields a better estimate.

Table 3. *The calculated and exprimental values of bandgaps for 2H and 1T (√3x√3 superstructure) structures of MoX₂. HSE and KS-DFT bandgaps are calculated using VASP.*

	Bandgap (eV)		
Compounds	KS-DFT (VASP)	HSE (VASP)	Exp.
2H-MoS$_2$	1.67	2.12	1.834
2H-MoSe$_2$	1.45	1.88	1.35
1T-MoS$_2$ (√3 X√3)	0.76	1.28	
1T-MoSe$_2$(√3 X√3)	0.64	1.16	

As we can see that MoSe$_2$band gap is lower than MoSe$_2$, from Arrhenius equation we can see that it would be a better catalyst as energy barrier is less.

We use estimates of Eg obtained from KS-DFT calculations in this work. The work function is calculated as φ = Evac- EF, where EF is the Fermi energy. We find that (a) the 2H and 1T-polytypes of MoS$_2$ have a greater φ than that of the respective structure of MoSe$_2$ (refer to Table 4). This implies that it is easier to extract an electron from MoSe$_2$ compared to that of MoS$_2$ in both 1T and 2H polytypes, (b) The 1T polytype has a lower φ than that of 2H, which means that its easier for the 1T to donate electron compared to the 2H-structure. This explains why the 1T-polytype of MoSe$_2$ produces hydrogen more efficiently than the 2H-polytype as observed in experiments. The electron affinities of both 1T- and 2H-polytypes indicate that MoS$_2$ has a stronger electron affinity (indicating a higher tendency to attract electrons) than that of MoSe$_2$ (refer to Table 4), and the work function is also larger for MoS$_2$.

Table 4. *The calculated values of electron affinity (EA) and work function (WF) for 1T (for both √3x√3 and √3x1 superstructures) and 2H structures of MoX$_2$ (MoS$_2$ and MoSe$_2$)*

Superstructure	1T-form √3x√3		1T-form √3x1		2H-form	
Compound	MoS$_2$	MoSe$_2$	MoS$_2$	MoSe$_2$	MoS$_2$	MoSe$_2$
EA (eV)	4.95	4.42	-	-	4.22	3.78
WF (eV)	5.68	5.20	5.63	5.00	5.86	5.35

Thus, though MoS$_2$ more readily attracts/accepts electrons, it does not donate it that easily. Hence, MoSe$_2$ is efficient in hydrogen evolution as compared to that of MoS$_2$ as observed in experiments here.

Conclusions

The band gap of the $MoSe_2$ is lower that of MoS_2, and CBM of $MoSe_2$ is more negative than MoS_2 it is found to better in HER. Also it was found that metallic-1T is highly catalytic than 2H form as energy barrier decreases in 1T form. Among all the catalyst we have studied in this chapter metallic 1T-$MoSe_2$ prepared by Li intercalation followed by exfoliation of bulk 2H-$MoSe_2$, shows excellent H_2 evolution activity in comparison to few-layered semiconducting 2H-$MoSe_2$. Interestingly, 1T-$MoSe_2$ shows better H_2 evolution activity than 1T-MoS_2 as well. Our first-principles analysis reveals that $MoSe_2$ has a lower work function as compared to MoS_2, and that the 1T-structure exhibit lower work function than the 2H-structure for both MoX_2(X=S, Se). This results in the easy transfer of electron from the $MoSe_2$ for the reduction to hydrogen, and hence $MoSe_2$ is more efficient catalyst for hydrogen evolution reaction compared to MoS_2.

References

1. J. Barber, **Chem. Soc. Rev.** 2009, 38, 185

2. A. Kudo, Y. Miseki, **Chem. Soc. Rev**. 2009, 38, 253

3. B. Hinnemann, P. G. Moses, J. Bonde, K. P. Jørgensen, J. H. Nielsen, S. Horch, I. Chorkendorff and J. K. Nørskov. *J. Am. Chem. Soc.*2005, 127, 5308.

4. R. R. Chianelli, M. H. Siadati, M. P. De La Rosa, G. Berhault, J. P. Wilcoxon, R. Bearden, B. L. Abrams, **Catal. Rev.** 2006, 48, 1

5. H. Tributsch and J. C. Bennett. *J. Electroanal. Chem. Interfac. Electrochem*1977, 81, 97.

6. A. B. Laursen, S. Kegnaes, S. Dahl and I. Chorkendorff. *Energy Environ. Sc.* 2012, 5, 5577

7. H. Tributsch, J. C. Bennett, **J. Electroanal. Chem.** 1977, 81, 97

8. K. Sakamaki, K. Hinokuma, A. Fujishima, **J. Vac. Sci. Technol. B** 1991, 9, 944

9. T. F. Jaramillo, K. P. Jørgensen, J. Bonde, J. H. Nielsen, S. Horch, I. Chorkendorff, **Science** 2007, 317, 100

10. S. Helveg, J. V. Lauritsen, E. Lægsgaard, I. Stensgaard, J. K. Nørskov, B. S. Clausen, H. Topsøe, F. Besenbacher, **Phys. Rev.Lett**. 2000, 84, 951

11. J. Kibsgaard, J. V. Lauritsen, E. Lægsgaard, B. S. Clausen, H.Topsøe, F. Besenbacher, **J. Am. Chem. Soc.**2006, 128, 13950

12. M. Brorson, A. Carlsson, H. Topsøe, **Catal. Today** 2007, 123, 31

13. J. Bonde, P. G. Moses, T. F. Jaramillo, J. K. Nørskov, I. Chorkendorff, **Faraday Discuss**. 2009, 140, 219

14. D. Merki, S. Fierro, H. Vrubel, X. Hu, **Chem. Sci**. 2011, 2, 1262

15. Y. Li, H.Wang, L. Xie, Y. Liang, G. Hong, H. Dai, **J. Am. Chem. Soc.** 2011, 133, 7296

16. Z. Chen, J. Kibsgaard, T. F. Jaramillo, **Proc. SPIE** 2010, 7770, DOI:10.1117/12.860659.

17. Wang, L. Sun, C. Li, **Chem. Commun**. 2009, 4536

18. Q. Xiang, J. Yu,M. Jaroniec, **J. Am. Chem. Soc.** 2012, 134, 6575

19. X. Zong, H. Yan, G. Wu, G. Ma, F. Wen, L. Wang, C. Li, **J. Am. Chem. Soc.** 2008, 130, 7176

20. S. Min, G. Lu, **J. Phys. Chem. C** 2012, 116, 25415

21. U. Maitra, U. Gupta, M. De, R. Datta, A. Govindaraj, and C. N. R. Rao, **Angew. Chem. Int. Ed.,** 2013, **52**, 13057

22. F. Wypych, Th. Weber, R. Prins, **Chem. Mater.,** 1998, **10**, 723

23. A. N.Enyashin, L. Yadgarov, L. Houben, I. Popov, M. Weidenbach, R. Tenne, M. Bar-Sadan, G. Seifert, **J. Phys. Chem. C.,** 2011, **115**, 24586

24. C. Rovirat, M. Whangbo, **Inorg. Chem.**, 1993, **32**, 4094

25. H. Jiang, **J. Phys. Chem. C.** 2012, 116, 7664

26. J. Kang, S. Tongay, J. Zhou, J. Li, J. Wu, **Appl. Phys. Lett.,**2013, **102**, 012111

27. A. M. Lukowski, A. S. Daniel, F. Meng, A. Forticaux, L. Li, S. Jin, **J. Am. Chem. Soc.,**2013, 135**,**10274

28. D. Voiry, H. Yamaguchi, J. Li, R. Silva, D. C. B. Alves, T. Fujita, M. Chen, T. Asefa, V. B. Shenoy, G. Eda, M. Chhowalla, **Nat. Mat.,** 2013,12,850

29. S. J. Sandoval, D. Yang, R. F. Frindt, and J. C. Irwin, **Phys. Rev B.,** 1991,**44**,3955

30. J. Heising, M. G. Kanatzidis, **J. Am. Chem. Soc**.,1999, **121**, 11720–117323.

31. R. A. Gordon, D. Yang, E. D. Crozier, D. T. Jiang, R. F. Frindt, **Phys. Rev. B,** 2002,65,125407

32. H. S. S. Ramakrishna Matte, A. Gomathi, A. K. Manna, D. J. Late, R. Datta, S. K. Pati, C. N. R. Rao, **Angew. Chem.**, 2010, 122, 4153

33. C. L. Jia, M. Lentzen, K. Urban, **Science** 2003, 299, 870

34. J. A Wilson, F.J Di Salvo, S. Mahajan **Adv. Phys**., 1975,24,117

35. A. H. C. Neto, **Phys. Rev. Lett.,** 2010,86,4382

36. G. Eda, H. Yamaguchi, D. Voiry, T. Fujita, M. Chen and M. Chhowalla. **Nano Lett.**2011, 11, 5111.

37. U. Gupta, B. G. Rao, U. Maitra, B. E. Prasad, and C. N. R. Rao, **Chem. Asian J**. ,2014, DOI: 10.1002/asia.201301537

38. P. Giannozzi et al., **J. Phys.: Cond. Matt.** 21, 2009,395502

39. D. Vanderbilt, Phys. Rev. B**, 41**, 1990, 7892

40. J. P. Perdew, K. Burke, and M. Ernzerhof, **Phys. Rev. Lett**., 1996,**77**, 3865

41. J. Heyd, G. E. Scuseria, and M. Ernzerhof, . **J. Chem. Phys**, 2003,118, 8207

42. P. E. Blöchl, **Phys. Rev. B**, 1994, 1994, 50, 17953

43. G. Kresse and D. Joubert, **Phys. Rev. B**, 1999,59, 1758

44. G. Kresse and J. Furthmüller, **Phys. Rev. B,** 1996,54, 11169

45. J. Heising and M. G. Kanatzidis, **J. Am. Chem. Soc.**, 1991121, 11720

46. K. F. Mak, C. Lee, J. Hone, J. Shan, and T. F. Heinz **Phys. Rev. Lett., 2010,105**, 136805

47. Y. Li, Y. L. Li, C. M. Araujo, W. Luo and R. Ahuja., **Catal. Sci. Technol**.,201**3**, 2214